

POTENTIAL OF STRAIN INDUCED
SEMICONDUCTOR QUANTUM DOTS FOR DEVICE
APPLICATIONS

A DISSERTATION

SUBMITTED TO THE DEPARTMENT OF APPLIED PHYSICS

AND THE COMMITTEE ON GRADUATE STUDIES

OF STANFORD UNIVERSITY

IN PARTIAL FULFILLMENT OF THE REQUIREMENTS

FOR THE DEGREE OF

DOCTOR OF PHILOSOPHY

Serguei Albertovich Komarov

December 2002

© Copyright by Serguei Albertovich Komarov 2003
All Rights Reserved

I certify that I have read this dissertation and that in my opinion it is fully adequate, in scope and quality, as dissertation for the degree of Doctor of Philosophy.

James S. Harris, Jr. (Principal Advisor)

I certify that I have read this dissertation and that in my opinion it is fully adequate, in scope and quality, as dissertation for the degree of Doctor of Philosophy.

Malcolm R. Beasley

I certify that I have read this dissertation and that in my opinion it is fully adequate, in scope and quality, as dissertation for the degree of Doctor of Philosophy.

Shanhui Fan

Approved for the University Committee on Graduate Studies

ABSTRACT

Tremendous amount of research has been devoted to the study of quantum confined structures in the last decade. Semiconductor quantum dots are the most promising candidates for low-threshold optoelectronic devices as well as for quantum computing applications. Room temperature operation requirement strongly restricts conventional lithography use leading to alternative approaches to quantum dot fabrication. One of the most developed being strain-induced island growth in Stransky-Krastanow mode. Two major issues limiting potential of this method are the island size and position non-uniformity and proper material choice to achieve desirable quantum dot characteristics.

In the present work both these aspects will be addressed. Experimental evidence of improved in-plane self-organization resulting from vertically stacked strain-induced InAs islands in a GaAs matrix will be shown. Fourier analysis of the AFM allowed us to see the onset of the lateral island lattice formation and provided useful information on this lattice orientation and spacing.

To study the question of material choice, we have investigated an unconventional system: strain-induced InAs islands on Ge. We believe, that is the first time that nanoscale islanding in Stransky-Krastanow mode has been observed and characterized in this a material system. An advantage of this system is close lattice constants of GaAs and Ge, and thus, it becomes possible to compare InAs islanding trends in two systems where the strain state is the same but the underlayer material is different. The comparison of islanding dynamics in this system with that of InAs islands on GaAs substantiated the importance of other factors besides the epitaxial strain state, such as surface diffusion, in island formation and evolution.

ACKNOWLEDGMENTS

This thesis would not have been possible without support and guidance of my advisor, James S. Harris, Jr. I owe him a dept of gratitude for helping me choose my dissertation research topic, providing advice and encouragement along the way, sponsoring my education at Stanford University and trips to conferences, and last but not the least, for putting up with long periods of idleness, procrastination, and inactivity when my energy was dissipated on other pursuits.

I am deeply grateful to Glenn S. Solomon who was my senior collaborator for tremendous amount of help and advice he gave me throughout my time in Solid State and Photonics Lab.

I owe special thanks to the members of my reading committee, Malcolm R. Beasley and Charles M. Marcus for graciously agreeing to review this dissertation, and their helpful comments.

I am immensely grateful to Paula Perron and Gail Chun-Creech for always helping with overcoming any administrative barriers I encountered. I greatly appreciate enjoyable atmosphere that surrounded me at Stanford created by numerous Harris Group members and my friends. Olga Zuyakova deserves special mention for care and inspiration.

Finally, none of this would have happened were it not for my parents who provided as much support and kept as close a track of my progress as was humanly possible from 6,000 miles away.

DEDICATION

For Olga and my parents

TABLE OF CONTENTS

List of Tables	ix
List of Figures.....	x
Chapter 1: Introduction.....	1
Chapter 2: Growth And Characterization.....	6
2.1 Molecular Beam Epitaxy	7
2.2 Island Growth.....	18
2.2.1 Crystal Growth Fundamentals	18
2.2.2 Strain Induced Self-Assembly	29
2.3 Characterization Techniques.....	41
2.3.1 Atomic Force Microscopy	41
2.3.2 Transmission Electron Microscopy	45
2.3.3 Optical and Electrical Measurements	47
Chapter 3: Structural and Optical Properties of Strain Induced Quantum Dots.....	50
3.1 Coherently Strained, Defect Free Islands	52
3.2 Growth Factors Influencing Island Density.....	61
3.3 Quantum Confinement.....	67
3.4 Photoluminescence of an Ensemble of Quantum Dots.....	70
Chapter 4: Lateral Self-Organization of Vertically Stacked Quantum Dots	81
4.1 Vertical Stacking of InAs Dot Layers.....	82
4.2 Increase in Lateral Island Uniformity with Layer Stacking: Simulation.....	88
4.3 Experimental Observation of the Onset of Island Ordering	92
4.4 Fourier Analysis of The Islanding Statistics.....	96
4.5 Conclusions.....	99
Chapter 5: InAs Strain Induced Islands grown on Ge	101
5.1 Group IV Semiconductor Quantum Dots	102
5.2 Role of Surface Diffusion in Islanding Dynamics.....	105

5.4 Conclusions.....	114
Chapter 6: Quantum Dot Device Applications.....	115
6.1 Optoelectronic Quantum Dot Devices.....	116
6.1.1 Quantum Dot Laser.....	117
6.1.2 Quantum Dot Infrared Photodetector.....	120
6.2 Electronic Quantum Dot Based Devices.....	122
6.2.1 Single Electron Transistor.....	122
6.2.2 Cellular Automata.....	124
6.3 Conclusions.....	128
Chapter 7: Conclusions.....	129
Bibliography.....	133

LIST OF TABLES

<i>Number</i>	<i>Page</i>
Table 2.1: Correlation of the typical substrate temperature measurement by thermocouple (TC) with the more accurate temperature measurement made using reflectivity. Semi-insulating and N+ substrates are contrasted. ...	17

LIST OF FIGURES

<i>Number</i>	<i>Page</i>
Figure 2.1: Schematic of a Varian Gen II MBE indicating the necessary infrastructure surrounding the growth chamber.	10
Figure 2.2: Schematic of a MBE growth chamber	11
Figure 2.3: Schematic of the flux pattern on the substrate surface from the furnace sources.....	15
Table 2.1: Correlation of the typical substrate temperature measurement by thermocouple (TC) with the more accurate temperature measurement made using reflectivity. Semi-insulating and N+ substrates are contrasted. ...	17
Figure 2.4: GaAs equilibrium phase diagrams: a) temperature versus composition [66], b) partial pressure versus inverse temperature [67].	19
Figure 2.5: The vapor pressure of several elements over their solid or liquid state as a function of temperature [68].	21
Figure 2.6: Cut through the growth surface showing three different types of attachment sites: A) highest excess energy site because of the number of dangling bonds, B) ledge or kink site (medium excess energy site), and C) lowest excess energy site.	25
Figure 2.7: Variation in the surface terrace length with temperature. As the surface temperature increases the equilibrium distance between terraces also increases.....	26

Figure 2.8: During step flow growth the mean diffusion distance is greater the ledge separation and growth proceeds by advancing kink site along a ledge	27
Figure 2.9: Biaxial compression, of a larger lattice that is epitaxially deposited on a smaller lattice. Here the lattice mismatch is small enough so that elastic compression is possible and the epitaxy is pseudomorphic.....	30
Figure 2.10: The energetics of surface attachment sites on a strained surface are different than on the unstrained surface. Site C is no longer an energetically favorable attachment site.....	31
Figure 2.11: Schematic of surface profile when the surface diffusion length is reduced by increased flux and long wavelength surface roughness becomes kinetically unfavorable.....	32
Figure 2.12: The critical wavevector (maximum k) and wavevector with the maximum amplitude using two different surface diffusivity terms. Only the amplitudes are affected by the change in surface diffusivity	38
Figure 2.13: The surface topology is estimated using Equation 2.30 under large and small surface diffusivity. The diffusivity and the growth rate establish the state of surface roughness.	38
Figure 2.14: Schematic of an Atomic Force Microscope.	43
Figure 2.15: Schematic of a transmission electron microscope.....	45
Figure 2.16: Photoluminescence measurement experimental setup.	47
Figure 2.17: Quantum Dot sample for electrical measurements.....	48
Figure 3.1: Atomic-force microscopy (AFM) images of InAs islands formed from various amounts of InAs deposition at 500°C. (a) is after 2 MLs on InAs, (b) 3 MLs of InAs, (c) 4 MLs of InAs and (d) after 6 MLs of InAs. The InAs islands are not covered with.....	55
Figure 3.3: Three dimensional AFM images of the InAs islanding surface in the isolated island regime at two different growth temperatures. In (a) the growth temperature is 455°C, while in (b) the growth temperature is 500°C.	60

Figure 3.4: Atomic-force microscopy (AFM) images of the difference in island density when the monolayer coverage is changed from 2 MLs in (a) to 3 MLs in (b). In both cases the growth temperature was 500°C and the growth rate was 0.19 $\mu\text{m/hr}$.	63
Figure 3.5: Atomic-force microscopy (AFM) images of the difference in island density when the V/III flux ratio is changed from 36 in (a) to 18 in (b) and finally 9 in (c). In all cases the growth temperature was 500°C, the growth rate was 0.19 $\mu\text{m/hr}$., and 3 MLs of InAs were deposited.	64
Figure 3.6: Atomic-force microscopy (AFM) images of the difference in island density when the growth rate changed from 0.19 $\mu\text{m/hr}$ in (a) to 0.09 $\mu\text{m/hr}$ in (b).	65
Figure 3.7: The critical dot diameter for the existence of electron and hole bound states in a quantum dot [95].	70
Figure 3.8: The variation in the density of states as the dimensional confinement changes form bulk (no confinement) to a quantum dot (3D confinement).	72
Figure 3.9: The effect of rms surface roughness on the DOS of a quantum dot ensemble. As the roughness increases the DOS approaches the bulk DOS [97].	74
Figure 3.10: The gain is calculated as a function of the threshold current for GaAs/AlGaAs system (a), and as a function of wavelength for the InP/InGaAs system (b)[98]. The wavelength is constant in the left result, while the injection carrier density is constant in the right calculation result.	76
Figure 3.11: 8K PL of several samples which contain InAs thickness that vary between 1.5 MLs and 3.75 MLs. There is a transition from planar growth to dot growth between 1.75 and 2 MLs, while the intensity decrease between 3 and 3.75 MLs is due to non-radiative recombination.	77
Figure 4.1: (a) TEM (110) cross section image of several columns of vertically aligned InAs islands (dark regions), (b) Selected area diffraction pattern of	

TEM sample in (a) showing superlattice diffraction spots in the (001) growth direction.....	83
Figure 4.2: TEM image showing one column of vertically aligned InAs islands. The island height is approximately 40 Å and the in-plane dimension is approximately 180Å.....	85
Figure 4.3: Calculated island positions for dense (left) and sparse(right) initial distributions in the first (a,d), second (b,e), and fifth (c,f) layers of a stacked structure.....	89
Figure 4.4: Island distribution in the fifth stacked layer with the spacer thickness of 0.5(a), 0.8(b), and 1.2(c) length units. Island density dependency on spacer thickness (d).....	90
Figure 4.5: Autocorrelation function calculated for the initial island layer (solid curve) and for the fifth stacked layer (dashed curve).	91
Figure 4.6: Visual comparison of the surface morphology of one (left) and twenty (right) layered samples of InAs self- assembled coherently strained islands on GaAs. Length scale applies to both plots.....	93
Figure 4.7: 3-D AFM image of the InAs dot surface after 1 dot layer has been deposited.	94
Figure 4.8: 3-D AFM image of the InAs dot surface after 20 dot layers have been deposited.	95
Figure 4.9: Fourier spectra of the AFM images for one (a) and twenty (b) layers of InAs islands and (c) inverse Fourier transform of the “features of interest” in the 20-layered sample’s spectrum.....	97
Figure 4.10: AFM image autocovariance (100) sections for one (a), five (b), ten (c) and twenty (d) stacked layers of InAs self- assembled islands. Length scale applies to all plots	98
Figure 5.2: AFM scans of InAs island on GaAs with monolayer coverages: a) 1.5 ML, b) 2 ML, c) 2.5 ML, d) 3 ML, and e) 3.5 ML.....	110

Figure 5.3: Monolayer coverage dependencies of the island density (a) and average diameter (b) for InAs islands on Ge (solid line) and on GaAs (dashed line).	112
Figure 6.1: Schematic of a semiconductor laser.	118
Figure 6.2: Density of electronic states as a function of structure size.	119
Figure 6.3: Quantum dot infrared photodetector schematics.	121
Figure 6.4: Schematic of a single electron transistor.	122
Figure 6.5: Four quantum dot elemental cell in “0” and “1” states.	125
Figure 6.6: Interaction between two nearby QCA cells.	126
Figure 6.7: Simple logical elements implemented with QCA cells: (a) binary wire and (b) inverter [144].	127

Chapter 1: Introduction

A tremendous amount of research has been devoted to the study of quantum confined structures in the last decade. Progress in different fields of science including epitaxial growth [1-5], conventional electron-beam lithography [6-8], micro-lithography using scanning probe microscopy [9-12], and colloidal chemistry [13] resulted in various possible approaches to fabrication of nanoscale objects that can be characterized as quantum dots. Structures that provide quantum confinement in all three dimensions for a limited number of, usually below several hundreds, electrons or holes and often referred to as quantum dots, are of considerable interest from a purely scientific standpoint as they are distinguished by their discrete energy spectrum and, thus, share properties of single atoms and can be used as “artificial” atoms to test fundamental theories of the atomic physics. On the other hand, according to the semiconductor industry roadmap, in less than two decades, critical dimensions of conventional semiconductor devices will be rapidly approaching the scale at which only a small number of carriers will take part in a single device and therefore quantum theory should be utilized to accurately describe operation of such devices.

The most promising structures for detailed fundamental theory oriented study are lithographically defined semiconductor quantum dots [14] because of their regularity and uniformity. These dots have contributed greatly to the understanding of major quantum mechanical concepts dealing with multi-body interactions, wave functions of a carrier in a controllably defined potential well, usually confined by epitaxial structure in one dimension and by electromagnetic field in the other two dimensions. These structures [15], however, commonly require liquid He temperatures to manifest any significant

quantum effects due to dimensional limitations imposed by the capabilities of current lithographic techniques.

Work presented in this dissertation is mainly focused on strain-induced, self-assembled semiconductor quantum dots, in which quantum confinement originates from the epitaxial growth of moderately lattice mismatched III-V and group IV material systems. Proper choice of growth conditions and semiconductor compounds enables fabrication of quantum dot ensembles with nanometers to tens of nanometers dimensions for each individual dot. These nano-scale objects are not achievable with the current state of conventional lithography and propagate the potential of quantum dot applications into the range of room temperature operation. The major limitation of such self-assembled quantum dots is their uniformity and uncontrolled spatial location. Despite these limitations, self-assembled semiconductor quantum dots are the most promising candidates for low-threshold optoelectronic devices as well as for quantum computing applications.

The most developed self-assembly fabrication technique is strain-induced island growth from Stransky-Krastanow mode of epitaxial growth [16]. This growth regime is intermediate between planar 2-dimensional (2D), layer by layer, growth typical of homoepitaxy or heteroepitaxy involving materials with identical lattice constants and fully 3-dimensional (3D) Volmer-Weber [17] growth mode characteristic for highly lattice mismatched materials. Unlike the latter regime, islands nucleated during Stransky-Krastanow growth are dislocation free and, therefore, are superior for most potential device applications. The Stransky-Krastanow growth regime is usually observed when lattice mismatch between the quantum dot material and host substrate is in a moderate regime (3-10%). Molecular beam epitaxy (MBE) [18] was used to fabricate experimental samples of strain-induced self-assembled quantum dots grown in Stransky-Krastanow regime and discussed in this dissertation. This technique offers far superior control for semiconductor crystal growth, where material composition and deposition parameters can

be varied on the monolayer scale. Three main quantum dot characterization methods were utilized: atomic force microscopy, transmission electron microscopy, and optical spectroscopy. Chapter 2 of this dissertation describes fundamentals of molecular beam epitaxy, semiconductor crystal growth, including detailed discussion of strain induced island self-assembly, and basic principles of the used quantum dot sample characterization techniques.

Chapter 3 elaborates on the structural and optical properties of strain induced semiconductor quantum dots -the main objects of this study. Primary material system of choice: InAs on GaAs, produces coherently strained defect free islands 15-20 nm in diameter and about 4 nm high. Dependency of island characteristics from growth parameters, such as substrate temperature, deposition rates, III-V flux ratios is further discussed. Presence of “atomic-like” quantum states for carriers confined in such fabricated quantum dots manifests itself in the photoluminescence spectra observed on our samples at room temperature. However, the theoretically discrete spectrum is broadened significantly due to dimensional non-uniformity of InAs quantum dots in a GaAs matrix.

This inhomogeneous broadening poses a considerable challenge for attempts to take advantage of the discrete, delta function like density of states for carriers in strain induced self-assembled semiconductor quantum dots. Chapter 4 of this dissertation addresses a potential approach to overcome this challenge discussing vertical stacking of multiple InAs island layers in a GaAs matrix. Formation of strain induced island columns with layer stacking is observed and found responsible for increased lateral island uniformity. Experimental evidence of improved in-plane self-organization resulting from vertically stacked strain-induced InAs islands in a GaAs matrix will be shown. Fourier analysis of the AFM data allowed us to see the onset of the lateral island lattice formation and provided useful information on this lattice orientation and spacing.

Another important issue limiting the potential of strain induced semiconductor quantum dots is material choice. Chapter 5 contains an overview of materials systems commonly used for fabrication of self-assembled quantum dots along with their advantages and drawbacks. Group IV and III-V compound semiconductor quantum dots are compared. Strain induced islanding is reported for the first time in an unconventional combination of InAs on Ge. Comparison of this material system with widely researched InAs on GaAs provides interesting insights into the role of surface diffusion in islanding dynamics. Both InAs on GaAs and InAs on Ge have almost identical lattice mismatch, but quite different adatom binding energies. Considerable deviations in wetting layer thickness, island statistics, and phase evolution substantiate the importance of surface diffusion in strain induced island formation.

Chapter 6 discusses device applications for strain induced ensembles of quantum dots. The potential to reach communication wavelengths (1.3-1.6 μm) on a GaAs substrate the region of transparency for optical interconnects on Si along with potential to use stacked InAs quantum dots in GaAs matrix as an active media in low threshold semiconductor lasers justifies research efforts directed at the improvement of dimensional uniformity of these quantum dot arrays. Characteristics of the self organized island columns, combined with technological advances in conventional lithography, create an opportunity for fabrication of single electron tunneling based transistors showing Coulomb staircase behavior up to room temperatures. Demonstrated ability to incorporate III-V compound semiconductor quantum dots with superior optoelectronic performance into group IV host material currently used by the mainstream semiconductor industry opens up new perspectives for device integration.

Chapter 7 is devoted to conclusions based on the research presented in this dissertation. It also outlines future research possibilities aimed to enhance the potential of strain induced self-assembled semiconductor quantum dots and provides an outlook on alternative approaches to semiconductor device fabrication and operation which may become

mainstream when conventional semiconductor industry roadmap ventures into the realm of quantum mechanics.

Chapter 2: Growth And Characterization

This chapter consists of three parts. It begins with a description of basic principles, origins, and advantages of molecular beam epitaxy (MBE) contained in Section 2.1. This overview focuses on the need for abrupt interface structures in novel quantum well devices and gives some context to the experimental work in the following chapters. Both the MBE growth process and some of the specifics of MBE technology that are important to the quantum dot growth utilized in this project are touched upon in this section. Books are written about this topic, and while such a complete development is neither appropriate nor necessary here, some theoretical foundation will make the motivation of the experiments and the details of the experiments more clear.

Section 2.2 proceeds from the experimental crystal growth technique used in this work to fundamentals of crystal formation with emphasis on strain induced self-assembly of nanoscale islands at an interface of two lattice mismatched semiconductor materials. It is divided into two subsections: Section 2.2.1 elaborates on kinetics and thermodynamics of homogeneous epitaxial growth and introduces the main parameters influencing the process and equations of relevance; Section 2.2.2 follows up with a description of strained heterogeneous epitaxial growth leading to the formation of nano-scale islands, which occurs when material of moderately different lattice constant is deposited on a host substrate. This section is perhaps the most critical portion of this chapter and outlines the energetics for heteroepitaxial island formation.

Section 2.3 provides an overview of the main characterization techniques used to investigate ensembles of strain induced, self-assembled semiconductor islands throughout this work. Data collected with three methods are used in this dissertation. Section 2.3.1 describes basic principles and some of the specific aspects of atomic force microscopy (AFM). In particular, its high resolution and ability to observe surface topology on non-

conducting samples are important for our research. Transmission electron microscopy (TEM) is another powerful characterization tool described in Section 2.3.2. Cross-section TEM atomic resolution images of stacked strain induced islands are extremely valuable to gain insight into behavior of islands under investigation while they are submerged into matrix or the host material, which is necessary to successfully incorporate them into working optoelectronic devices. Section 2.3.3 is concerned with optical spectroscopy and electrical measurements of quantum dot structures which is probably the most important from the practical point of view, as that is how performance of an electronic or optoelectronic device based on strain induced semiconductor quantum dots can be directly evaluated.

2.1 Molecular Beam Epitaxy

To investigate fundamental fermion and boson carrier confinement in crystalline solids abrupt interfaces creating uniform and controllable confining potentials and high refractive index interfaces are required. In pursuit of these abrupt heterointerfaces highly kinetic crystal growth processes are the most desirable since the reduction of the total interface energy by the entropy of mixing drives most abrupt interfaces to diffuse in thermodynamic equilibrium. To generate the initially abrupt interface the reactants on the surface must be switched abruptly. Thus, the reactants stored in the growth process, that is the reactant species traveling in the growth system to the growth surface, must be small and well controlled. Generally, the two sources of stored reactants in growth systems are in the travel time to the substrate and travel through the boundary layers above the substrate. These two regions are somewhat arbitrary as there may exist upstream boundary layers and eddies that store reactants and are away from the substrate. Thus, a growth process in which delay times between the reactant sources and the substrate are small, and boundary layers are reduced is desired. This is the motivation for studying crystal growth in high vacuum environments where travel time from the source to the growth surface can be minimized to be the time of flight of effectively isolated atomic or

molecular species. Particularly attractive is the molecular beam epitaxy process in which molecular beams from thermally heated furnaces are used and beam switching is controlled by shutters. The background vacuum is in the 10^{-10} torr range and the beam density is approximately 10^8 molecules/cc so that there are effectively no collisions among the molecules in the molecular beams. The liquid or solid sources are contained in furnaces called Knudsen cells that have small orifices compared to the mean free path of the reactant species so material flows from the furnaces by effusion [19]. This is in contrast to free evaporation, because the furnace openings are small, hence a near equilibrium condition exists so that the effusion rates and spatial distribution of the beams from the furnaces can be predicted [20].

Molecular-beams were first studied in the early part of last century [21, 22] using vacuum systems composed of bakeable glass with base pressures of 10^{-7} torr. Between the 30's and late 50's there were improvements in vacuum technology, in-situ characterization and the understanding of epitaxy that led to rapid developments in MBE in the 60's. With the use of stainless steel vacuum components, vacuum quality dramatically increased in the late 50's and more complete investigations of molecular beams resulted [23, 24]. High energy electron diffraction (HEED) was developed [25] and applied to surface studies in epitaxy growth beginning in 1930 and a better understanding of factors controlling epitaxial quality began to develop. In the mid 30's the effects of substrate temperature on epitaxy were investigated [26] and the concept of strained epitaxy was proposed [27, 28]. Van der Merwe[29] provides a review of these early experiments. While Elleman and Wilman [30] vacuum sublimated PbS epitaxial film in 1948, and Miller and Bachman deposited CdS non-epitaxially using multiple molecular beams [31], the use of molecular beams from effusions cells to grow epitaxial material had to wait until 1964 when Schoolar and Zemel deposited PbS on NaCl[32]. For CdS the growth process was understood about the time of Miller and Bachman's experiments [33], however it took several years (until 1963) before CdS epitaxy was achieved by MBE [34]. GaAs was epitaxially deposited by MBE in 1964 by Cho and Arthur [35, 36] and Si molecular-beam epitaxy was first reported in 1966 by Joyce and Bradley [37] using a molecular beam of

silane. Arthur [38, 39] first reported the kinetic behavior of Ga and As on the GaAs surface which led to understanding of the growth mechanism. Just as the MBE process was becoming well understood new device structures based on quantum confinement were being proposed [40] and this greatly accelerated MBE research. Excellent III-V epitaxy was produced in this early period by Arthur [41], Cho [42], Cho et al. [43], Esaki et al. [44] and Chang et al. [45] and was the foundation for the growth of the new quantum semiconductor structures. In 1974 Esaki and Chang reported electron tunneling across the potential barriers [46] formed by heteroepitaxial growth, and Dingle showed the energy quantization in these structures using optical spectroscopy [47].

The newly emerging quantum device physics using artificially constructed epitaxial semiconductors really pushed the rapid expansion of the MBE crystal growth technique. Several technical improvements to the MBE growth system in the mid 70's extended the complexity of the epitaxial structures and increased the epitaxial purity. The use of control systems for shuttering furnaces allowed for long, complicated growth structures with accurate thickness [48], such as superlattices [40], while improvements in the background pressure increased the purity of the epitaxial growth, and was especially important with respect to the purity of AlAs containing compounds [49]. Larkins et al. [50] provides a general review of high purity III-V MBE growth. A significant advance was the addition of liquid nitrogen cryopanel around the furnaces [51] and inside the main chamber, which besides acting as a general pump, provided better flux control by eliminating the rebounding of As species from the chamber walls to the growth surface [52]. An additional increase in purity resulted from gate valved load lock entry chambers in which pre-growth thermal cleaning could be conducted. A schematic of the Varian Gen II, system that was used in this work, is shown in Figure 2.1. It was developed in the early 80's and except for a host of continuous incremental changes it remains essentially the same machine today, although the product line was sold first to a Varian spin-off called Intevac and finally to EPI in the early 90's. In this system the preparation chamber is a load lock chamber, isolating the growth chamber from ambient. The growth chamber contains LN cryo panels for the sources (called the furnace/shutter cryoshroud in the

Figure) and the main chamber (called the substrate cryoshroud in the Figure) which reduce the base pressure of the machine by a factor of 2 or 3. In Figure 2.1 only a 400 l/s ion pump pumps the growth chamber, while in the systems used in this work, an additional 1000 l/s cryo pump was also used in the main chamber. After proper baking of the machine in the 175°C range for approximately 3 days, loading the machine with source material and rebaking, and several 'conditioning' runs the base pressure of the machine is typically 1-2 10^{-10} torr.

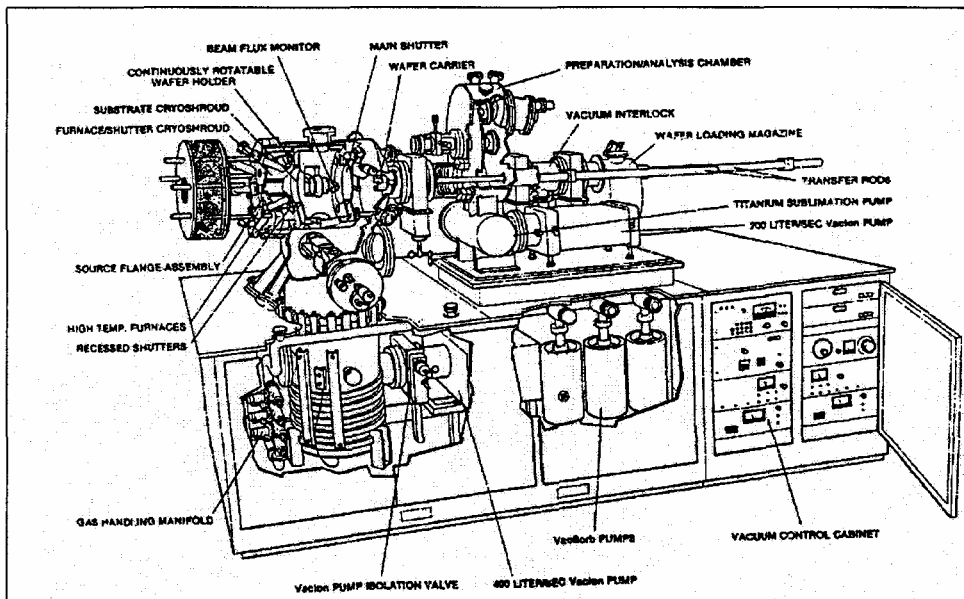


Figure 2.1: Schematic of a Varian Gen II MBE indicating the necessary infrastructure surrounding the growth chamber.

A substrate is loaded into the preparation chamber, which is isolated from the main growth chamber by an O-ring sealed gate valve. In the preparation chamber, the substrate is degassed at 400°C for approximately 45 minutes. After the pressure in the preparation chamber reaches an acceptable value, the substrate can be transferred into the growth chamber, where it is mounted on a rotating holder that contains the substrate heating elements.

A stylized schematic of the growth chamber is found in Figure 2.2 and provides a better view of the main growth chamber. The substrate is transferred and mounted to the substrate heater unit using a magnetically coupled transfer rod. In Figure 2.2 the substrate is shown facing the source in the growth position; however, the substrate heater unit can be rotated to load/unload wafers to the preparation chamber.

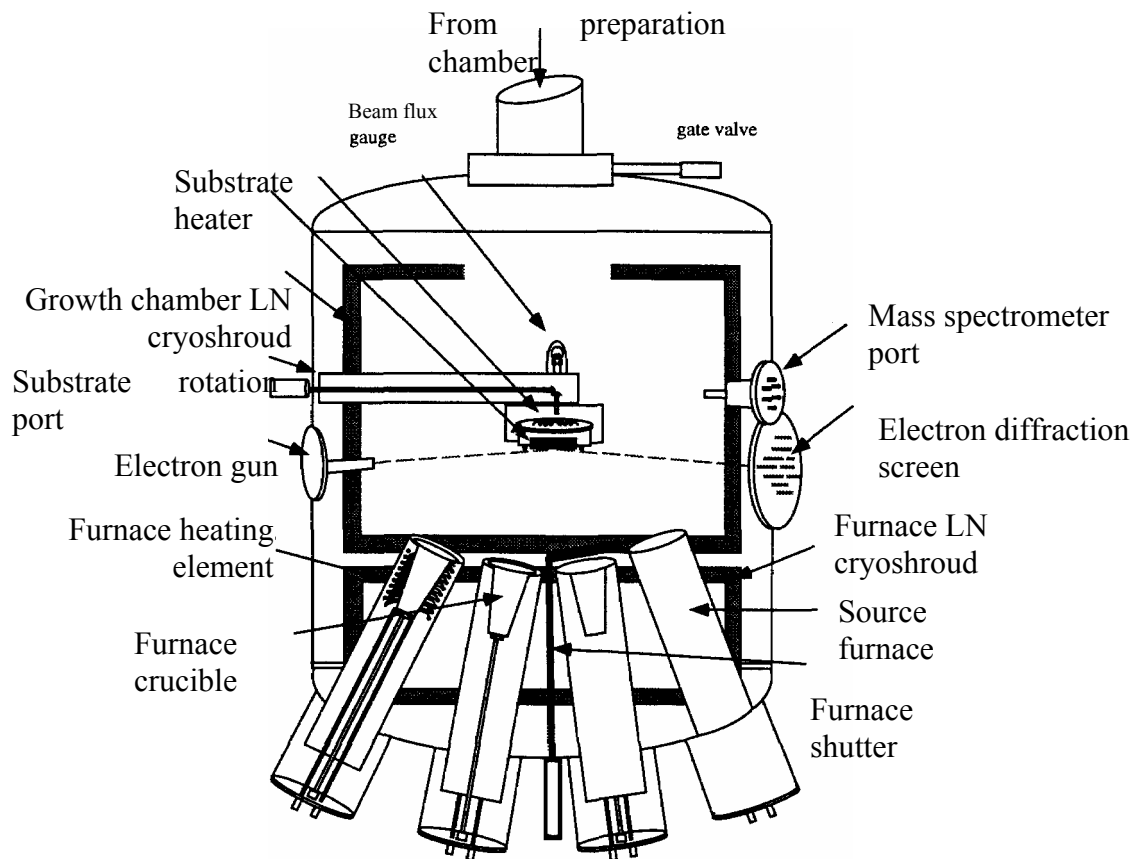


Figure 2.2: Schematic of a MBE growth chamber

From Figure 2.2, we can see that the main LN cryoshroud encases the substrate manipulator unit, as the furnace LN cryoshroud encases the source flange portion of the machine. The usual mode of operation is to have LN continuously flowing through both

sections; however, in our labs an alcohol/water mixture at -10°C flows through the furnace cryoshroud section, while LN flows through the main shroud. The reasoning behind this choice is not only cost, but efficiency and safety. Unlike the main cryoshroud, the furnace shroud serves mainly as a cooling source for the hot furnaces, and the thermal conductivity of the water mixture is superior to LN [50]. In addition, there is a failure mode for the cryoshroud that appears to result from freezing of water vapor in confined internal microcrevices when the LN is purged from the cryoshroud during routine source loading. This failure mode is eliminated using the alcohol/water solution.

Some additional instrumentation, which is essential for high quality MBE operation is also shown in Figure 2.2. The electron gun and electron diffraction screen provide glancing angle reflective high energy electron diffraction (RHEED) of the growth surface. This is the same surface analysis technique developed in the 1930's. RHEED provides in-situ surface analysis in the form of reciprocal lattice imaging of the crystal surface and monolayer-scale growth rate calibration. The value of RHEED as an in-situ surface characterization tool cannot be underestimated, and its use has clearly set MBE apart from other crystal growth techniques that cannot use this surface analysis tool. In the early years of MBE, RHEED provided information on surface reconstruction and surface kinetics that was critical to the understanding of the crystal growth process [54, 55, 56]. Its use as a scientific tool continues in non-planar growth studies, the growth of new materials and a finer understanding of typical epitaxial growth. In addition, monolayer-scale growth rates can be measured using RHEED through the variation in intensity of the diffracting beam as the growth surface undergoes a cycle of complete and planar coverage, new partial coverage which scatters and reduces the diffracting intensity, to complete coverage again as a new planar monolayer is complete and restores the beam intensity [57]. The other in situ tool shown in Figure 2.2 is the mass spectrometer, which is typically used to characterize the background partial pressure of the growth chamber. In the high vacuum regime of MBE the dominant background species are H (AMU 1), CO (AMU 28), As (doubly ionized at 47) and doubly ionized

AsO (95). The mass spectrometer can be used to study surface desorption or surface reflection of reactant species, but in this case, the mass spectrometer must be positioned in a more line-of-sight angle to the substrate [58].

Four of eight furnaces are shown in Figure 2.2 in various cut-away views. Three types of boron nitride (pBN) crucibles are used in the standard Knudsen furnaces depending on whether the source is a dopant source (small crucible), standard metal source or standard group V source (larger crucible). The taper of the crucible is important to both the pattern of the molecular beam and the change in that pattern as the source melt is depleted [59]. The crucible and charge are heated using tungsten wire, which is wrapped in various patterns to optimize the particular source. In particular, to reduce the condensation of Ga on the crucible lip, the heater wire is typically wrapped more densely at the lip of the Ga crucible or a separate heating zone is added to the lip section. The Ga condensate may react to form a gallium oxide or may remain as a gallium droplet, but in any event, the droplet can be spit into the Ga beam and form an inclusion in the epitaxy that is called an Oval defect. Heating the upper lip area of the Ga crucible significantly reduces this effect and is therefore nearly universally used [112]. However, for the Al charge, the Al melt can wet and climb up the crucible walls and either directly damage the furnace or drip Al into the growth chamber. To reduce this problem, the furnace wire density is decreased towards the furnace lip to create a cooler upper zone. Finally, a new two zone As furnace is often used in which the As_4 beam is cracked to an As_2 beam in the second zone. The advantage of cracked As_4 is that the As tetramer must decompose on the growth surface, since it is incorporated as As_2 into the lattice; supplying As_2 to the surface instead of As_4 gives greater substrate temperature flexibility and reduces the required As beam flux. As an aside, there is a problem with increased n-type background when the cracking zone is heated to a level, which insures 100% decomposition of As_4 to As_2 . This has been associated with a greater incorporation efficiency of Si, which exists as an impurity in As_4 , but may be related to out-gassing from the cracker section of the furnace. In addition to the cracker, a valve assembly can be added to the cracker design. Because of the high vapor pressure of As a large As charge is required in comparison to other source material

and it can take many hours to stabilize the As flux. One would like to load the furnace with a larger charge of As but this requires even longer stabilization periods. The addition of a valve assembly so that the As flux can be adjusted without adjusting the As source temperature remedies this problem. Now, a large charge of As can be loaded into the furnace and maintained at a constant temperature, the flux being adjusted by the valve. This valved cracker As source was used to great advantage in this work to accurately study the effects of V/III flux ratio on InAs island formation.

Except for the group V (As) cracking cell, the fluxes from the Knudsen cells are controlled by changing the furnace temperature. Assuming the crucible opening is negligibly small, the density of molecules in the cell is proportional to the partial pressure and inversely proportional to the cell temperature. The flux from the crucible is related to the molecular density by a geometric factor which is often approximated as r^2/L^2 , where r is the radius of the crucible opening and L is the distance from the furnace at which the flux is measured [23]. Using the Clausius-Clapeyron relation in the ideal gas approximation,

$$R \frac{\partial(\ln P)}{\partial \frac{1}{T}} = \Delta H \quad (2.1)$$

the partial pressure, P and hence the flux, is exponentially related to the furnace temperature. Thus, the flux can be adjusted through a large range by small but controllable temperature changes. A schematic of the flux pattern from the furnace cells is shown in Figure 2.3. All the furnaces and fluxes are axially symmetric to the normal of the substrate in the growth position. The center of the flux distribution from each furnace is purposely designed to lie away from the substrate center, the intersection of beam axes of all the furnaces lies behind the substrate. Since the substrate must be rotated during growth to maintain compositional uniformity across the growth surface, the off center flux apex from each source creates a more uniform flux profile across the wafer when averaged over a complete wafer revolution.

The beam flux is measured using a Bayard- Alpert ionization gauge. The gauge generates electrons from a hot filament, which circle around a positively biased grid. These electrons collide with passing flux molecules and ionize them. The positively charged flux molecules are then attracted to a collector where they are measured as current. The measured current is directly related to the beam flux pressure but it is also a function of the ionization and capture efficiencies. These efficiencies depend on the time a molecule spends in the region, i. e., the molecule velocity, which is related to the square of its temperature so that,

$$J = P\eta\left(\frac{3kT}{M}\right)^{\frac{1}{2}} \quad (2.2)$$

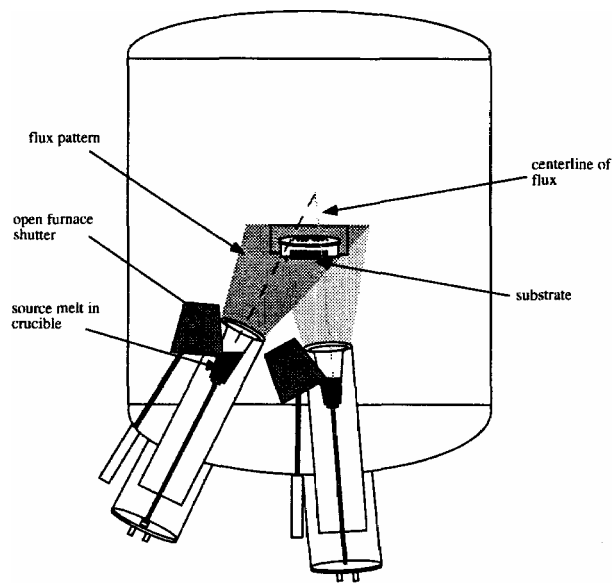


Figure 2.3: Schematic of the flux pattern on the substrate surface from the furnace sources.

where J is the current and η is the ionization constant and is related to the molecules atomic number. In this work the current is incorrectly assumed to be equal to the beam partial pressure. In general, this approximation is acceptable since the growth rate is measured in some way (either RHEED for small mismatch cases, or X-ray diffraction for

strained epitaxy) and a constant between growth rate and group III beam flux is established. The group III flux measurement is simple, as the sticking coefficient of the group III metals is unity and so the current is stable. However, the As flux continues to rise because once the gauge surface area is saturated with As, the As sticking coefficient begins to drop and As molecules recoil back into the ionization region and change the gauge efficiency. In practice, the As flux is measured over a set time period using computer control and averaged. All As flux measurements are made in this manner for consistency. The V/III flux ratio can dramatically effect the substrate surface, but investigations of this effect on the surface depend on many factors, such as material choices and substrate temperature and must be examined with RHEED on the actual growth surface, then some general correlations with ionization gauge pressure can be established. Since the growth rate is dependent of group III flux the As flux measurement is not critical; however, there are sections in this dissertation in which more careful control of the As flux was necessary, and the use the As valved furnace source and computer controlled flux averaging was extremely useful.

In conventional, planar MBE growth there is a large growth temperature window, which does not necessitate substrate temperature accuracy to better than about 15 °C. The initial oxide layer must be desorbed at higher than growth temperature. This can be accurately accomplished using RHEED to see the surface reconstruction appear after the oxide has been desorbed, or less accurately by simply making sure the substrate temperature is above the desorbing temperature for some fixed period of time. In the latter case, the substrate is held at 680°C for 15 minutes under an As flux. Growth temperature windows are also present. Without using an As₂ flux (i.e. using As₄ flux) AlGaAs depositions in the 610-630°C range produce rough surfaces and interfaces. However, As₂ is now typically used and alleviates this problem. Indium will be desorbed from InAs surfaces above 530°C and grows more planar on GaAs at lower growth temperatures. These situations do not require highly accurate temperature measurements. However, for the island growth discussed in this work, finer substrate temperature resolution is required as a 10°C change in temperature can produce a large change in island size. We employ a

substrate temperature measuring system [60, 61] that utilizes the change in wavelength position of the band edge of a semiconductor as a function of temperature. A look up table was developed based on the change in the absorption edge of GaAs as a function of temperature. The system uses the inflection point of the band edge as a measuring point. Physically, a detector is placed on the outside of a heated viewport,

The previous discussion just		N type	
Substrate TC	Reflectivity	Substrate TC	Reflectivity
700	620.1	700	677
600	549.7	600	603.7
540	549.7	540	556.6
530	496.5	530	549.7
500	467.05	500	528.7
480	448.2		
470	440.55		
450	421.2		
$T_{ref} = 4.6663 + 0.92569T_{rc} (R = 0.99966)$		$T_{ref} = 153.85 + 0.74776T_{rc} (R = 0.99987)$	

Table 2.1: Correlation of the typical substrate temperature measurement by thermocouple (TC) with the more accurate temperature measurement made using reflectivity. Semi-insulating and N+ substrates are contrasted.

which is normal to the substrate. Light, either from the substrate heater passing through the substrate, or light incident on the substrate through the viewport is collected and passed through a spectrometer. The correlation between the substrate thermocouple temperature and the temperature measured by band edge absorption has some run to run variation which is mainly due to the difference in substrate holders (differences in depositions on the holders) and more importantly-slight differences in the way substrates are mounted on the holders. However, the largest variation between substrate thermocouple and absorption edge values occurs between doped and undoped substrates, where the large free carrier absorption from the doped substrates causes a significant temperature difference between thermocouple and band edge absorption measurements. Values of corrected temperature for doped and undoped thermocouple readings are found in Table 2.1 and have been used throughout this work. To insure uniform temperature values, undoped substrates were used whenever possible. In cases where doped substrates

were necessary, such as in light-emitting diodes, the corrections found in Table 2.1 were used.

2.2 Island Growth

The InAs islands that form on GaAs surfaces are the result of competing strain and surface tension processes. In this section the relationship between these processes is formally developed. To fully understand the effect of mismatch strain on epitaxial growth, homoepitaxial growth is first discussed. After the thermodynamics and kinetics of the ideal, non-strained system are developed, strain is added and the equilibrium surface shape changes to a new equilibrium shape. This surface topology is determined by the competing process of surface tension, which drives the surface to minimize its area and thus becomes planar and strain, which drives the surface to island and increases elastic relaxation. In both the homoepitaxial and strained heteroepitaxial growth the effects of growth parameters such as flux ratios, growth rates, and surface temperature are shown to limit these equilibrium shapes.

2.2.1 CRYSTAL GROWTH FUNDAMENTALS

The thermodynamic equilibrium growth of GaAs is well understood through early work in LPE and bulk growth experiments. Because of the three extensive thermodynamic variables, temperature (T), pressure (P) and composition (X), a three dimensional plot is needed to completely describe the equilibrium system. This is generally represented using 2 dimensional plots of T-X, and P-T, and for GaAs, are shown in Figure 2.4 [66,67].

Salient points are now discussed. In Figure 2.4a the phase diagram is shown where a liquid region exists for temperatures above the solid phase states. This is not the case for MBE growth where the GaAs surface is in vacuum. The solidus region, shown in Figure 2.4a and represented by the dotted lines, is exaggerated and although it is shown symmetric about a 50-50 composition in this figure, it is not. However, this detail is not important for MBE growth because the growth temperature is nearly always below 800°

C. The melting point of stoichiometric GaAs is high and well above the typical

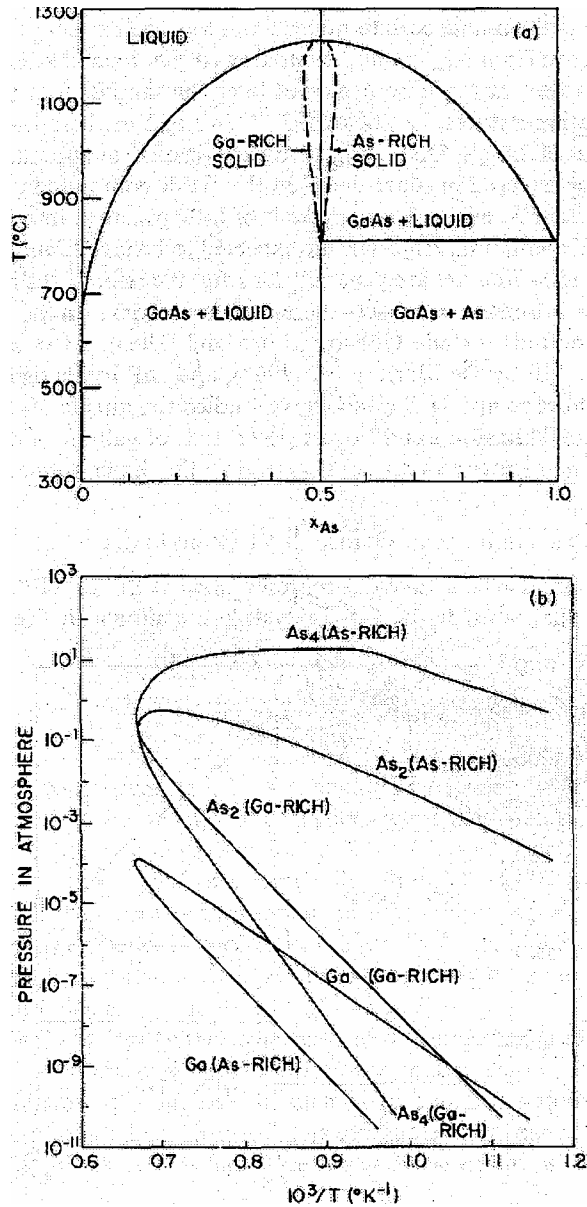


Figure 2.4: GaAs equilibrium phase diagrams: a) temperature versus composition [66], b) partial pressure versus inverse temperature [67].

MBE growth temperature ($\approx 600^{\circ}\text{C}$). From Figure 2.4a any excess Ga on the GaAs surface will exist as a liquid at typical MBE growth temperatures, if GaAs is to be grown with a Ga rich flux ratio a nearly exact Ga to As net surface flux must be maintained and is practically impossible in normal operation, Thus the As - rich sections of Figure 2.4b

are appropriate. In Figure 2.5 the vapor pressure of several elements are shown as a function of temperature. Whereas in Figure 2.4b, the vapor pressure of Ga and As are given over GaAs, in Figure 2.5 the vapor pressure of each element is given over itself. The As vapor pressure over As is several orders of magnitude larger than the vapor pressure of As over Ga. Thus, excess As, i.e. As on an As terminated surface quickly desorbs, maintaining stoichiometry. Because of the natural excess desorption of As, As rich growth is the usual growth mode. Also note that GaAs can be grown As rich as a solid; although it appears this can be done to nearly 800°C, because of the even higher As vapor pressure required to stabilize the As rich GaAs surface in vacuum this is practically impossible at this temperature but can be done at lower temperatures. The use of As rich GaAs in conjunction with a high temperature anneal to enhance the As inclusion grain growth has been a useful insulating layer for device isolation.

The thermodynamics of the growth surface practice is dominated by the volatility of As and in an As flux must be applied to the surface or a GaAs +liquid mixture will result. In MBE the net flux to or from the surface is found from the surface lifetime of individual beam constituents,

$$\tau_i = \frac{1}{\nu_i} \exp\left(\frac{\Delta\mu_i}{kT}\right) \quad (2.3)$$

where $1/\nu_i$ is the surface hopping frequency of the i th, and $\Delta\mu_i$ is the difference in the surface and vapor chemical potentials of the i th component,

$$\Delta\mu_i = \Delta H_i - \Delta\mu_{state} - T\Delta S_{mixing} \quad (2.4)$$

where ΔH_i is the i th component enthalpy of absorption, $\Delta\mu_{state}$ is the chemical potential change in going from the gas to solid (or liquid) state, and ΔS_{mixing} is the entropy of mixing. For As_4 or As_2 on an As_2 terminated surface $\Delta\mu_{state}$ is basically unchanged, but since in the MBE process, the As source temperature is typically 200°C lower than the surface temperature, ΔH_i is negative, so the lifetime is small. The opposite is true of Ga on a Ga surface, where the Ga source is many hundreds of degree higher than the

substrate, making ΔH large and the surface lifetime long. Therefore, liquid Ga can build up on the GaAs surface, while excess As will not accumulate. There is extra energy associated with the surface because the bulk crystal periodicity is broken leaving unsatisfied bonds. This excess energy is reduced by surface reconstruction in which dangling bonds from surface atoms are eliminated by a reordering of surface atoms into a 2-D surface lattice. The effects of various As partial pressures on the type of lattice

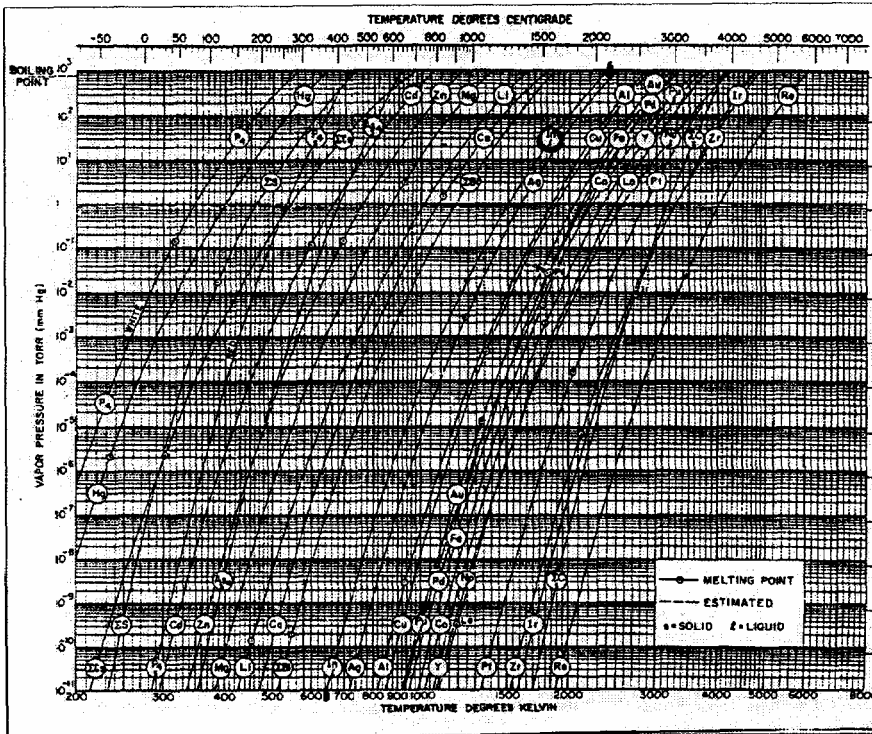


Figure 2.5: The vapor pressure of several elements over their solid or liquid state as a function of temperature [68].

reconstruction has been well characterized and it is clear that there are several intermediate surface reconstructions that exist between the well stabilized 2×4 : reconstruction and the GaAs + liquid mixture [69]. Although this concern with the As partial pressure might make the GaAs growth appear fragile, in fact it is quite the opposite because the need to always supply more As than is required for GaAs growth means that the growth rate is controlled only by the flux of Ga to the surface. Since an excess As flux must always be present, there always exists an As dimer on the surface to

bond with Ga. Although too much As at a the typical MBE growth temperatures may not affect the crystalline quality, it can make for a rough growth surface by reducing the Ga adatom surface diffusivity. Thus the V/III flux ratio is bounded high and low, but in practice, there is a wide acceptable range from 5 to around 20 (depending on the growth temperature). While ratios much lower than 5 can be catastrophic there are many situations in multilayer structures where the grower must use ratios significantly higher than 20 with only the danger of increased surface roughness.

The state of surface roughness is a function of several other variables besides the V/III flux ratio. In thermodynamic equilibrium the surface roughness is primarily a function of the extra energy associated with the particular free surface in question. The total internal energy provides a complete description of system equilibrium and can be represented by Euler's Equation, $U = TS - PV + \mu N$, where T, P, μ represent the well know temperature, pressure and chemical potential while S, V and N are the extensive properties of the system; entropy, volume and particle number. When such a system is cleaved, the internal energy increases (or else the system would spontaneously cleave), which is related to some increase in surface energy due to a disruption in crystal periodicity, such as the surface reconstruction discussed above. Euler's equation can be modified to include this additional surface energy using the surface tension, (γ), acting on the surface area, A,

$$U = TS - PV + \mu N + \gamma A \quad (2.5)$$

Differentiating with respect to the intensive variables, the Gibbs-Duhem equation results

$$A\gamma + SdT - VdP + Nd\mu + A\sum_{i,j}(\gamma\delta_{i,j} - \sigma_{i,j})d\varepsilon_{i,j} = 0 \quad (2.6)$$

Since there are two other dependent free energy equations for the bulk and vapor phases, we are free to arbitrarily define the volume, V and the number, N and we set them to zero with no loss of generality, and Equation 2.6 reduces to,

$$S_{i,j} = -A \left. \frac{\partial \gamma}{\partial T} \right|_{\epsilon} \quad \text{and} \quad \sigma_{i,j} = \gamma \delta_{i,j} + \left. \frac{\partial \gamma}{\partial \epsilon_{i,j}} \right|_T \quad (2.7)$$

Even though we are free to define the surface region as arbitrarily thin (in fact of zero thickness) by adjusting the volume of the bulk and vapor phases, this is generally a realistic assumption since we are taking a macroscopic perspective; compared to the vapor and bulk volumes, and particle numbers the surface region is effectively of zero thickness. However, in the high vacuum MBE growth process where boundary layers are minimized, this is especially appropriate.

Thus, from Equation 2.7 in thermodynamic equilibrium the entropy of the surface is affected by the change in surface tension with temperature, and more importantly the surface stress is in general not equal to this surface tension (unless the surface is a liquid). Therefore, there is a driving force for the surface to rearrange to reduce the effect of the strain on the surface tension, so that if some additional strain, such as lattice mismatch strain is added to the surface, the driving force for the surface to rearrange increases [70]. γ is also a function of the orientation of the surface because of the number of dangling bonds or the nature of the surface reconstruction. There are a set of orientations which provide local and global minimum in the surface tension and are thus preferred [71]. So, given the proper time, the final surface shape will expose different planes whose predominance is reflected by their relative surface tension [72]. In cubic crystals, neglecting surface reconstruction effects, the $\{100\}$ planes are predominant with some $\{111\}$ planes present [73]. Therefore, the (100) surface is a stable growth surface for GaAs; however, perturbations, such as lattice mismatch strain, can drive the growth surface to a faceted surface that helps to relieve this strain and does not create too much increase in surface tension. This can result in increased step exposure. As the temperature increases the surface is driven to a more disordered state and the anisotropic effects of surface tension have been shown to subside and equilibrium shapes become rounded. The degree to which this occurs is a function of the magnitude of the surface tension, but other effects, such as lattice mismatch strain can play a large role. The surface shape, including faceting effects is defined thermodynamically above; however, there is also a

kinetically limited surface topology. While large macro-scale roughness can occur at high temperatures from thermodynamic effects, a fine micro-scale roughness can occur at low temperatures due to kinetic effects. The mean surface diffusion length is defined through the Einstein equation,

$$X_i^2 = 4D_i\tau_i \quad (2.8)$$

where τ_i has been defined in Equation 2.3 and the surface diffusivity of the i th species is defined as

$$D_i = a^2\nu \exp\left(\frac{\Delta G}{kT}\right) \quad (2.9)$$

where here ΔG is the activation energy between adjacent sites. For Ga surface diffusion ΔG is the limiting factor since the sticking coefficient is unity, while for the As surface diffusion length both τ and ΔG are important. A cut through a planar growth surface is shown in Figure 2.6 (top). Three types of sites are shown. Site C is the lowest energy site in the Figure since it is bonded to more adjacent atoms and thus ΔG is largest. Site B is actually 2 different types of sites on a 2-D surface (see Figure 2.6 bottom), a kink or ledge site, and has the next largest ΔG , while the exposed surface site A has the lowest activation energy because it is bonded to the least amount of adjacent atoms. If the surface preparation is not exact before the substrate is heated under proper As flux stabilizing conditions the planarization of the surface will increase as C sites are initially filled from adatoms migrating predominately from low energy attachment sites A. When the substrate surface is heated under As stabilized conditions, but without growth (no Ga flux), the distance, λ_l between ledges is a function of the surface temperature if the As stabilized flux is minimized. See Figure 2.7. At extremely low temperatures there is minimum diffusion and the average terrace length is shorter than the existing roughness and there is minimal movement or change to the surface. At slightly higher temperatures, X_i is small, but larger than the existing roughness scale and a new equilibrium λ_l is established that is larger than the previous roughness length scale. As the

surface temperature is increased further, X_i increases and thus so does the equilibrium ledge distance, so that roughness attributed to ledges diminishes with increasing temperature. However, this is not the complete story; as the surface temperature increases so does the entropy of mixing of surface states (configurational entropy associated with the surface sites) [73] and so with increasing temperature the vertical interface roughness

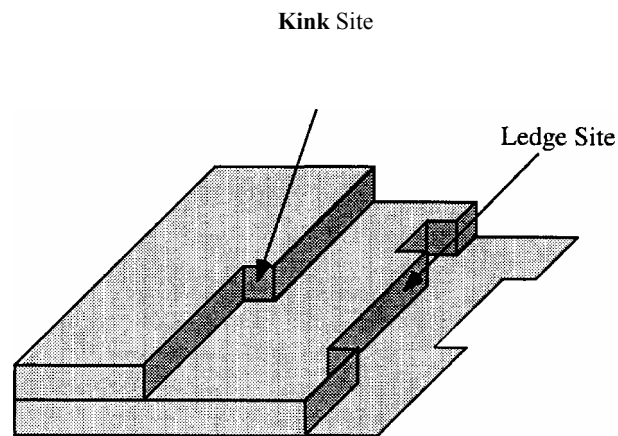
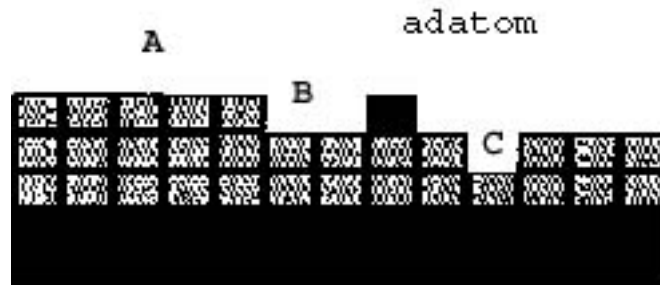


Figure 2.6: Cut through the growth surface showing three different types of attachment sites: A) highest excess energy site because of the number of dangling bonds, B) ledge or kink site (medium excess energy site), and C) lowest excess energy site.

increases and the fine scale roughness on and between ledges increases. Since adatoms are less tightly bond to ledges than to the flat surface (site C in Figure 2.6) the ledges will always have more roughness than the flat surface. The vertical and horizontal roughness is also increased by an increase in the minimum As flux required to stabilize the growth

surface at higher temperatures. More As adatoms are impinging and leaving the surface creating more variation in surface sites. Thus, even though the average terrace length is larger at higher surface temperatures a fine scale roughness due to disorder increases. The variation in roughness is also larger at higher temperatures as $\delta(\Delta G)$, the variation in the average surface activation energy increases as the variation in surface sites increases. The result is that the surface roughness wavelength and roughness amplitude increases with increasing surface temperature. If the growth parameters are correct (surface temperature is large enough, and fluxes low enough) when growth begins, adatoms will diffuse over the surface and find the lowest energy attachment positions of first C sites, then B sites, and a planar growth front will be maintained.

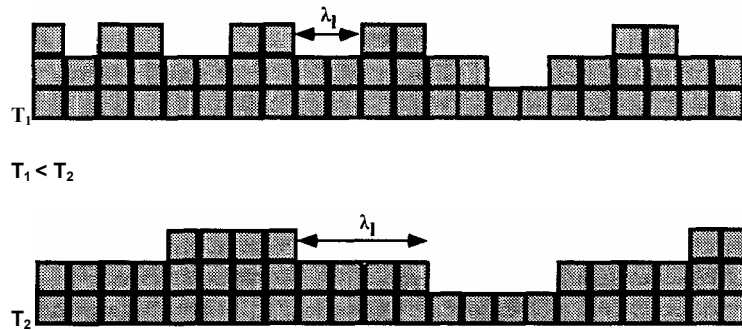
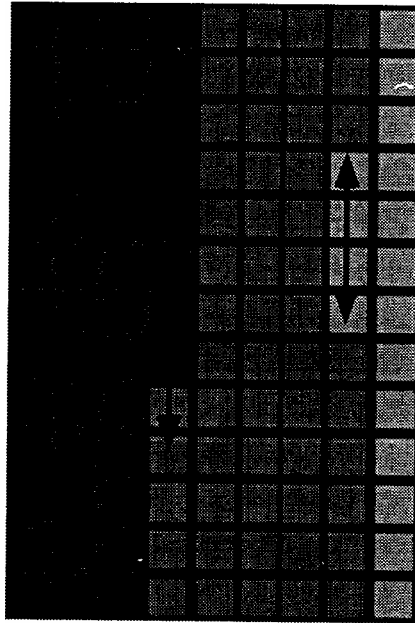


Figure 2.7: Variation in the surface terrace length with temperature. As the surface temperature increases the equilibrium distance between terraces also increases.

Growth will occur by adatoms sticking to the surface and migrating laterally and attaching to kink sites along ledges. Thus, in ideal step growth, adatoms attach to kink sites, which progress the kink site along the ledge as in Figure 2.8. In this way the growth proceeds perpendicular to a ledge until no kink sites exist within X_i of the adatom, then a new kink site is generated on the ledge and the ledge grows parallel to the ledge surface. As ledges fill new surface sites (A sites) become more stable and new nucleating centers are generated and the layer thickness increases. In theory a vicinal surface, *i.e.* a surface polished slightly off axis by a few degrees, will enhance step flow growth by creating an initial surface that has a preferred ledge direction. Now, instead of ledges filling in as growth proceeds, all ledges grow in one direction.

For this ideal step flow growth to occur the surface diffusion length, X_i must be on the order of the distance between ledges, λ_l or greater. However, if the surface temperature is too low with respect to ΔG , and all impinging fluxes, then D_i will decrease X_i and if X_i is less than λ_l some adatoms

TOP VIEW



SIDE VIEW

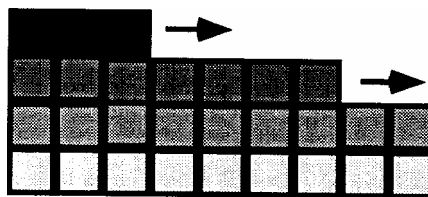


Figure 2.8: During step flow growth the mean diffusion distance is greater the ledge separation and growth proceeds by advancing kink site along a ledge

will not reach the ledge sites. This will results in a rough surface as nucleation centers develop between ledges. The nature of these centers depends on what limits ΔG , in particular, whether it is the Ga or As flux. If a high flux of either of the i th component (metal) or an impurity species is present, then these species lock to form critical size in-

plane nucleating centers, often called pillboxes. While if the limiting flux is of the other species (As) or some impurity species, Ga adatoms will be locked into place from above by the As and more 3-D like islands form and the roughness has a more 3-D nature. In practice the low fluxes and hence low growth rates, as well as the delicate critical balance between each of the fluxes and the growth temperature make step flow growth generally impractical. However, in practice it is not difficult to balance the As to Ga flux ratios, especially with using the valved cracker designs, so that 2-D nucleating centers are present. When the growth begins the surface goes through a period of cycling where pillboxes develop on a smooth surface, they grow to consume half of the surface, then fill in the surface ending the cycle. The surface roughness cycles as well, where it is maximally rough when half of the surface is consumed by the pillbox structures. This cycling gradually fades as the surface evolves to some equilibrium roughness representing some equilibrium density of nucleating centers. RHEED is typically used to measure the roughness evolution by correlating the scattering of the glancing angle electron beam with surface roughness. In the ideal case of step flow growth the surface topology is unchanged and so no variation in the RHEED intensity is observed.

The ideal type of surface roughness depends on the application. For exciton physics where the particle radius is approximately 100\AA , the small scale roughness at intermediate to low temperatures is optimal, while other optical applications, where point defects and impurity incorporation that are present at low temperatures become important problems, higher growth temperatures are more desirable.

The equilibrium surface roughness of stable and a growing surface has been discussed. Thermodynamic energy balances dictate the type of stable facets that form surfaces. At low and medium temperatures, the surface roughness on these surfaces is kinetically limited. As the surface temperature increases, surface diffusion lengths increase and the average terrace length increases. However, the entropy of mixing and the minimum As flux required to stabilize the surface also increases with increasing surface temperature creating more in-plane and vertical roughness variation leading to larger roughness amplitudes and wavelengths. The effect of lattice mismatch strain has not been discussed.

In this work the mismatch strain affect on the surface state dominants all of the above effects. Using the concepts developed in this section, strain perturbation on the surface topology is discussed next.

2.2.2 STRAIN INDUCED SELF-ASSEMBLY

Now suppose that heteroepitaxy has begun and In adatoms are supplied to the GaAs surface. The surface diffusivity of In is higher than Ga on the (100) GaAs surface. However, the InAs lattice constant (6.03 Å) is 7% larger than the GaAs lattice constant (5.65 Å). Because the mismatch is not too large InAs can be initially deposited epitaxially on GaAs. As InAs is deposited on the GaAs the InAs is tetragonally distorted to fit on the GaAs lattice. As shown in Figure 2.9 in the growth plane the InAs has contracted and now has the GaAs lattice constant, while vertically, in the growth direction, the InAs has expanded in an effort to conserve volume. Because the lattice mismatch is small enough, at least initially the lattice mismatch is accommodated by tetragonal distortion and the epilayer remains commensurate with the substrate and is pseudomorphically strained. The strain is defined as the proportional change in length, and is equal to the lattice mismatch. The extra energy associated with this strain, the strain energy is equal to the product of the stress (the force acting in a crystalline direction) and the strain (displacement),

$$E = \iint \sigma_i d\varepsilon_i dz = \iint c_{i,j} \varepsilon_j d\varepsilon_i dz = \frac{1}{2} \int c_{i,j} \varepsilon_i \varepsilon_j dx \quad (2.10)$$

where E is the strain energy per unit in-plane area.

The accumulated strain energy increases with the deposition thickness and is elastic in the sense that if the heteroepitaxy is detached from the substrate the crystal would in principle relax back to its natural lattice constant. At some deposition thickness the energy associated with generating a defect, such as a dislocation, will be lower than this accumulated strain energy and the InAs deposition will plastically relax. In its equilibrium form this critical thickness was first proposed in [74].

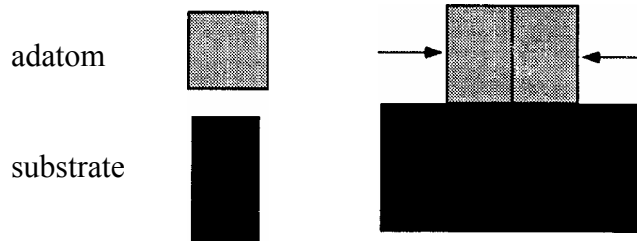


Figure 2.9: Biaxial compression, of a larger lattice that is epitaxially deposited on a smaller lattice. Here the lattice mismatch is small enough so that elastic compression is possible and the epitaxy is pseudomorphic.

Well before this critical thickness, the surface undergoes several structural changes to accommodate the different chemical species and its different lattice constant. The surface reconstruction changes because the chemical and structural differences of the new chemical species on the surface. The size difference of the new species also changes the energetics associated with each of the surface sites discussed above and in Figure 2.6. As shown in Figure 2.10, site C which was the lowest energy site on the unstrained surface is now unfavorable because the adatom is contracted on all sides. In fact, the least energetically favorable sites on the unstrained surface, A sites, now become the most favorable attachment site. The activation energy ΔG at site C is reduced on this mismatch epitaxy surface, and surface sites are energetically more attractive. Because the epitaxial lattice is not completely rigid, some lattice relaxation occurs. Thus, the further adatoms are from the heterointerface, the more they are relaxed toward their equilibrium lattice constant, and so the lower the attachment energy. The poor in-plane (C sites) attachment energetics and the better attachment preference further from the interface combine to roughen the heteroepitaxial surface. If kinetics are favorable the resulting surface will contain islands of material, minimizing flat, planar attachments, while maximizing the amount of hetero-material that is deposited away from the heterointerface. Thus, in

heteroepitaxy where the mismatch strain energy is large enough to be a competing driving force but small enough to be elastically accommodated through biaxial compression, the equilibrium surface is roughened. However, there is an opposing energy term, γ from Equation 2.5 that increases with increasing surface area. How large must this strain be to drive the surface to roughen and to what extent does this roughening proceed? This question can be answered by a simple energy balance in thermodynamic equilibrium, where the two forces in question are the energy related to the surface tension, γ , and the strain energy.

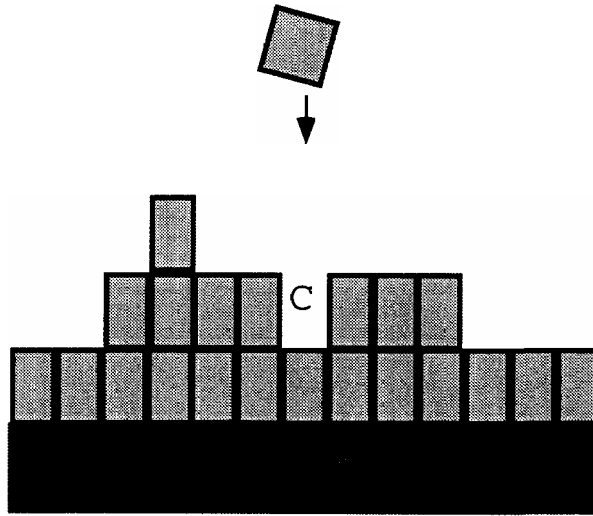


Figure 2.10: The energetics of surface attachment sites on a strained surface are different than on the unstrained surface. Site C is no longer an energetically favorable attachment site.

$$\mu = \mu_0 + \left(\Omega K \gamma + \frac{1}{2} S_{ijkl} \sigma_{ii} \sigma_{kl} \right) \quad (2.11)$$

where, μ_0 is the chemical potential of the flat surface, Ω is the molecular volume, γ is the surface tension, K is the surface curvature and $\frac{1}{2} \sigma_{i,j} \varepsilon_{i,j} = \frac{1}{2} S_{ijkl} \sigma_{ii} \sigma_{kl}$ is the strain energy

density developed in Equation 2.7. There is a simplification inherent in using μ_0 in

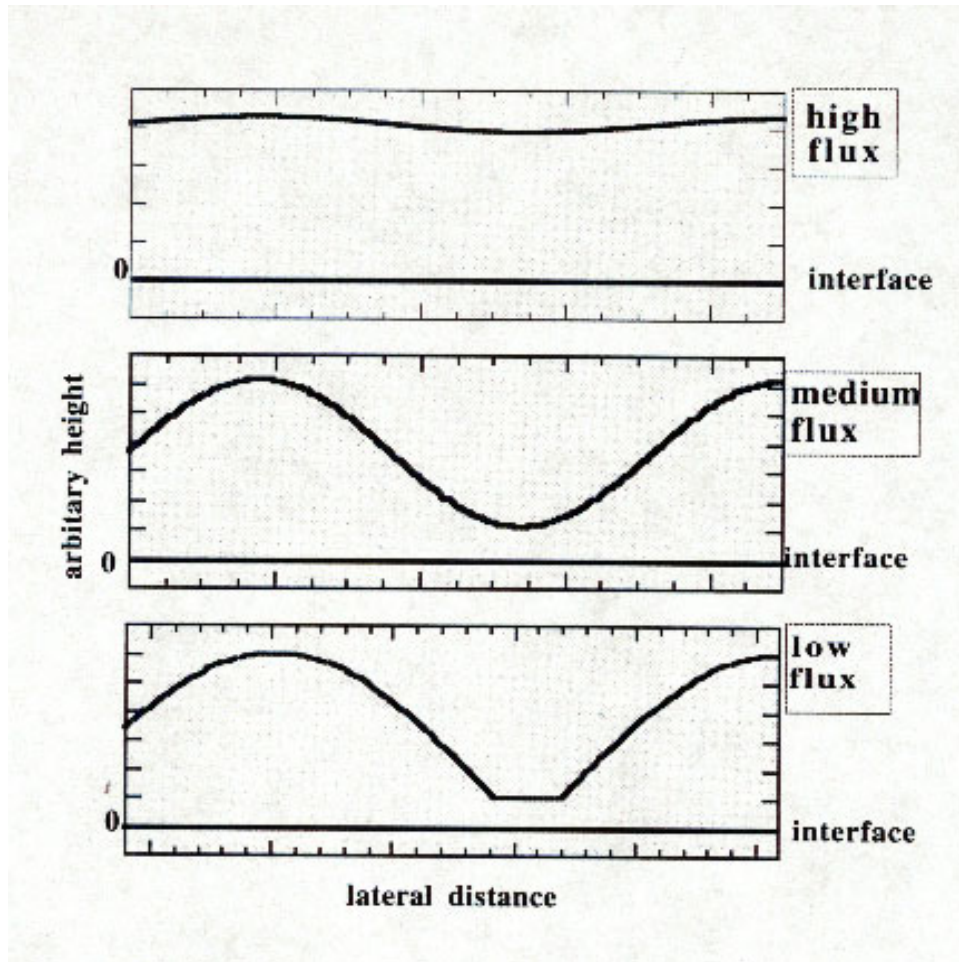


Figure 2.11: Schematic of surface profile when the surface diffusion length is reduced by increased flux and long wavelength surface roughness becomes kinetically unfavorable

Equation 2.11 that serves us well here since we are not too concerned about the details. The quantity μ_0 is not a realistic quantity since it is the equilibrium chemical potential of heteroepitaxy, say InAs on GaAs, when the surface is flat and unstrained. In addition, there is no entropy of mixing term or the effect of mixing on strain energy. If subsurface solid phase diffusion can be ignored, the lack of such mixing terms is appropriate, in fact subsurface solid phase diffusion has been observed in InAs/GaAs growth in the accumulation of InAs on the surface of InAs/GaAs layered structures [75]. γ , the surface tension is over simplified since it is anisotropic and depends on the ledge density. However, Equation 2.11 does show the basic energy balance between the strain energy

and surface energy. The strain energy density is relieved by creating more surface, which increases the surface energy. From this energy balance it is easy to see that small wavelength roughness will create too much extra surface area and will not be stable, while larger wavelength roughness may be more stable because the additional surface area is less. Kinetics has not been considered and before these effects are specifically included in Equation 2.11, some general observations about the kinetic effects can be made. Equation 2.11 is in the thermodynamic limit, the case when the growth rate and flux ratios (V/III) are low, and the surface temperature high enough for appropriately large $X_{s,s}$. Immediately clear is that very large wavelength fluctuations will not be stable because X_l will always be finite. As the growth rate or flux ratio increases, or the surface temperature decreases, the largest stable roughness wavelength will decrease. This is schematically shown in Figure 2.11.

The incorporation of kinetic effects into Equation 2.11 was first demonstrated by Mullins [76]. Asaro [77] cast the derivation within the context of stable surface roughness and the derivation here follows in that spirit except that additional terms are kept so that the solution may be better applied to islanding. Srolovitz [78] has revisited the problem and contrasted this stable roughness with surface nucleation. Kinetic effects can be incorporated into the thermodynamic energy balance of Equation 2.11 by solving for the surface diffusion as a function of the chemical potential [76]. The Nernst-Einstein relation describes the velocity of surface atoms in response to local changes in chemical potential,

$$V = -\frac{D_s}{kT} \frac{\partial \mu}{\partial s} \quad (2.12)$$

while the surface flux of adatoms is

$$J = -\frac{D_s \Omega}{kT} \nabla \mu \quad (2.13)$$

By taking the surface divergence of the flux the adatom accumulation is found, which can be changed to a growth rate normal to the curved surface by multiply by the atomic volume,

$$r_n = \frac{\partial J}{\partial s} \Omega = -\frac{\Omega^2 D_s}{kT} \nabla_s^2 \mu \quad (2.14)$$

The growth rate normal to the surface, r_n , can be converted to the surface growth rate, $\frac{\partial y}{\partial t}$ by recognizing that r_n is the projection of $\frac{\partial y}{\partial t}$ on to the surface,

$$\frac{\partial h}{\partial t} = \frac{\partial y}{\partial t} = r_n \left(1 + \left(-\frac{\partial y}{\partial x} \right)^2 \right)^{\frac{1}{2}} \quad (2.15)$$

Now return to Equation 2.11. First, similar to Equation 2.15 the curvature, K can be defined as

$$K = -\frac{\partial^2 y}{\partial x^2} \left(1 + \left(\frac{\partial y}{\partial x} \right)^2 \right)^{\frac{3}{2}} \quad (2.16)$$

If $\frac{\partial y}{\partial x} \ll 1$ this reduces to $K = h_{xx}$.

The stresses, $\sigma_{i,j}$ on the traction free surface are defined as

$$\begin{aligned} \sigma_{\tau\tau} &= \sigma_{xx} \cos^2 \theta + \sigma_{yy} \sin^2 \theta + 2\sigma_{xy} \cos \theta \sin \theta, \\ \sigma_{\tau n} &= \sigma_{nn} = 0 \quad \text{along the surface,} \end{aligned} \quad (2.17)$$

where τ and n are the surface and surface normal directions, respectively. To solve for $\sigma_{\tau\tau}$ assume an Airy solution for the total stress potential. Equation 2.11 contains stress terms

which are not specifically related to the curved surface. If the stress on the planar surface is σ , and using Equation 2.16 the energy balance of Equation 2.11 can be rewritten as,

$$\mu(x) = \mu_0^* - \gamma \Omega h_{xx} + \frac{1}{2} (\partial_{rr}(x)^2 - \partial^2) 2 \frac{\Omega}{2M}, \quad (2.18)$$

where M is the elastic modulus and μ^* is the reference surface chemical potential including planar strain effects.

The Airy function solution includes both the sinusoidal variation across the surface and the exponential decay away from the interface, and thus represents the important features of the stress. The Airy solution has the form,

$$\Phi = \frac{\sigma_y^2}{2} + (A + B_y) \exp^{-ky} \sin(kx), \quad (2.19)$$

and taking respective derivatives,

$$\begin{aligned} \Phi_y &= \sigma_y + (-k(A + B_y) + B) \exp^{-ky} \sin(kx) \\ \Phi_x &= -k(A + B_y) \exp^{-ky} \cos(kx) \\ \Phi_{yy} &= \sigma_{xx} = \sigma + \{-k[-k(A + B_y) + B] \exp^{-ky} - kB \exp^{-ky}\} \sin(kx) \\ &= \sigma + [k^2(A + B_y) - 2Bk] \exp^{-ky} \sin(kx) \\ \Phi_{xx} &= \sigma_{yy} = -k^2(A + B_y) \exp^{-ky} \sin(kx) \\ \Phi_{xy} &= -\sigma_{yx} = -k(-k(A + B_y) + B) \exp^{-ky} \cos(kx). \end{aligned} \quad (2.20)$$

Inserting these expressions into Equation 2.17 and using $\sigma_{nn} = \sigma_{nt} = 0$, and assuming the surface has the form $h(x) = \Delta \sin(kx)$, $A = 0$, $B = -\sigma\Delta$, and the stresses become

$$\begin{aligned} \sigma_{xx} &= \sigma (1 - k\Delta (ky - 2) \exp^{-ky} \sin(kx)) \\ \sigma_{yy} &= \sigma k^2 \Delta y \exp^{-ky} \sin(kx) \\ \sigma_{xx} &= \sigma k^2 \Delta (1 - yk) \exp^{-ky} \cos(kx) \end{aligned} \quad (2.21)$$

Now the normal stress perpendicular to the surface can be calculated using Equation 2.17 and the above equations (2.21),

$$\begin{aligned}\sigma_{\tau\tau} = & \sigma (1 - k\Delta (ky - 2) \exp^{-ky} \sin(kx)) \cos^2(kx) \\ & + (\sigma k^2 \Delta y \exp^{-ky} \sin(kx)) \sin^2(kx) \\ & + (\sigma k^2 \Delta (1 - ky) \exp^{-ky} \cos(kx)) \sin(kx) \cos(kx) .\end{aligned}\quad (2.22)$$

Since we have assumed a profile of the form $h(x) = \sin(kx)$ and $\sigma_{\tau\tau}$ reduces to

$$\sigma_{\tau\tau} = \sigma (1 - k^2 y \exp^{-ky} h(x) (\sin^2(kx) - \cos^2(kx)) + 2k \exp^{-ky} \cos^2(kx)) .\quad (2.23)$$

Now, assume $h_x = \tan(kx)$ and that $h_x \ll 0$ is small so that terms smaller than h_x , of order $O(h_x)^2 \ll 1$. Thus $\cos^2(kx) \rightarrow 1$ and $\sin^2(kx) \rightarrow 0$ and

$$\sigma_{\tau\tau} = \sigma (1 - k^2 y \exp^{-ky} h(x) + 2k \exp^{-ky} h(x)) .\quad (2.24)$$

σ equals the stress on a planar surface, so that the square of the stress due to the curved surface is

$$\left(\sigma_{\tau\tau}^2(x) - \sigma^2 \right) \frac{\Omega}{2M} = \sigma^2 \left(\left(1 - k^2 y \exp^{-ky} h(x) + 2k \exp^{-ky} h(x) \right)^2 - 1 \right) \frac{\Omega}{2M} .\quad (2.25)$$

Now we would like to calculate $\frac{\partial y}{\partial t}$ from Equation 2.15. The surface growth rate, r_n is found in equation 2.14, and $\nabla_s^2 \mu$ can be calculated from Equation 2.18, using the Equation 2.25, above. Thus,

$$\begin{aligned}\frac{\partial^2 \mu}{\partial s^2} = & -\gamma \Omega h_{xxxx} + \left(\sigma_{\tau\tau}^2(x) - \sigma^2 \right) \frac{\Omega}{2M} \\ = & -\gamma \Omega h_{xxxx} + \frac{\sigma^2 \Omega}{2M} \left(\left(1 - k^2 y \exp^{-ky} h(x) \right)^2 - 1 \right)\end{aligned}\quad (2.26)$$

$$\frac{\partial h(x,t)}{\partial t} = -\frac{D_s \gamma \Omega^2}{kT} h_{xxxx} + \frac{D_s \gamma \Omega^2}{kT} \frac{\sigma^2}{2M} \left(\left(1 - k^2 y \exp^{-ky} h(x) + 2k \exp^{-ky} h(x) \right)^2 - 1 \right)_{xx}\quad (2.27)$$

Defining $C = \frac{D_s \Omega^2}{kT}$, this reduces to

$$\frac{\partial h(x,t)}{\partial t} = -Ch_{xxxx} + \frac{C\sigma^2}{2M} (2k^3 \exp^{-ky} \Delta \sin(kx)(2-ky)) \quad (2.28)$$

Now use a trial function, $h(x) = \Delta \sin(kx)$ so that

$$\frac{\partial h(x,t)}{\partial t} = \left(C\gamma k^4 + \frac{C\sigma^2}{M} k^3 \exp^{-ky} (2-ky) \right) h(x). \quad (2.29)$$

and integrate to get the thickness as a function of position and time,

$$h(x,t) = h_0 \exp \left(\left(-C\gamma k^4 + \frac{C\sigma^2}{M} k \exp^{-ky} (2-ky) + V_g \right) t \right). \quad (2.30)$$

According to Equation 2.29 at any reference thickness (taking $y=0$) the surface is unstable to roughening for

$$\lambda_c = \frac{\pi\gamma M}{\sigma^2} \quad (2.31)$$

and the maximum wavelength is

$$\lambda_{\max} = \frac{4}{3} \frac{\pi\gamma M}{\sigma^2} = \frac{4}{3} \lambda_c \quad (2.32)$$

The critical wavelength and maximum wavelength are not dependent on the growth parameters but the amplitude for each wavelength is dependent on the growth parameters. In Figure 2.12, the distribution of wavelengths is shown for two different surface diffusion coefficients. The critical wavelength, λ_c is at the crest of the wavelength distribution. The roughness wavelengths are proportional to the surface tension γ and inversely proportional to the square of the stress. As the surface tension increases, so does

the critical wavelength at which surface roughness will be stable. As the lattice mismatch increases, the stress increases and the critical wavelength at which roughening

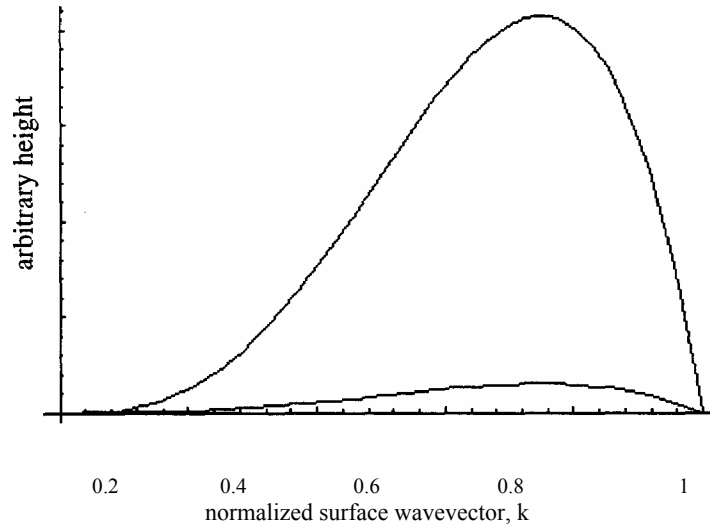


Figure 2.12: The critical wavevector (maximum k) and wavevector with the maximum amplitude using two different surface diffusivity terms. Only the amplitudes are affected by the change in surface diffusivity

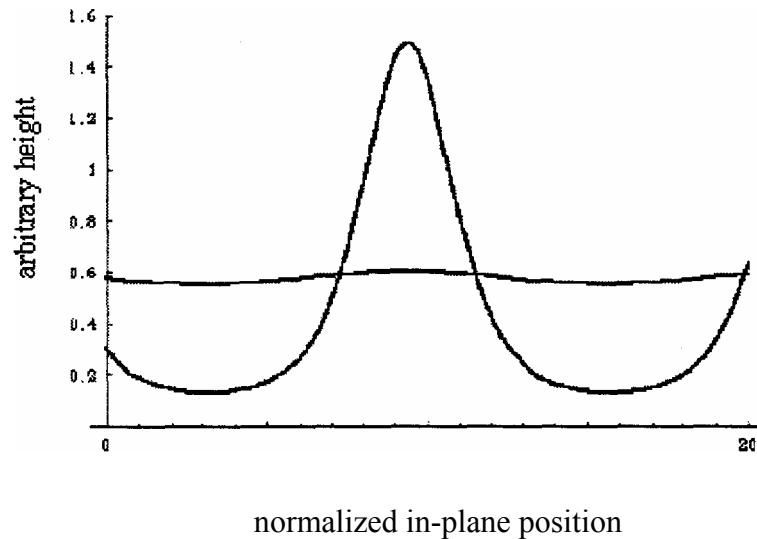


Figure 2.13: The surface topology is estimated using Equation 2.30 under large and small surface diffusivity. The diffusivity and the growth rate establish the state of surface roughness.

is stable is reduced. Since the growth parameters only affect the amplitudes of these wavelengths the growth parameters can not inhibit the tendency of the surface to

roughen, but the growth parameters can minimize the roughening by reducing the wavelength amplitudes. In Figure 2.13 the shape of the surface is calculated using Equation 2.30 for two different values of surface diffusivity. For the small diffusivity case, the growth rate dominates the surface diffusivity terms and planarizes the surface.

Combining a thermodynamic expression for the chemical potential for the strain surface with surface kinetics through the Nernst-Einstein equation a general expression for the surface topology has been found (Equation 2.30). From this expression $\lambda_{critical}$ and λ_{max} have been determined and are expressed in Equations 2.31, and 2.32. Thus a surface phase transition from planar growth to a roughened growth front will occur at some thickness which is dependent on the lattice mismatch and the surface properties of the epitaxy (γ). This is not clearly an islanding surface but simply a rough surface.

However, as the accumulated strain energy increases so does σ^2 which amplifies the effect of the e^{-ky} term in Equation 2.30. The result is that the amplitude begins to increase and the growth front at $\lambda = \frac{3\pi}{2}$ begins to impinge on the heterointerface. This is the beginning of another phase transition to the islanding growth surface. The growth surface becomes flattened just near the heterointerface as more material is transferred the positive (island) regions of the roughness wave. As growth continues, if the accumulated strain energy is still increasing because surface roughening does not completely eliminate the mismatch strain, the stable wavelength will continue to decrease and the amplitudes will continue to increase. The islands will grow taller and fatter and at some point adjacent islands will impinge on each other. At this point the accumulated strain energy dramatically increases as the surface curvature is diminished. The epitaxy will continue to grow with increasing strain energy until some other relaxation process becomes energetically favorable.

What are the constraints on Equation 2.30 and is this expression valid through the roughening phase and into the islanding phase? An approximation used in Equation 2.24 is that $\cos^2\theta \rightarrow 1$, and $\sin^2\theta \rightarrow 0$ so θ the angle of the surface tangent with respect to the

previous planar surface must be small. In the islanding cases discussed in the next chapter, the island height is typically 40 Å while the island diameter is approximately 180 Å. Thus if the islanding wavelength is assumed to be 360 Å θ is approximately 6° and $\sin^2 \theta \sim 0.01$ and the assumptions are appropriate. Thus the transition to roughening is generally actually represented by Equation 2.30. More troubling is the transition from the rough surface to the island surface where a discontinuity of the derivative (and second derivative) occurs at the island edge. Mathematically, the surface wave is extended through the heterointerface and Equation 2.30 could still be valid if the stress fields of adjacent islands overlap. However an alternative approach, such as the numerical solutions developed in [79], exists and is probably better suited for this phase region.

Four epitaxial growth regimes have been delineated. Initially the epitaxial growth is planar. The strain energy increases and a transition to a roughened growth front regime occurs. As the roughened growth front develops, the roughness wavelength amplitude increases, the troughs impinge on the heterointerface and a change to an islanding surface regime results. These two transitions elastically relieve the mismatch strain; however, the strain may also be reduced plastically through dislocation generation or other structural defects. It will be shown in the coming chapter that plastic relaxation does occur in these structures but that for some growth region, the islanding surface is present. Thus, because of the particular material system, the energy to initiate a dislocation is less than the energy to initiate surface roughening and then surface islanding.

The transition from the planar to the islanding growth surface describes a phenomenological growth mode called Stranski-Krastanov growth. This growth mode is characterized by an initial wetting layer region in which the growth is planar, followed by the transition to the islanding region. Two other growth modes are typically discussed: Van de Merwe growth, which is always planar, and Volmer-Weber growth which is always 3-D. Although Stranski-Krastanov growth often is only a transitional growth regime between planar and fully developed 3-D growth, it is a distinct regime. The islanding growth that has been discussed here is not the truly classical Volmer-Weber growth because adatoms still diffuse long distances along the surface. In Volmer-Weber

growth the extremely rough surface exists because the surface diffusivity is extremely low [74].

2.3 Characterization Techniques

Characterization techniques used to collect research data for this dissertation deserve description to help understand the experimental results presented. This section divides into three subsections. Section 2.3.1 provides a somewhat more detailed overview of atomic force microscopy [80] that has been our primary tool throughout this study. It is particularly valuable to observe nano-scale surface topology directly and, thus, characterize strain induced islanding statistics dependency on growth parameters.

Section 2.3.2 is devoted to transmission electron microscopy (TEM) [81] which is a unique instrument for direct investigation of strain induced self-assembled InAs quantum dots embedded into the crystal matrix of the host material (GaAs). TEM has been used successfully to prove the quantum dot column formation when multiple layers of InAs dots are deposited and then covered with GaAs capping layers to produce 3-dimensional QD ensembles in GaAs matrix.

Section 2.3.3 describes optical spectroscopy and electrical measurements performed that are not as direct as the two previous methods, but have significant practical importance as they closely relate to possible optoelectronic and electronic device applications.

2.3.1 ATOMIC FORCE MICROSCOPY

The Atomic Force Microscope (AFM) is being used to solve processing and materials problems in a wide range of technologies affecting the electronics, telecommunications, biological, chemical, automotive, aerospace, and energy industries. The materials being investigated include thin and thick film coatings, ceramics, composites, glasses, synthetic and biological membranes, metals, polymers, and semiconductors. The AFM is being

applied to studies of phenomena such as abrasion, adhesion, cleaning, corrosion, etching, friction, lubrication, plating, and polishing. By using AFM one can not only image the surface in atomic resolution, but also measure the force at nano-newton scale. Publications related to the AFM have grown very rapidly since its birth.

The first AFM was made by meticulously gluing a tiny shard of diamond onto one end of a tiny strip of gold foil. In the fall of 1985 Gerd Binnig and Christoph Gerber [82] used the cantilever to examine insulating surfaces. A small hook at the end of the cantilever was pressed against the surface while the sample was scanned beneath the tip. The force between tip and sample was measured by tracking the deflection of the cantilever. This was done by monitoring the tunneling current to a second tip positioned above the cantilever. They could delineate lateral features as small as 300 \AA . The force microscope emerged in this way. In fact, without the breakthrough in tip manufacturing, the AFM probably would have remained a curiosity in many research groups. It was Albrecht, a fresh graduate student, who fabricated the first silicon micro-cantilever and measured the atomic structure of boron nitride [83]. Today the tip-cantilever assembly typically is micro-fabricated from Si or Si_3N_4 . The era of AFM came finally when the Zurich group released the image of a silicon (111) 7×7 pattern [84]. The world of surface science knew that a new tool for surface microscope was at hand. After several years research the fabrication of micro-cantilevers has been perfected, and the instrument has been extensively embraced by scientists and technologists.

The force between the tip and the sample surface is very small, usually less than 10^{-9} N. How to monitor such small forces is another story. The detection system does not measure force directly. It senses the deflection of the micro-cantilever. The detecting systems for monitoring the deflection fall into several categories. The first device introduced by Binnig [82] was a tunneling tip placed above the metallized surface of the cantilever. This is a sensitive system where a change in spacing of 1 \AA between tip and cantilever changes the tunneling current by an order of magnitude. It is straightforward to

measure deflections smaller than 0.01 \AA . Subsequent systems were based on the optical techniques. The interferometer is the most sensitive of the optical methods, but it is somewhat more complicated than the beam-bounce method, which was introduced by Meyer and Amer [85]. The beam-bounce method is now widely used as a

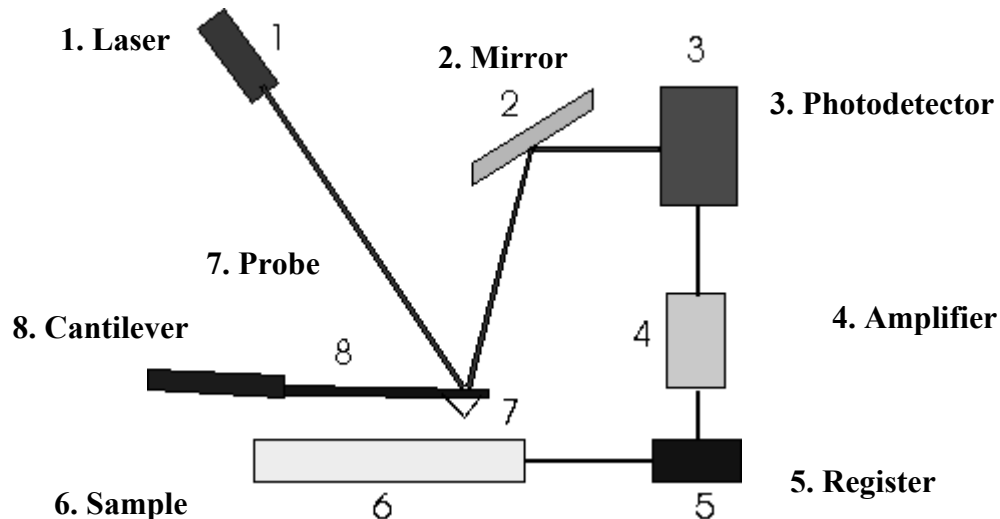


Figure 2.14: Schematic of an Atomic Force Microscope.

result of the excellent work by Alexander and colleagues [86]. In the system shown on Figure 2.14, an optical beam is reflected from the mirrored surface on the back side of the cantilever (8) onto a position-sensitive photodetector (3). In this arrangement, a small deflection of the cantilever will tilt the reflected beam and change the position of the beam on the photodetector.

The principles on how the AFM works are very simple. An atomically sharp tip (7) is scanned over a surface with feedback mechanisms that enable the piezo-electric scanners to maintain the tip at a constant force (to obtain height information), or height (to obtain force information) above the sample surface. Tips are typically made from Si_3N_4 or Si, and extended down from the end of a cantilever (8). The nanoscope AFM head employs an optical detection system in which the tip is attached to the underside of a reflective cantilever. A diode laser (1) is focused onto the back of a reflective cantilever. As the tip

scans the surface of the sample, moving up and down with the contour of the surface, the laser beam is deflected off the attached cantilever into a dual element photodiode (3). The photodetector measures the difference in light intensities between the upper and lower photodetectors, and then converts to voltage. Feedback from the photodiode difference signal, through software control from the computer, enables the tip to maintain either a constant force or constant height above the sample. In the constant force mode the piezo-electric transducer monitors real time height deviation. In the constant height mode the deflection force on the sample is recorded. The latter mode of operation requires calibration parameters of the scanning tip to be inserted in the sensitivity of the AFM head during force calibration of the microscope. The primary purpose of these instruments is to quantitatively measure surface roughness with a nominal 5 nm lateral and 0.01 nm vertical resolution on all types of samples. Depending on the AFM design, scanners are used to translate either the sample under the cantilever or the cantilever over the sample. By scanning in either way, the local height of the sample is measured. Three dimensional topographical maps of the surface are then constructed by plotting the local sample height versus horizontal probe tip position.

Most of the AFM images used in this dissertation were obtained in the contact mode where the tip scans the sample in close contact with the surface is the common mode used in the force microscope. The force on the tip is repulsive with a mean value of 10^{-9} N. This force is set by pushing the cantilever against the sample surface with a piezoelectric positioning element. In contact mode AFM, the deflection of the cantilever is sensed and compared in a DC feedback amplifier to some desired value of deflection. If the measured deflection is different from the desired value, the feedback amplifier applies a voltage to the piezo to raise or lower the sample relative to the cantilever to restore the desired value of deflection. The voltage that the feedback amplifier applies to the piezo is a measure of the height of features on the sample surface.

2.3.2 TRANSMISSION ELECTRON MICROSCOPY

Another powerful characterization tool used in our research is a transmission electron microscope (TEM) that allowed investigation of quantum dot structures

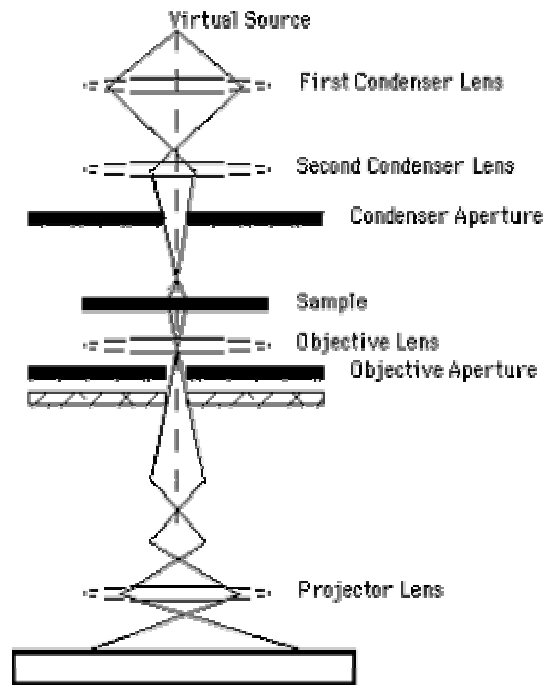


Figure 2.15: Schematic of a transmission electron microscope

embedded in the host matrix. Samples for TEM must be specially prepared to thicknesses which allow electrons to transmit through the sample, much like light is transmitted through materials in conventional optical microscopy. Because the wavelength of electrons is much smaller than that of light, the optimal resolution attainable for TEM images is many orders of magnitude better than that from a light microscope. Thus, TEMs can reveal the finest details of internal structure - in some cases as small as individual atoms. Magnifications of 350,000 times can be routinely obtained for many materials, whilst in special circumstances, atoms can be imaged at magnifications greater than 15 million times.

Schematic of a transmission electron microscope is presented on Figure 2.15. The virtual source at the top represents the electron gun, producing a stream of monochromatic electrons. This stream is focused to a small, thin, coherent beam by the use of condenser lenses 1 and 2. The first lens (usually controlled by the "spot size knob") largely determines the "spot size"; the general size range of the final spot that strikes the sample. The second lens (usually controlled by the "intensity or brightness knob" actually changes the size of the spot on the sample; changing it from a wide dispersed spot to a pinpoint beam.

The beam is restricted by the condenser aperture - a thin (<100 micron thick) disk or strip of metal (usually Pt) with a small (2-100 micron) circular through-hole used to filter out unwanted high angle scattered electrons before image formation. The beam strikes the sample originating a number of interaction with the sample material and producing: backscattered electrons, that are caused by an incident electron colliding with an atom in the specimen which is nearly normal to the incident's path, the incident electron is then scattered "backward" 180 degrees; secondary electrons driven by incident electron passing "near" an atom in the specimen, near enough to impart some of its energy to a lower energy electron (usually in the K-shell), thus causing a slight energy loss and path change in the incident electron and the ionization of the electron in the specimen atom, so that ionized electron then leaves the atom with a very small kinetic energy (5eV); Auger electrons and X-rays caused by the de-energization of the specimen atom after a secondary electron is produced; and, finally, transmitted beams consisting of unscattered, elastically and inelastically scattered electrons. This transmitted portion is focused by the objective lens into an image. Optional Objective and Selected Area metal apertures can restrict the beam; the Objective aperture enhancing contrast by blocking out high-angle diffracted electrons, the Selected Area aperture enabling the user to examine the periodic diffraction of electrons by ordered arrangements of atoms in the sample. The image is passed down the column through the intermediate and projector lenses, being enlarged all

the way. Finally, phosphorous screen allows user to observe and record the image. The darker areas of the image represent those areas of the sample that fewer electrons were transmitted through (thicker or denser). The lighter areas of the image represent those areas of the sample that more electrons were transmitted through (thinner or less dense).

2.3.3 OPTICAL AND ELECTRICAL MEASUREMENTS

To compliment physical observations of nano-scale objects obtained using the two techniques described above with evidence that these very small islands are indeed quantum dots optical, primarily of photoluminescence spectra of quantum dot ensembles embedded in GaAs matrix, and electronic measurements of quantum dot column structures were performed.

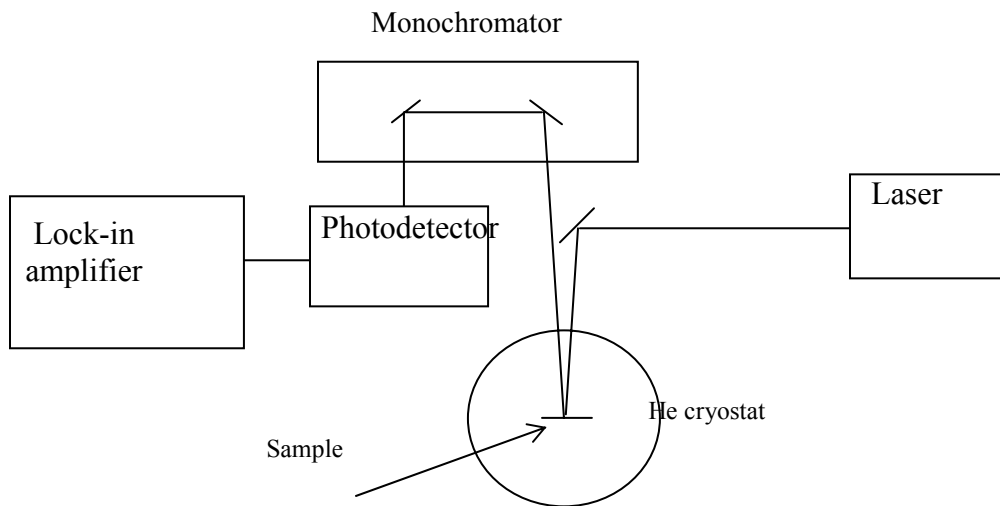


Figure 2.16: Photoluminescence measurement experimental setup.

Typical setup for optical measurements is shown on Figure 2.16: Ar^+ ion laser was used as an optical “pump” source, sample with InAs islands embedded in the GaAs matrix was placed inside liquid He circulation cryostat maintained at 8K, then photoluminescence spectra were collected using monochromator, Ge photodetector, and lock-in amplifier.

Electrical measurements were conducted on samples schematically depicted on Figure 2.17. Quantum dot ensembles were grown epitaxially, using MBE, and then vertical micro-column structures were lithographically defined and fabricated using selective ion etching. Subsequently contact and gate material was deposited to allow study of single electron tunneling in these structures.

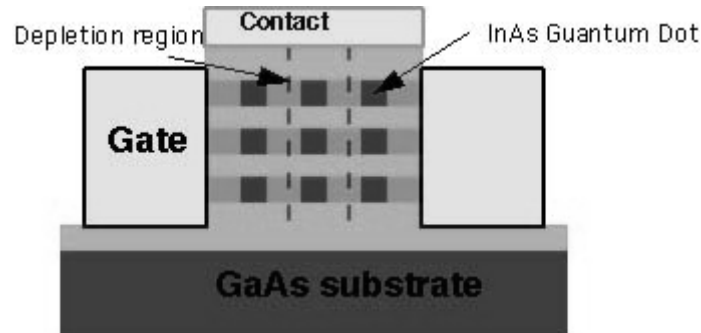


Figure 2.17: Quantum Dot sample for electrical measurements.

2.4 Conclusions

In this chapter a foundation for the following chapters was established. This dissertation is driven by the self-organized crystal growth of InAs quantum dots on GaAs. Therefore, this chapter investigates the crystal growth process from a historical, technical and theoretical standpoint. The advantages of the MBE technique for in-situ monitoring of the crystal growth process and for the ability to produce highly abrupt interfaces were discussed. It is precisely the advances in MBE that produced the initial quantum well and superlattice structures, and it is the monolayer control that allows the Stranski-Krastanov growth mode to be investigated and optimized for quantum dot structures. The energetics of the growing surface were investigated first in the homogeneous, non strain epitaxy. The energy balance was then modified to include strain effects from mismatched epitaxy. An equilibrium phase transition to a roughened growth surface was established using a

minimum critical roughened wavelength criteria based on the strain energy and surface tension. This was then extended to include stable island growth. An expression for the epitaxial thickness as a function of time and position on the surface was found. In this expression, the growth parameters effect the equilibrium surface topology through the surface diffusivity, and the growth rate is a term which directly balances the expression for the equilibrium surface. Thus, the equilibrium surface is partially determined by the growth parameter effects on the surface diffusivity, but this equilibrium surface can be inhibited by a growth rate term. Finally, the use of strain induced islanding as a general self-assembly technique was discussed. The advantage of this technique is that it combines the fabrication of quantum dot-like structures in an epitaxial system. The disadvantage is that this self-assembly system does not produce dots of exactly the same size and shape because the epitaxial forces are the dominant driving forces in the system.

Description of characterization techniques is essential for understanding research data presented in the subsequent chapters.

Chapter 3: Structural and Optical Properties of Strain Induced Quantum Dots

The strain-induced islanding process is a one step process for fabricating quantum dots. In this way the structures can be produced in a fashion similar to structures containing quantum wells; the artificial crystal structure is grown by MBE or another acceptable crystal growth process, and the device is defined by post growth contact evaporations in concert with lithographic processing techniques. This is in contrast to the earlier work in quantum dot fabrication, in which post growth processing is used to fabricate the quantum dot from an epitaxial quantum well structure. In the former case, the concepts used to integrate quantum wells in devices is extended to quantum dots, while in the latter case, quantum wells are used as the building blocks of quantum dots, and thus significant additional processing steps are required.

This new, all growth quantum dot fabrication process requires a careful study of the effects of various growth parameters on the resulting physical, optical and electrical properties of the quantum dot. These studies are all the more basic because the Stranski-Krastanow growth mode has not been studied in depth in the MBE environment, so that little is known about the effects of certain growth parameters on the dot formation process. Thus, the effects of these parameters on the statistical properties of these island ensembles become the defining issue. In this chapter, the effects of several growth parameters on the statistical properties of the island ensembles are investigated. These include substrate temperature, V/III flux ratio, growth rate, the amount of material deposited, and the crystallographic orientation of the substrate. It is found that except for limited experiments using vicinal substrates, all of these parameters have some effect on

the InAs island size and distribution statistics, and translate to variations in optical properties.

This chapter begins with a discussion of the narrow growth window in which these islands can be fabricated in a defect free, controllable form that is necessary for quantum dot applications. Coherent, dislocation free dots can be grown only within a deposition window of 2 monolayers (MLs) or approximately 6 Å of deposited material, and the exact transition point is a function of the growth temperature. The growth temperature and lattice mismatch also effect the islanding process. The second section of this chapter discusses the effects of growth parameters on dot density, which is important for both optoelectronic device applications (high density) and electronic device applications (intermediate density). Although both growth rate and monolayer cover effect the dot density, the most significant effect on dot density is the V/III flux ratio. After key factors influencing islanding are discussed in the Section 3.2 we proceed to theoretical description of quantum confinement in Section 3.3 which establishes the connection between the physical structure of the dots and their optically active electronic states. Photoluminescence is used to observe the effects of changing crystal growth parameters on these states. Section 3.5 focuses on optical properties of ensembles of strain induced quantum dots.

As important as it is to define the general growth parameter space that results in useful islands for quantum dots, it is also shown in this chapter that adjusting these growth parameters has a very limited effect on enhancing the quantum dot properties of the dot ensembles. In the end the two issues limiting the initial complete success of this quantum dot formation technique remain. First, the island or quantum dot size can only be moderately controlled by adjusting the MBE growth parameters, and luminescence remains inhomogenously broadened. More importantly, the size distribution of the dot ensemble can only be marginally reduced by optimizing the crystal growth parameter space. In fact, reduced luminescence linewidths originally associated with narrower size distributions and resulting from changes in the substrate temperature will be correlated to less (not more) uniform dot size distribution. The spectral peak position of these dot

ensembles cannot be shifted very far from its typical position. Second, the in-plane ordering of dots with respect to each other remains an unresolved issue. Although there are many electrical and optoelectrical applications for these structures without in-plane ordering, the addition of such ordering would provide the basis for a device structure that can be easily placed in the current Cartesian circuit layout. This important issue will be discussed in detail in the next chapter.

3.1 Coherently Strained, Defect Free Islands

In heterogenous crystal growth, as more adatoms are deposited onto the growing surface, this growth surface can go through several structural changes that can be as large as the complete loss of epitaxial coherency and as small as a microscopic change in surface roughness or a non-abrupt, diffuse heterointerface. These general effects have been introduced earlier in the Background chapter of this dissertation. The focus of this section is the detailed investigation of structural effects on the growing surface due to small changes in the amount of epitaxially deposited material when the lattice constant difference between the epitaxy and substrate is small. This is the case of the InAs/GaAs system, where the lattice mismatch is approximately 7%. This is considered very large by high quality epitaxial standards but, in fact is small enough to observe the transitional Stranski-Krastanow growth regime. In the Stranski-Krastanow (SK) growth of InAs on GaAs, there is the initial second order phase change between the flat, layer-by-layer growth regime that characterizes ideal MBE growth, and the island growth regime. The island size and shape is predominately determined by the Gibbs free energy balance that was developed in the Chapter 2. This energy balance is

$$\mu = \mu_0 + \frac{1}{2} S_{ijkl} \sigma_{ij}(x) \sigma_{kl}(x) V_0 + \gamma KV_0 \quad (3.1)$$

Here the accumulated strain energy $\frac{1}{2} S_{ijkl} \sigma_{ij}(x) \sigma_{kl}(x) V_0$ and the extra surface energy (γKV_0) associated with islanding contribute to the additional energy terms, where μ_0 is

the total unstrained and planar crystal energy. Note that if the epitaxial lattice mismatch was not present the curvature (γ) that minimizes the system energy is zero, corresponding to a flat surface. Thus, the lattice mismatch strain leads to non-flat growth surface with an island size determined by the minimization of equation 3.1. The phase change from the flat, layer-by-layer surface to the islanding surface may not be a discrete second order phase change, as the growth surface becomes increasingly roughened and this roughness is the seeding for subsequent island growth.

In this section an additional phase change is observed. This phase change is between isolated InAs islands that are only elastically relaxed by the surface topology and larger coalesced islands that are plastically relaxed through dislocation generation. Here, particular attention is paid to the transition, in SK growth, between isolated island growth and the coalesced island regimes in an effort to expand the isolated island SK regime. The transition region is investigated as functions of growth temperature and equivalent InAs layer-by-layer monolayer (MLs) coverage in order to extend the isolated island regime for quantum confinement applications.

Atomic force microscopy (AFM) results on the GaAs (100) growth surface indicate that as the substrate temperature is increased, isolated island SK growth is sustained over larger monolayer coverages. In addition, for constant epitaxial coverage, the island diameter also increases with temperature. An isolated island diameter of 180Å is observed at 500° C when the equivalent of 3 monolayers of InAs surface coverage are deposited. When $\text{In}_{0.5}\text{Ga}_{0.5}\text{As}$ is used rather than InAs, it is observed that the isolated island growth is extended to higher ML coverages and there is a decrease in island concentration compared to the InAs results. It will be shown that these results fit a SK growth model in which the island size and shape are kinetically, not thermodynamically, controlled by surface adatom diffusion.

InAs islands of 180Å in diameter are typically grown. Growth of $\text{In}_{0.5}\text{Ga}_{0.5}\text{As}$ islands indicates an increased 2-D epitaxial region before island nucleation and a decreased island concentration compared to growth of InAs islands. These differences between

InAs and $\text{In}_{0.5}\text{Ga}_{0.5}\text{As}$ are expected because the lattice constant of $\text{In}_{0.5}\text{Ga}_{0.5}\text{As}$ is closer to the lattice constant of GaAs than is the lattice constant of InAs. In all of the experiments in the following section the V/III flux ratio was maintained at 18 for all layers. The growths were conducted with an As_2 flux, which was generated from an As_4 cracking effusion cell. The substrate temperature is typically measured using a thermocouple radiatively coupled to back of the substrate. This is not the real substrate temperature. A correlation between the actual substrate temperature and the temperature measured by the thermocouple was discussed in the Chapter 2. The actual temperature is measured by determining the GaAs bandgap by measuring the transmitted light from the substrate heater. The variation in the band-edge with temperature is known and thus the actual substrate temperature can be determined. Since the bandedge and its variation with temperature are different for doped and undoped substrates, the correlation is different. Since the growth temperature is particularly important for island nucleation, only semi-insulating GaAs substrates were used.

Figure 3.1 shows the transition in the SK growth regime between isolated growth and coalesced growth at 500°C . Figure 3.1a shows isolated islanding at 2 MLs of surface coverage. Below 2 MLs (actually below 1.8 MLs) the epitaxial surface is flat and the growth is planar. With 2 MLs of deposited InAs, the average island diameter is 150\AA .

Transmission-electron microscope (TEM) investigations indicate these islands are defect free. When the equivalent of 3 flat MLs of InAs have been deposited the island size increases slightly and the density of InAs islands also increases. The island size increases simply because more material is deposited and migrates to the islands. The increase in the island density is more complicated and will be discussed in detail in Section 3.2. In general, the increase in density is due to a non uniform wetting layer structure. Because of the lattice mismatch, the critical wetting layer thickness is only 1.8 MLs. Thus small differences in thickness, of the order of 0.2 MLs (0.6 \AA) at different sample positions will result in regions that are still growing planar because this critical wetting layer thickness has not been exceeded and regions that contain islands because the critical wetting layer

thickness has been exceeded. As more material is deposited the planar thickness is exceeded over more regions of the sample and the island density increases.

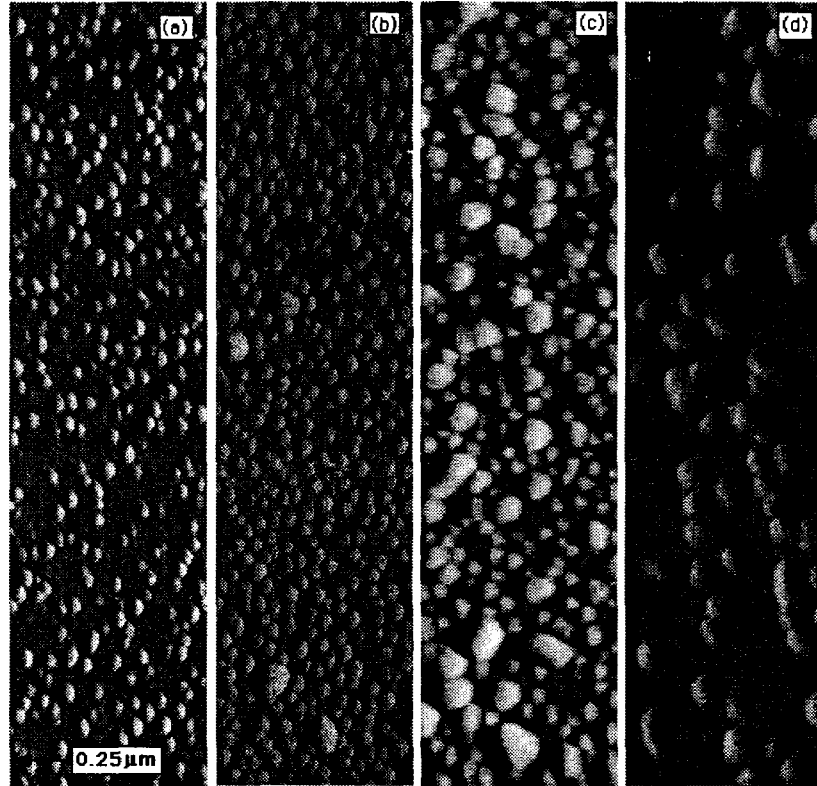


Figure 3.1: Atomic-force microscopy (AFM) images of InAs islands formed from various amounts of InAs deposition at 500°C. (a) is after 2 MLs on InAs, (b) 3 MLs of InAs, (c) 4 MLs of InAs and (d) after 6 MLs of InAs. The InAs islands are not covered with.

When an additional 1 ML of InAs is deposited so that the total InAs deposited is 4 MLs (Figure 3.1c) a change in the surface topology is clearly evident. The distribution in the island size is significantly increased and it appears there are two distinct types of islands. One type of island is large, with an odd, less symmetric shape than the islands in Figure 3.1a or b, while the other type of island is similar to those found in Figure 3.1a and b. It is

believed that the larger islands are formed by the coalescing of isolated islands. These larger islands may have plastically relaxed through dislocation generation before coalescing or the relaxation may have taken place after coalescing. By 6 MLs of InAs deposition, the transition to this large island surface topology is complete. The island density is significantly reduced from Figure 3.1b, the individual island size has increased and the shape is no longer symmetric. Why does the island density and shape change through island relaxation? Initially, the islands are strained. The strain fields from individual islands extend through the GaAs underlayer and inhibit adjacent islands from impinging on each other. The distance between adjacent islands is established early with the roughening of the initial wetting layer region. Surface roughness is present in heteroepitaxial systems, but the large roughness present here is due to the lattice mismatch strain. As deposition continues the island size grows to the point when adjacent islands must impinge on each other and the crystal strain increases to the point where dislocation generation becomes energetically favorable. The island size and shape is determined by the total Gibbs free energy which includes surface, interface and bulk energy terms whose values are cryallographically dependent. Once the islands are relaxed through dislocation generation, the energy balance of Eq. 3.1 is altered and therefore so is the equilibrium shape. The extra surface, needed previously in the strained island case to elastically relieve strain, is now not necessary. The surface energy balance is altered; the strain energy term which balanced the energy component due to increased surface area is absent, and therefore the equilibrium island radius of curvature increases. Since the Gibbs energy is now minimized by reducing the total vacuum interface area, the result is that the island size will grow laterally not vertically, and each island will consume more surface adatoms, which eventually reduce the island density.

The results of Figure 3.1 indicate there is a very narrow deposition window in which strained isolated islands can be fabricated in a reasonably controlled fashion. Below 2 MLs of InAs deposition the epitaxial growth is planar, while at 4 MLs, the individual islands have grown to a size where adjacent islands are coalescing and islands are plastically relaxing through dislocation generation. In all the samples investigated the

Stranski-Krastanow growth mode is present. This is true even in the cases where the islands are relaxed through dislocations. The coalesced, relaxed islanding regime is stable, but it is unclear if the coalesced, relaxed islanding regime remains stable for thicknesses much larger than the 8 MLs of InAs deposition investigated. Certainly, the islands become flatter and less dense with increased depositions, but this is no clear evidence that the growth surface returns to its original planar topology. Such a case would be interesting because it suggests that the islanding regime exists for a very small period during deposition, that the initial and final surfaces are both planar with layer-by-layer growth and there is a small intermediate region where island growth is present until the heteroepitaxy plastically relaxes through dislocations.

From the AFM data in Figure 3.1 the optimum deposition thickness is approximately 3 MLs. In the following experiments the growth temperature is varied and it will be shown that this optimum deposition thickness is a function of the growth temperature. However, 500°C is chosen as the optimum growth temperature so 3 MLs of InAs deposition is typically used.

The substrate temperature affects the strained island - relaxed island phase transition. This effect is related to the strong variation of surface diffusion with growth temperature. The AFM images in Figure 3.2 illustrate the variation in island formation as a function of substrate temperature for 4 MLs of InAs. In the experiments represented in this figure the growth rate was maintained at 0.09 $\mu\text{m/hr}$, while the V/III ratio was maintained at 9. The deposition of 4 MLs corresponded to the boundary of the isolated and strained - coalesced and relaxed island transition at 500°C. In Figure 3.2a, the substrate temperature is 425°C (388°C actual) and islands grow with a broad size distribution. It is not clear from the AFM image whether the islands are strained or have already plastically relaxed. It is believed that because of the low surface diffusivity at this temperature, the surface can not completely transform to its equilibrium shape. The limited surface diffusion impedes the movement of adatoms on the growth surface, resulting in local variations in surface topology. The resulting local surface structure is the result of chance variations in the local deposition rate and underlying surface as the limited surface diffusion inhibits

the degree of thermodynamic equilibrium. Thus, isolated island growth and coalesced island growth are simultaneously present. At 3 ML coverage and 425°C, a roughened 2-D growth is present (not shown). No isolated island-coalescing SK transition is observed at this lower growth temperature, and such a clear transition is inhibited by the limited surface diffusion. In Figure 3.2b the substrate temperature is 500°C (457°C actual), and isolated islands of a uniform diameter begin to coalesce into larger islands. This is the

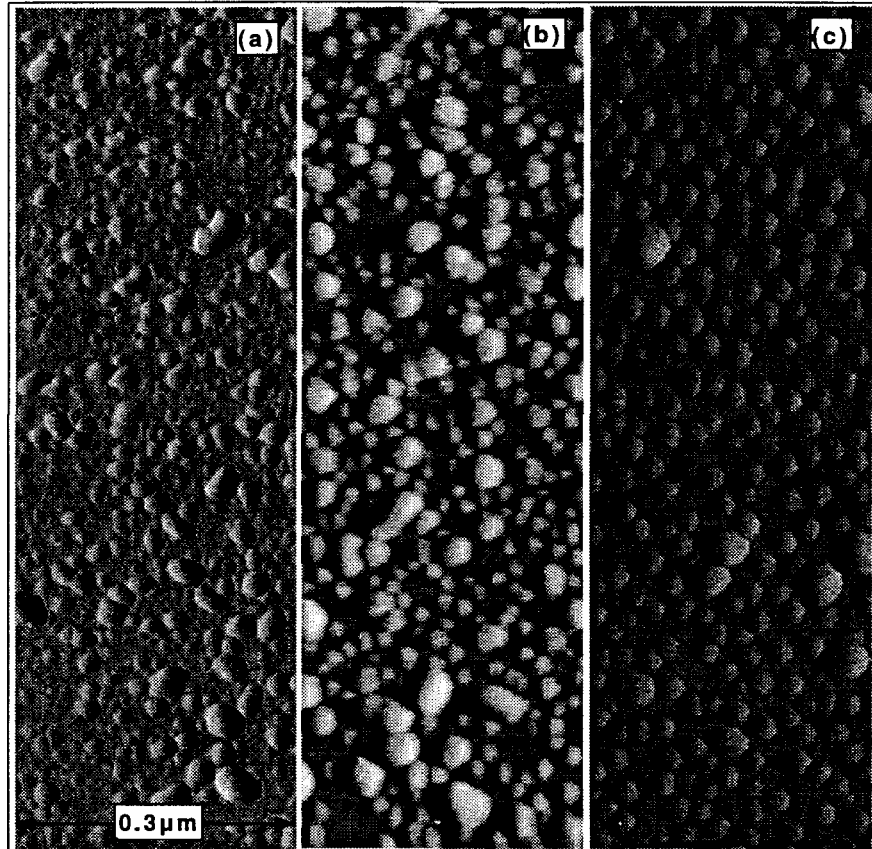


Figure 3.2: The variation in the in-plane InAs island diameter with growth temperature. The growth temperature in (a) is 425°C, in (b) is 500°C and in (c) is 540°C. These temperatures are substrate thermocouple readings.

example illustrated above in Figure 3.1c, where the beginning of the transition from isolated to coalesced islands is observed. In Figure 3.2c the substrate temperature is 540°C (492°C actual) and individual island growth still remains distinct. The average

isolated island size has increased as the substrate growth temperature has increased. At 500°C the average isolated islands size is 180Å (see Figure 3.1b) while in Figure 3.2c at 540°C, the average island diameter has increased to 325Å. While the isolated island growth region is maintained until 3 ML coverage at 500°C (again see Figure 3.1b), but as the substrate temperature is increased to 540°C, the isolated island growth is maintained until at least 4 MLs (Figure 3.2c). Surface kinetics terms are usually exponential, and one that is clearly effecting the island topology is the surface diffusivity. The surface diffusivity suppresses islanding at lower temperatures as is evident in Figure 3.2a, and it appears to effect the island size as well.

The surface island surface topology is further investigated in Figure 3.3 where AFM images show the fine structure of the island distribution. 3 MLs of InAs is deposited in both images, so that the islands are growing in the isolated island regime. The image of the lower temperature sample shows irregularly formed islands that are elongated in the [011], parallel to the nature terrace direction of the crystal. In the image of the sample growth at a higher temperature (500°C), the islands are much more defined and uniform. At the lower growth temperature, lower surface diffusion rates limit In adatoms from diffusing upwards to a different ledge, so the islands can extend laterally along a ledge, but not perpendicular over a ledge. Furthermore, the equilibrium ledge size is smaller and less uniform at low temperature because of reduced GaAs surface diffusion. Therefore, as the growth temperature changes the island size and size distribution changes, as well as the point in deposition process when a phase change from planar to island growth occurs or when a phase change from strained island to relaxed island growth occurs.

As discussed in the last chapter, the substrate type, whether semi-insulating or doped, effects the thermocouple reading of the substrate heater. Therefore, when comparing the results using semi-insulating and doped substrates, the actual temperature is different when the thermocouple reading may be the same. An example is shown in Figure 3.3, where the AFM surface images are of InAs dots deposited on semi-insulating and N⁺ substrates at 500 °C. The larger dots on the N⁺ substrate correspond to a higher substrate temperature. The temperature difference is nearly 60°C. The luminescence features of

these dots is compared in the next chapter and the dots deposited on the doped substrate at 500°C match the spectra of dots deposited at higher temperatures on semi-insulating substrates.

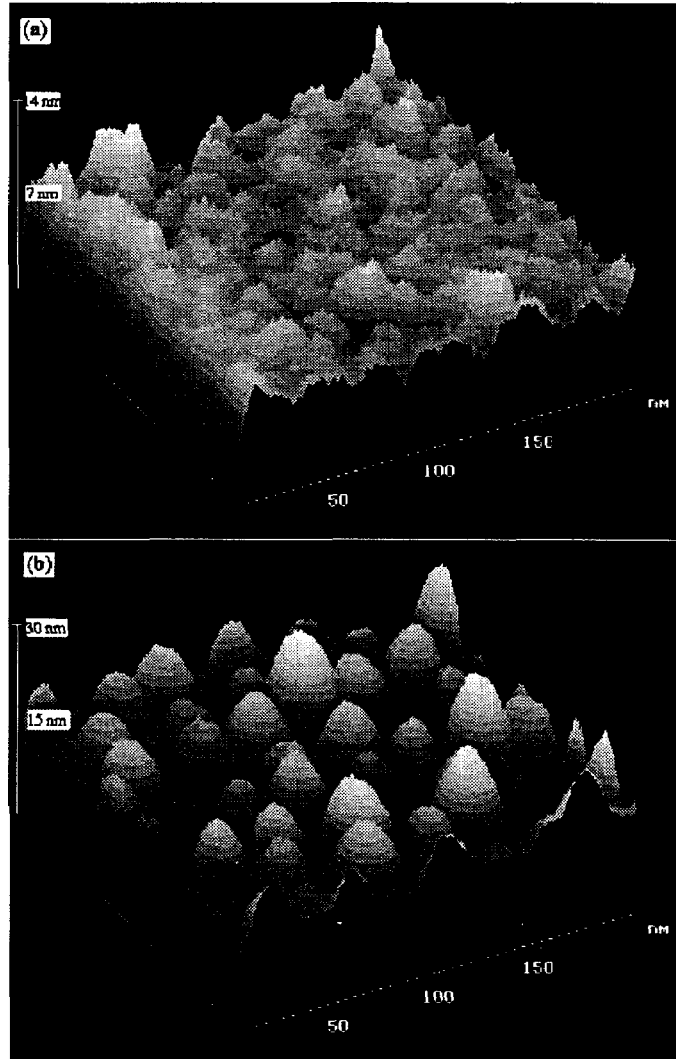


Figure 3.3: Three dimensional AFM images of the InAs islanding surface in the isolated island regime at two different growth temperatures. In (a) the growth temperature is 455°C, while in (b) the growth temperature is 500°C.

3.2 Growth Factors Influencing Island Density

In this section the island density in the isolated island growth regime is investigated. The high density of InAs dots formed by the Stranski-Krastanow growth technique is one of the attributes of this dot formation process. As can be seen from earlier work presented in this chapter, for example Figure 3.1, the natural InAs dot density is much greater than that achieved through conventional lithography techniques. In fact, as lithography techniques are optimized to reach smaller feature sizes, the fill factor will not increase as quickly since the active feature size is often reduced without reducing the spacing between these areas. Therefore, it is important to focus some attention on the effects that alter the InAs island density. If growth parameters can be isolated that control the density, the InAs dot formation process can be tuned to meet different device structure needs. For example, in some optical devices, such as light-emitting diodes (LEDs) or perhaps non-linear optical devices, the InAs density should be as large as possible to maximize the device efficiency. However, in other optical devices, such as lasers individual island uniformity and the ability to contact and control each device independently may require less dense dot ensembles. Conversely, for electronic devices and circuits, a sparsely populated dot surface is likely to be required because of device isolation effects, such as parasitic capacitance, and the more complicated device structures such as individually accessed three terminal devices.

In the previous section the amount of material deposited (the monolayer coverage) at constant temperature, was shown to affect the InAs island density in the well controlled isolated island region [90]. It was indicated that initial surface non-uniformity was responsible for the slow increase in island density with increasing monolayer coverage. In this section, more attention is given to this effect. The island density increases by approximately 40% between 2 and 3 monolayers (MLs) of coverage. In this section the

InAs island density is also shown to be a function of the growth rate and V/III ratio: as the growth rate and V/III ratio are decreased, the island density increases. When the V/III ratio is decreased from 36 to 9, the island density increases by nearly 100%, and when the growth rate is decreased by a factor of 2 the island density increases by 15%. Combining V/III flux ratio, growth rate and monolayer coverage observations, a model is developed in which the V/III flux ratio and growth rate affect the surface diffusion before the fully developed 3-D island growth phase, i.e., in the layer-by-layer and roughening phases. Change in the surface diffusion affects the uniformity of the stress state in the wetting layer by changing the 2-D island size in the wetting layer and the uniformity of the roughened surface as the growth evolves to the 3-D island regime. Islanding is initiated by the accumulated strain in the layer-by-layer region and the islands grow through both strain-enhanced and concentration-dependent surface diffusion until an equilibrium size is reached.

The samples were grown in the usual fashion. The thermocouple substrate temperature was maintained at 500°C. The growth rate, V/III flux ratio and monolayer coverage were adjustable parameters. The V/III flux ratio is the beam flux ratio, that is the ratio of the thermally cracked As₂ molecular beam flux to the In atomic beam flux. This flux is measured by an ion gauge that rotates in the substrate position. In this simple measurement, the mass of the atom or molecule comprising the beam is not considered. All InAs thicknesses are reported in equivalent layer-by-layer ML coverages, while all island diameters reported are measured perpendicular to the growth direction. The island density is calculated as a percentage of the ideal close-packed island density. At the 500°C growth temperature the island diameter is 180Å.

In Figure 3.4, AFM images of InAs islands grown with 2 and 3 MLs of InAs are shown. In both cases the growth rate was 0.19 $\mu\text{m/hr}$ with a V/III flux ratio of 18. Since 3-dimensional islands are present in the 2 ML case shown in Figure 1a, the layer-by-layer wetting region must be locally less than 2 MLs thick. This observation agrees with reflective high energy electron diffraction (RHEED) and optical measurements of quantum wells [91]. Figure 3.4 shows that the average in-plane island size is

approximately 180\AA . The change in island diameter between the 2 and 3 ML case is small compared to the exponential change in island size with substrate temperature as in Figure 3.5. However, the significant difference between the 2 MLs and 3 MLs AFM images is the increased island density with increased coverage. The in-plane island density, referenced to the ideal close packed density, changes from 30% to 49%, a 39% increase. It is observed that as more material is deposited, new islands are formed with only a small increase in the size of older islands. However, as discussed in section 3.1 by 4 MLs at 500°C , the growth enters a new, coalesced island growth regime in which the island diameter grows rapidly with coverage [90].

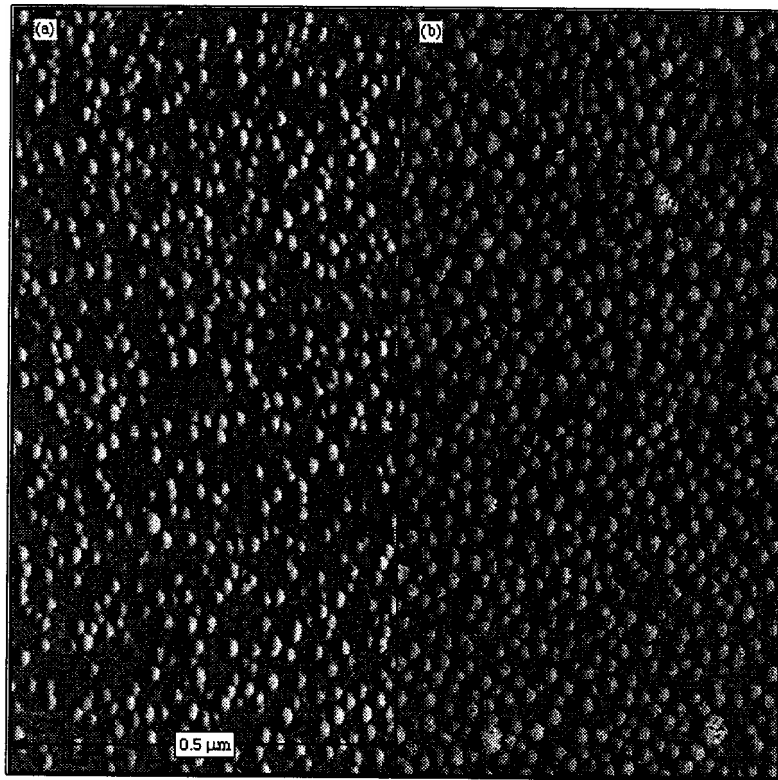


Figure 3.4: Atomic-force microscopy (AFM) images of the difference in island density when the monolayer coverage is changed from 2 MLs in (a) to 3 MLs in (b). In both cases the growth temperature was 500°C and the growth rate was $0.19\ \mu\text{m/hr}$.

In Figure 3.5 the V/III flux ratio is varied in the InAs region while the InAs growth rate is maintained constant at $0.19\ \mu\text{m/hr}$. The V/III ratio is decreased from 36 in Figure 3.5a, to 18 in Figure 3.5b, and finally to 9 in Figure 3.5c. As the V/III ratio is decreased, the 3-D

island density increases, while the island diameter remains unchanged. The island density changes from 42% for a V/III ratio of 36, to 49% for a V/III ratio of 18, to 81% for a V/III ratio of 9. A decrease in V/III ratio increases the In surface migration length. If the island density was modulated by adjusting the In adatom surface diffusion on the

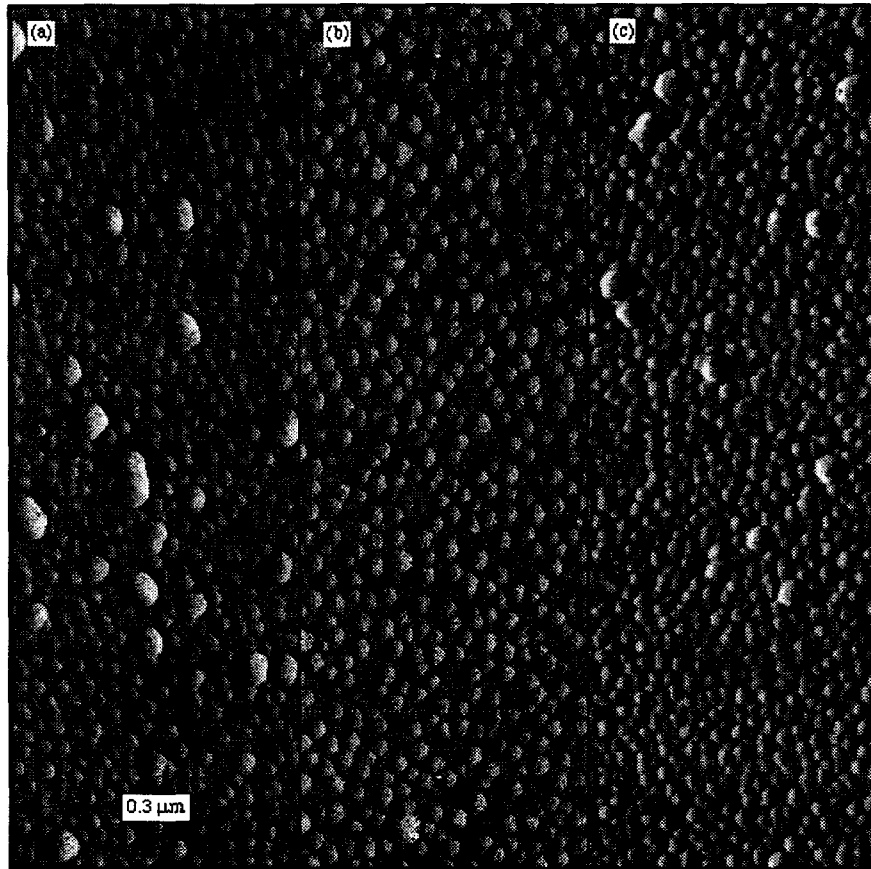


Figure 3.5: Atomic-force microscopy (AFM) images of the difference in island density when the V/III flux ratio is changed from 36 in (a) to 18 in (b) and finally 9 in (c). In all cases the growth temperature was 500°C, the growth rate was 0.19 $\mu\text{m/hr.}$, and 3 MLs of InAs were deposited.

islanding surface, then the island diameter should also change. However, decreasing the V/III ratio can increase the In adatom surface diffusivity in the wetting layer, allowing it to attain a more thermodynamically equilibrium state with respect to uniform strain and uniform roughening. A more uniform strain distribution and roughened growth front will lead to a more uniform island distribution on top of the wetting layer.

In Figure 3.6 the InAs growth rate is adjusted while the V/III ratio is maintained at 18. In Figure 3.6a the growth rate is $0.19 \mu\text{m/hr}$, while in Figure 3.6b the InAs growth rate is decreased to $0.09 \mu\text{m/hr}$. As with previous results discussed above, the in-plane island diameter in both Figure 3.6a and Figure 3.6b is approximately 180\AA . However, as

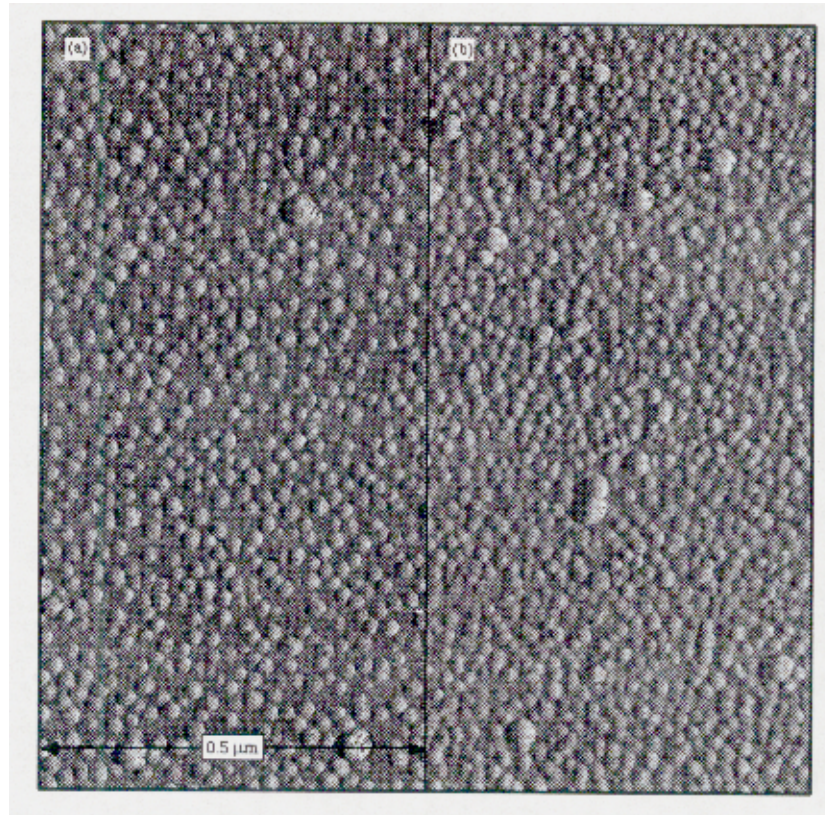


Figure 3.6: Atomic-force microscopy (AFM) images of the difference in island density when the growth rate changed from $0.19 \mu\text{m/hr}$ in (a) to $0.09 \mu\text{m/hr}$ in (b).

the growth rate decreases from $0.19 \mu\text{m/hr}$ to $0.09 \mu\text{m/hr}$, the island density increases from 49% to 57%. Since the island diameter does not change when the growth rate decreases, the growth rate does not change the island density by changing the concentration-dependent surface diffusion in the isolated island growth regime. As with changes in V/III flux ratio, it is believed that decreasing the growth rate increases the surface diffusion in the wetting layer and a more uniform strain distribution and roughened growth front can develop.

An interpretation of the above observations is presented in two steps. First, it is observed that increased ML coverage increases the island density with little change in island diameter. There is a variation in the local strain state on the surface and, hence, islanding does not begin uniformly. As the coverage increases, the strain in some regions on the surface is accommodated through islanding. In other regions, the strain energy continues to increase because the accumulated strain has not reached the point where islanding lowers the free energy. In these areas, layer-by-layer growth continues. As the ML coverage increases, the strain increases in these non-islanded regions until local islanding begins. Second, it is observed that the V/III flux ratio and growth rate do not change the isolated island size, they do affect the island density. If In concentration-dependent surface diffusion in 3-D island region is the limiting effect controlling island density, it should also be the limiting effect controlling island size, and this is not observed. Thus, changes in the surface diffusion (brought on by changing the V/III flux ratio or the growth rate) are responsible for the change in the island density. However, the local strain state in the underlying wetting layer and the evolution of the strain-enhanced roughening in this layer is affected by changes in V/III flux ratio and growth rate. Here strain induced surface roughening is an early stage in islanding. [92] It is important to distinguish between two effects in the wetting layer: the 2-D island size, which is partially controlled by concentration-dependent diffusion, and the periodic roughening, which is controlled by strain-enhanced and concentration-dependent surface diffusion. Decreasing the growth rate and the V/III flux ratio increases the concentration-dependent surface diffusion in the wetting layer and, hence, increases the 2-D island size in the wetting layer. It is important to make clear the distinction between 3-D islands nucleating on top of the wetting layer and 2-D islands that contribute to the layer-by-layer growth of the wetting layer. The 2-D islands nucleate between surface steps and coalesce into a flat layer. In typical MBE growth their density and hence, average size at which they coalesce, is affected by surface diffusion; increasing surface diffusion can lead to larger 2-D islands in the wetting layer. In strained epitaxial systems, the strain where 2-D islands meet will be less than the strain within the islands because of the presence of vacancies at 2-D island boundaries. Thus a layer composed of larger 2-D islands will

have a more uniform strain distribution than one composed of smaller 2-D islands and this leads to an increased 3-D island density. The increased surface diffusion will also allow the growth front to roughen more uniformly, and hence more uniformly develop into 3-D islands of increased density. Although two effects within the wetting layer have been described that will increase the 3-D island density on top of this region, it is not known whether one or both of these effects dominates.

In summary in the SK growth regime of isolated island growth, increasing the monolayer coverage increases the island density with only a small increase in island size. The local strain state is not uniform across the wetting layer surface so that islanding is initiated in some regions while the wetting layer continues to grow in other regions. Therefore, as the equivalent monolayer coverage increases, the island density also increases until the growth regime changes to coalesced island growth. It is shown that by decreasing the V/III flux ratio or decreasing the growth rate, the island density can be increased without changing the average in-plane island diameter. Lower V/III flux ratio and growth rate also increase 2-D island size in the wetting layer and allow the growth front to develop more uniformly, which, in turn, results in the 3-D island density increase.

3.3 Quantum Confinement

Because the bandgap of GaAs is larger than the bandgap of InAs, the transition from a thin planar InAs deposition to an island structure can be considered as a transition from a quantum well like (1-dimensional confinement) structure to a quantum dot (3-dimensional confinement) ensemble structure if the InAs deposition is covered by subsequent GaAs deposition either in the planar growth regime or the islanding regime to form the upper potential barrier. Measurements on these types of samples are found throughout the later chapters. These two types of structures have fundamental differences including the nature of the eigen-energy states, the magnitude and type of scattering and the density of energy states. In this section the fundamental development of quantum confinement is outlined to provide a brief foundation for the optical measurements on

quantum dot structures and devices that are reported in later chapters. Electronic measurements of quantum dot structures are an active research topic and the foundations of this area of study, namely the classical Coulomb blockade, are not developed here. In these electronic structures the quantum dot self capacitance is small, and the addition or subtraction of a charged particle to the dot changes the dot potential through Coulomb interactions with the carriers in the dot (see for example [93]). This section begins with a brief description of the 0D system, where it is shown that the presence of at least one bound state is not required. The density of states is described where the effects of size variation in the dot ensemble are discussed. The section concludes with a discussion on the benefits of quantum dot active regions for increased gain and reduced threshold current densities in semiconductor lasers.

We presume that the presence of quantum dots (QDs) does not significantly effect the crystal periodicity and so the electron and hole wave functions may be written using a Bloch component and an envelope component. The envelope component can be solved using Schrodinger's equation,

$$\left(\frac{P^2}{2m^*} + V \right) \zeta = E \zeta, \quad (3.2)$$

here ζ is the envelope wavefunction and $E = \frac{\hbar^2 K^2}{2m^*}$ assumes the parabolic approximation.

The quantum well (QW) case of confinement in one direction is well known with both odd and even solutions,

$$\begin{aligned} \zeta = \zeta_{n_z}(z) &= A \cos(kz), B \sin(kz), \\ \cos\left(\frac{kL}{2}\right) &= \frac{k}{k_0}, \quad \sin\left(\frac{kL}{2}\right) = \frac{k}{k_0}, \\ \text{where} \quad k_0^2 &= \frac{2m^*V_0}{\hbar^2}. \end{aligned} \quad (3.3)$$

The point to emphasize in this well known solution is that there is always at least one bound state for each m^* because of the even solutions. When the confinement is increased to two directions, an exact solution is only obtained for infinite barriers [94],

$$\zeta = \zeta_{n_x n_y}(x, z) = \frac{1}{2\sqrt{L_x L_z}} \sin\left(\frac{n_x \pi x}{L_x}\right) \sin\left(\frac{n_z \pi z}{L_z}\right), \quad (3.4)$$

and both even and odd solutions are still present. The presence of even and odd states is not affected by the non-infinite barrier potential and hence, at least one bound state will always be present in each of the valance band and the conduction band.

The presence of even and odd states is emphasized because for confinement in three directions, only odd states are present [95]. Solving in spherical coordinates for confinement in the r direction, the exact solution is

$$\sqrt{\frac{2m^* V_0}{\hbar^2} - k^2} = -k \cot(kR), \quad (3.5)$$

and only odd solutions exist. Half of the set of solutions are absent because in spherical coordinates, $r \geq 0$, where as in Cartesian coordinates positive and negative solutions are present. The existence of only odd solutions means that no bound state must necessarily exist in the conduction or valance band. From this result, a critical radius can be defined,

$$R_c = \frac{\pi}{2} \sqrt{\frac{\hbar^2}{2m^* V_0}} \quad (3.6)$$

such that below this radius no bound states will be present in the QD. Because m^* is different for the individual valance band and conduction band states, R_c will also be different for each band.

Thus three different scenarios relating to the existence of bound states are possible: bound electron and hole states, only bound hole states, and no bound states. These regions are calculated for the AlGaAs-GaAs system in Figure 3.7. If the dot size is too

large, the separation of individual states will be less than the thermal energy. For an infinite barrier the separation between the ground and first excited states is

$$\Delta E_{1,0} \approx 10.3 \left(\frac{\hbar^2}{2m^* R^2} \right) \quad (3.7)$$

If this separation is set equal to $3kT_{T=300K}$ an upper bound dot diameter for the situation in which the ground valance states and electron state is bound is approximately 175 Å [95]. The lower bound dot diameter is approximately 60 Å.

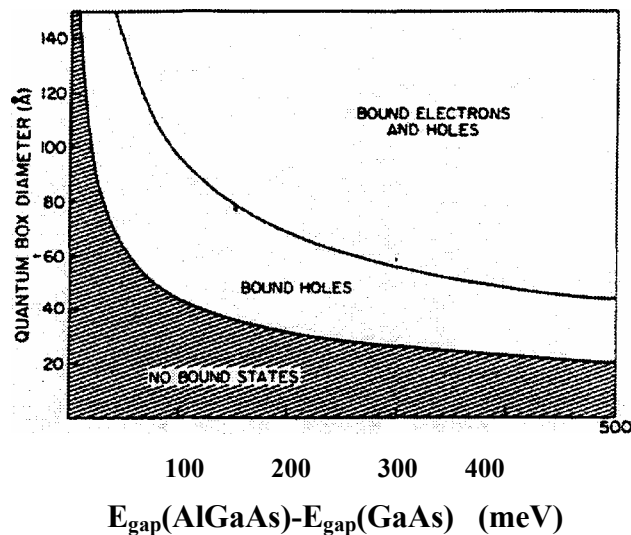


Figure 3.7: The critical dot diameter for the existence of electron and hole bound states in a quantum dot [95].

3.4 Photoluminescence of an Ensemble of Quantum Dots

For optical device structures, the advantages of QD active regions over bulk or less dimensionally confined systems are much more than the spatial localization of electrons and holes. Advantages in threshold current density and optical gain result from the highly discrete density of states found in QD systems. The density of states (DOS) in these

structures is found in many references [87,88] and will only be briefly reviewed. The DOS in bulk material is

$$\rho_k dk = 2 \left(\frac{1}{2\pi} \right)^3 4\pi k dk \quad (3.8)$$

For the quantum wells, quantum wires and quantum boxes the k quantization further increases and the density of states becomes

$$\rho_k dk = \frac{1}{\pi^2} k \left(\frac{\pi}{L_z} \right) dk, \quad \text{quantum well} \quad (3.9)$$

$$\rho_k dk = \frac{1}{\pi^2} \left(\frac{\pi}{L_z} \right) \left(\frac{\pi}{L_x} \right) dk, \quad \text{quantum wire} \quad (3.10)$$

$$\rho_k dk = \frac{1}{\pi^2} \frac{1}{k} \left(\frac{\pi}{L_z} \right) \left(\frac{\pi}{L_x} \right) \left(\frac{\pi}{L_y} \right) dk, \quad \text{quantum dot} \quad (3.11)$$

The densities of states for the four cases are shown in Figure 3.8. The ideal DOS in Figure 3.8 is broadened by some combination of homogeneous and inhomogeneous effects. However, because of the increasingly discrete nature of the DOS as the degree of confinement increases, the QD DOS is more strongly affected by broadening effects. Excitons with a radius of approximately 100\AA are the dominant particles in the InAs/GaAs structures. Because of the roughness of even the InAs quantum wells formed from the InAs planar growth regime, the dominant broadening is inhomogeneous. In the islanding regime, the broadening is more acute because of two effects. First, an exciton in a dot is confined in all directions by a unique potential. Small perturbations in the size of each island effect the excitonic energy, and do so more dramatically than in a quantum well where there is no confining potential in the in-plane directions. Second, the exciton

radius is of the order of the dot radius and therefore the inhomogeneous broadening is

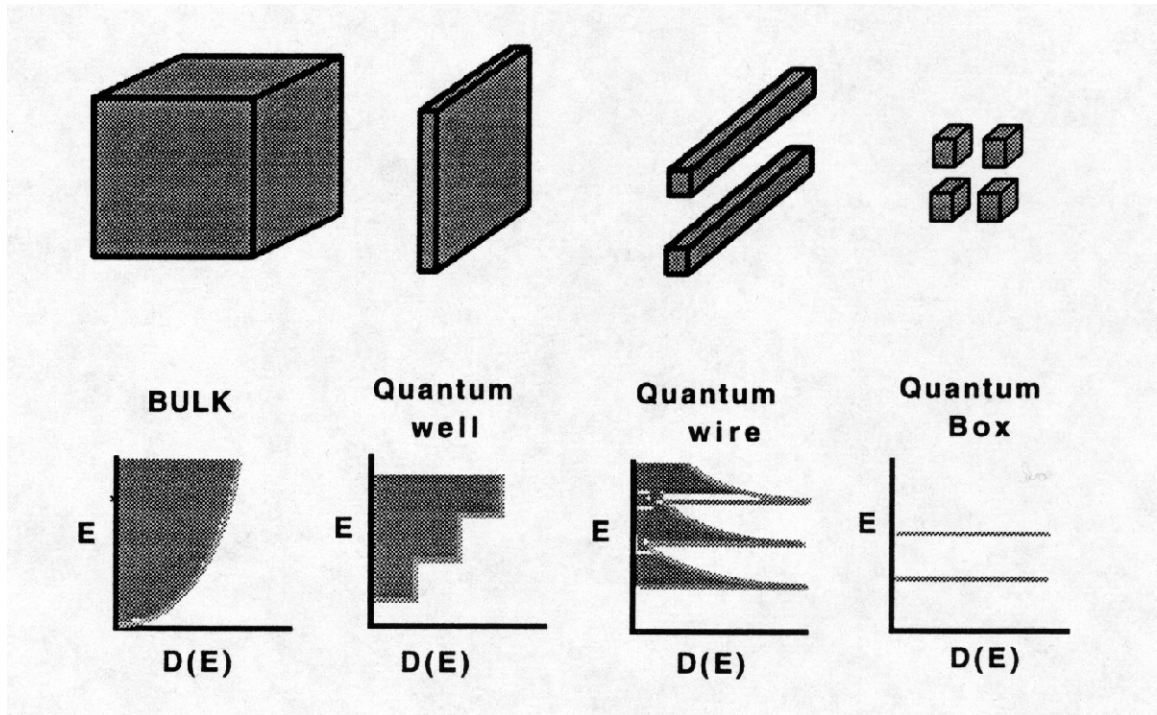


Figure 3.8: The variation in the density of states as the dimensional confinement changes from bulk (no confinement) to a quantum dot (3D confinement).

at a maximum. To see this assume that a quantum well exciton has a Hamiltonian of the form [96],

$$H = H_e + H_h + V_{eh} \quad (3.12)$$

where H_e and H_h , are the Hamiltonians for the individual electrons and holes, while V_{eh} is the Coulomb attractive potential. Now assume that in a quantum dot the individual electrons and holes have a Hamiltonian that is perturbed by roughness potentials $V_{e,d}$ and $V_{h,d}$, respectively,

$$H_e = H_{e,0} + V_{e,d}(z, r_e) \quad \text{and} \quad H_h = H_{h,0} + V_{h,d}(z, r_h) \quad (3.13)$$

where now $H_{e,0}$ and $H_{h,0}$ are the unperturbed QD electron and hole hamiltonians and $V_{e,d}$ and $V_{h,d}$ are the perturbation potentials of the individual dots. The new exciton Hamiltonian is

$$H = H_{e,0} + V_{h,0} + V_{e,h} + V_{e,d} + V_{h,d} \quad \text{or} \quad H = H_0 + V_d \quad (3.14)$$

Assuming the exciton is in the ground state, so that $H_0 |R_{cm}, 1s\rangle = E_{R_{cm}} |R_{cm}, 1s\rangle$ and the variation in the Coulomb potential of the exciton is

$$\Delta V_{exc,d} = \langle R, 1s | V_{e,d}(z) + V_{h,d}(z) | R, 1s \rangle. \quad (3.15)$$

which can be approximated by

$$\Delta V_{exc} = \Delta V_{rough} \left(\frac{\lambda_c}{e_B} \right)^n, \quad (3.16)$$

where ΔV_{rough} is the change in the Coulombic attraction due to local variations in confinement, λ_c is the wavelength of the roughness perturbation, e_B is the exciton Bohr radius, and n is a geometric factor that increases as the confinement goes from 1D to 3D. Thus, the larger product $\Delta V_{rough} \lambda_c$ is the more homogeneous broadening occurs. ΔV_{rough} cannot be of order larger than the excitonic binding or new confinement regions are formed, λ_c 's larger than e_B lead to inhomogeneous broadening, so the maximum broadening occurs when λ_c is of the order of e_B . This is the case in the InAs dots in GaAs where the dot radius is approximately 100Å and equal to the exciton radius.

If a Gaussian size distribution is assumed for the QD ensemble, a density of states that is the convolution of the delta function DOS and the Gaussian variation results [95]. The DOS becomes

$$D(E) = \frac{2\eta}{\gamma\sqrt{2\pi}} \exp\left(-\frac{1}{2}\left(\frac{E}{\gamma}\right)^2\right), \quad (3.17)$$

where η is the number of dots, γ is the rms roughness, and the spin degeneracy is included. In Figure 3.9 the DOS of an ensemble of quantum dots is shown for various values of rms roughness [97].

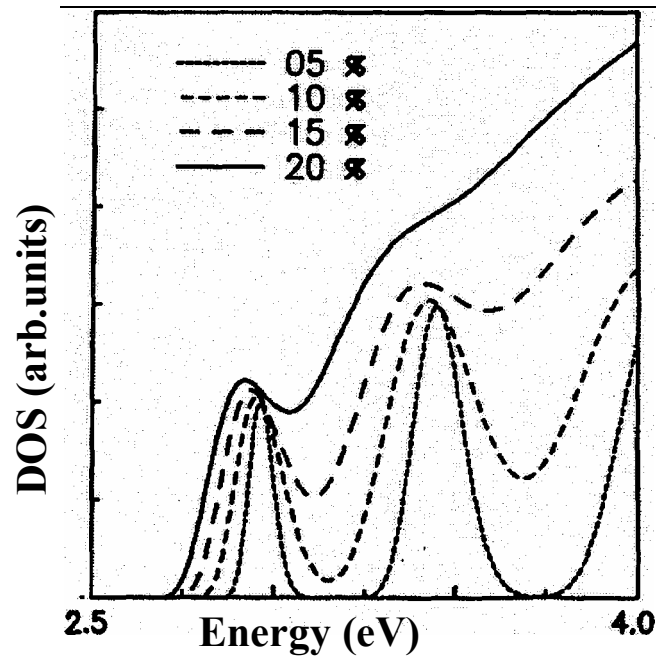


Figure 3.9: The effect of rms surface roughness on the DOS of a quantum dot ensemble. As the roughness increases the DOS approaches the bulk DOS [97].

To achieve transparency, the difference in conduction and valence band quasi-Fermi levels must be approximately equal to the energy gap. k states below the quasi-Fermi levels must be filled and the larger the number of k states below the Fermi level which must be filled the higher the threshold current density. As quantum confinement is increased, the DOS narrows and reduces the number of lower lying states, and hence the threshold current density is reduced. In the case of a single quantum dot, the DOS is a delta function at the lowest lying energy level and the threshold current density is at its theoretical minimum.

Now, only 1 carrier is needed to occupy this level to increase the energy state's occupancy to 1/2 and the difference in quasi-Fermi levels will be larger than the band gap and transparency will occur. For an ensemble of quantum dots, the number of injected carriers must equal the number of dots. The results of a theoretical calculation of the gain as a function of threshold in GaAs/AlGaAs[98] is shown in Figure 3.10a. The threshold current density is reduced by 1/2 when the active region changes from bulk to a quantum well, but the threshold current density is reduced by over an order of magnitude when quantum dots are used in the active region. The optical gain is related to the density of states, $D(E)$, the homogeneous broadening, $g(E)$, and the difference between the quasi-fermi levels, $(f_c - f_v)$ as

$$G(N, \omega) = 2 \int dE d(E - E_0) |M|^2 \left(\int_c \rho(N, E) - \int_v \rho(N, E) \right), \quad (3.18)$$

where $|M|$ is the dipole transformation matrix. As the effective DOS narrows and increases, so does the linear gain, as shown in Figure 3.10b for a theoretical calculation in the GaInAs/InP system [98]. As the dimensional confinement increases, the eigen-energy of each state increases and reduces the lasing wavelength. The gain narrows and the peak gain increases due to the DOS. Although much attention is given to the theoretical reduction in threshold current density with increasing dimensional confinement, the theoretical gain increase is at least as dramatic.

Exciton physics is usually not applicable to lasers because the large carrier densities required for threshold create a large charge carrier background which screens the excitons. However, because of the significant reduction in threshold current density in QDs, gain using excitonic transitions may be possible in these structures [94]. Because the oscillator strength of excitonic transitions increases with increased carrier localization, improvements in oscillator strength similar to those achieved between bulk and quantum wells can be expected. Since dots sizes on the order of the exciton radius must be used, a new lower limit on dot radius must be considered and device dimensions will be larger than those using electron and hole transitions [99, 100].

can relax towards the ground state. This relaxation rate depends on the phonon scattering rate, so for example the relaxation to the ground state is enhanced at higher temperatures where the phonon scattering rate is increased. Thus the energy distribution measured in PL is not the energy spectrum nor does it represent the DOS. In these experiments, it is assumed that the distribution is close to thermal equilibrium and since

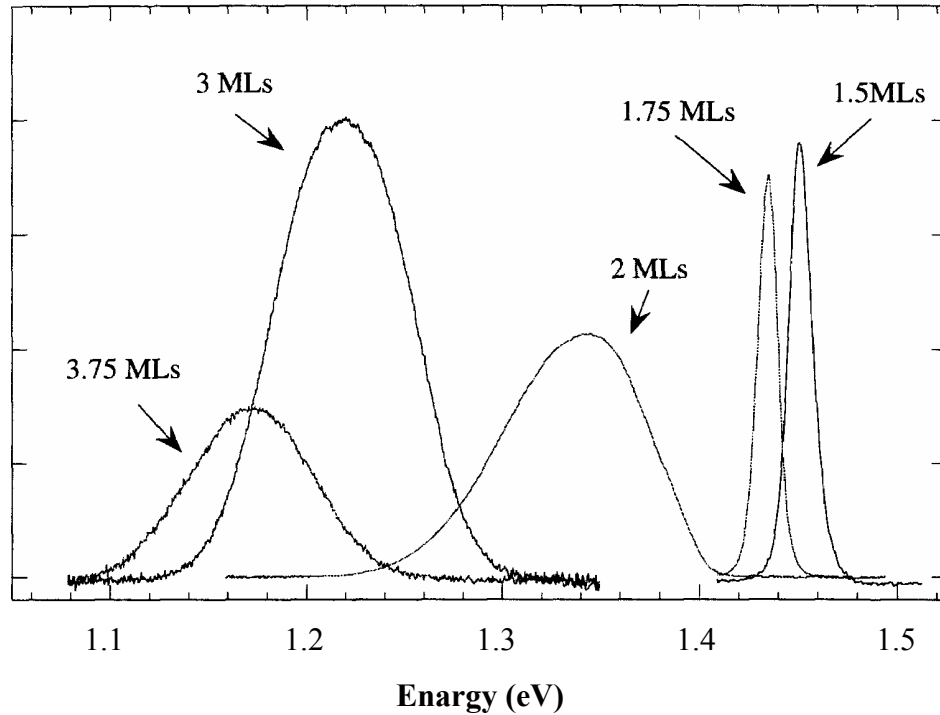


Figure 3.11: 8K PL of several samples which contain InAs thickness that vary between 1.5 MLs and 3.75 MLs. There is a transition from planar growth to dot growth between 1.75 and 2 MLs, while the intensity decrease between 3 and 3.75 MLs is due to non-radiative recombination.

the samples are at liquid He temperatures, it is assumed that the measured spectra represent something close to the ground state energies. A transition in the luminescence signature is observed as more InAs is deposited and is well correlated to a transition in the physical structure between the flat wetting layer surface and the islanding quantum dot surface. As more material is deposited and the structural data indicates the island size and density increases, the luminescence data also shifts to longer wavelengths accordingly. Finally, when enough material is deposited so that island relaxation through

dislocation generation is observed in the structural data, the luminescence intensity decreases, in keeping with the increased non-radiative recombination expected at dislocations. When the structural data of the previous sections and the luminescence data presented here are taken together, the evidence for 0-D confinement in the InAs is very convincing. The luminescence is clearly emitted by the dots and is generally correlated to their changing size. However, the luminescence is greatly inhomogeneously broadened and the sharp 0-D resonances expected in these structures can not be directly observed.

Figure 3.11 shows the photoluminescence of InAs of varying thickness deposited in GaAs. The measurements were taken at 8K using a liquid He cryostat and a lock-in technique. A Ge detector was used for the quantum dot spectra while a Si detector was used for the quantum well spectra. In all cases, the data is normalized to the detector responsivity. The responsivity is obtained by measuring the detector signal as a function of wavelength when spectrally flat white light is incident. In all of the spectra represented in 3.11, the InAs growth rate was 0.11 $\mu\text{m/hr}$, the growth temperature of the InAs layer was 500°C measured by the substrate thermocouple, corresponding to 485°C by the more accurate band edge transmission measurement. The As/In flux ratio was 9 and the As flux is As_2 from an EPI valved cracker. After the oxide is desorbed and the substrate treated at 680°C, the substrate temperature is lowered to 600°C and a 300 nm GaAs buffer layer is grown. The substrate temperature is then lowered to 500°C, allowed to stabilize and after which a 12.5nm GaAs layer is deposited. This cooling process and thin layer growth allow the substrate temperature stabilize after the temperature is dropped and bury any adsorbed impurities. This takes approximately 5 minutes and during this period, the bare substrate surface is left unprotected and exposed to impurities in the vacuum. Additionally, when a metal furnace shutter is opened, the substrate is radiatively heated; opening the Ga shutter first for a short period of time allows the substrate to again come to equilibrium.

With these experimental details described, the results can now be discussed. When 1.5 and 1.75 MLs of InAs are deposited, luminescence features consistent with a quantum well are observed. The structure of these QWs is more thoroughly examined in the last

section of this chapter. As more material is deposited, for example when the total deposited thickness is increased from 1.5MLs to 1.75MLs, the spectral peak position shifts to lower energy since the confinement energy in the quantum well is reduced. This shift is relatively small as only 0.25MLs or 0.75Å are added to the surface. When an additional 0.25 MLs are added so that the total deposited InAs is 2MLs or 6 Å, the spectral peak position and shape change dramatically. This is the transition to the quantum dot ensemble, and correlation of the luminescence structure with the changes in physical structure clearly shows the luminescence originates from the InAs dot regions. The spectral peak shifts to lower energy because the confinement energy is reduced between the QW and QDs. The height is the main factor. In the QD ensembles the average height was determined in previous sections to be about 40Å and is significantly larger than the 5 or 6 Å of the QW. The lateral confinement in the dots does increase the dot confinement energy, but not as much as the increased height decreases it. The linewidth increases because of the distribution in size of the dot ensemble. The luminescence is attributed to an ensemble of InAs dots of different sizes and shapes that each have very narrow spectral linewidth. The integrated intensity also increases when the deposited thickness changes from 2 to 3 MLs. This is due to an increase in InAs dot density, as has also been observed by AFM and described in this chapter. When the amount of deposited InAs is increased from 3 MLs to 3.75 MLs the spectral peak position again shifts to lower energy because of the increasing size of the InAs islands, but the integrated intensity now begins to decrease. It is believed that dislocations are now being generated in the dots which act as non-radiative recombination sites, reducing the luminescence intensity.

3.5 Conclusions

In this chapter, structural and optical properties of strain induced quantum dots were discussed. The first two sections describe different growth regimes, with emphasis on Stranski-Krastanow intermediate growth mode producing defect free coherently strained islands. Theoretical concepts are supported by data collected on InAs/GaAs and

InGaAs/GaAs material systems. Influence of growth factors, such as substrate temperature, growth rate, V/III flux ratio on islanding dynamics, island size and density distribution were characterized and illustrated by AFM images.

When strain induced lower bandgap semiconductor islands grown in Stranski-Krastanov regime are covered with an overlayer of the host semiconductor material with higher bandgap they become quantum dots provided their dimensions are small enough. 3D-quantum confinement formalism was developed in section 3.3 in an attempt to achieve a more profound understanding of applicability of strain induced islands embedded into host material matrix for operation of devices governed by quantum mechanical principles. As a logical continuation, section 3.4 deals with optical characterization of an ensemble of quantum dots grown in Stranski-Krastanow mode. The density of states for carriers in quantum dot ensembles is modified by inhomogeneity of dot dimensions and was also addressed in this section. Photoluminescence results were presented for different InAs coverages and shown to correlate with surface topology evolution observed with AFM. Transition from planar growth regime to Stranski-Krastanow mode of InAs strained layer is clearly associated with photoluminescence peak shift from a QW energy to lower energy QD peak inhomogeneously broadened due to size distribution of InAs islands in GaAs matrix. Further PL peak evolution is in good agreement with island size and density evolution studied with AFM, and finally reflects transition from defect free coherently strained islanding to the regime of dislocation formation when PL intensity drops significantly because of increase in the number of non-radiative recombination channels.

Chapter 4: Lateral Self-Organization of Vertically Stacked Quantum Dots

In the previous chapters the growth parameters governing single InAs dot layers were discussed and structural and optical characterization of these single dot layers was described. In this chapter, the effect of adding additional InAs dot layers in vertical close proximity is investigated. The general method is to deposit an InAs dot layer on GaAs using the growth parameters discussed in Chapter 3, then deposit a thin, sub 100Å GaAs layer, which covers the dot layer and planarizes the growth surface. A new InAs dot layer is then deposited on the GaAs spacer layer, and this cycle can be repeated to produce a structure that is analogous to multi-quantum well or superlattice structures made from thin planar layers. Because of the periodic stress fields, InAs dots from different layers vertically align in columns when the GaAs is thin enough. When the GaAs spacer layer is the correct thickness, the growth surface is planarized with every GaAs layer; thus the surface roughness cycles between the planar GaAs surface and the single layer island roughness found in the initial layer. The surface topology is well controlled through the column formation process and can be completely planarized by subsequent deposition making these self-organized dot columns structurally stable. It is interesting to note that while the single InAs dot layers are a self-organized structure, the dot columns closely follow this initial organization. Because of their vertical orientation and coupling, these self-organized columns may be more desirable basic structural element for optoelectronic and electronic devices. Furthermore, the main drawback of quantum dot structures for device applications - a broad dot size distribution - is somewhat alleviated through QD layer stacking due to lateral ordering and self-organisation effects that are the main focus of this chapter.

This chapter is divided into five sections. The first section describes the process and energetics of island layer stacking and subsequent QD column formation and provides cross-section TEM evidence of dot self-organization into vertical columns. The second section presents a simplified model of layer stacking and based on it, numerical simulation of the islanding evolution characteristics with layer stacking, and its dependency on spacer layer thickness, number of layers and initial island distribution. Section 4.3 delivers experimental confirmation of the lateral self-organization of top layer island positions with layer stacking, while Section 4.4 focuses on original analytical approaches to characterization of the observed ordering. Finally, Section 4.5 is devoted to conclusions based on observed results and comments as to potential usefulness of this self-organization phenomenon for device application.

4.1 Vertical Stacking of InAs Dot Layers

As described in Chapters 2 and 3, in the Stranski-Krastanov (SK) growth mode, the mismatched epitaxy is initially accommodated by biaxial compression in a layer-by-layer growth region, traditionally called the wetting layer. After some critical thickness, the strain energy increases and the development of heteroepitaxial islands becomes more energetically favorable than planar growth. Originally, island edges were presumed to be a nucleation source for dislocations. However, coherent, dislocation-free islands are typically observed [110] and theoretical studies [101, 102], have shown that these islands are initially both partially relaxed and dislocation free. In the III-V semiconductor material system, the SK growth mode has been used to grow InAs and InGaAs islands on GaAs[104, 103, 105] and their size[106, 107], and density[108] are well controlled if the InAs or InGaAs coverage is below an isolated island - coalesced island transition. These islands have also been used as stressors [109] to create 3-D confinement in lower quantum well regions. They can also be used to create As clusters [89]. Growth induced islanding may be a possible alternative to lithographically defined 0-D quantum systems. Current lithography permits length scales on the order of 500Å with low fill factors,

while InAs islands 100 Å in diameter have been grown on GaAs[106, 107] where the island packing fraction is approximately 80% density.[108]

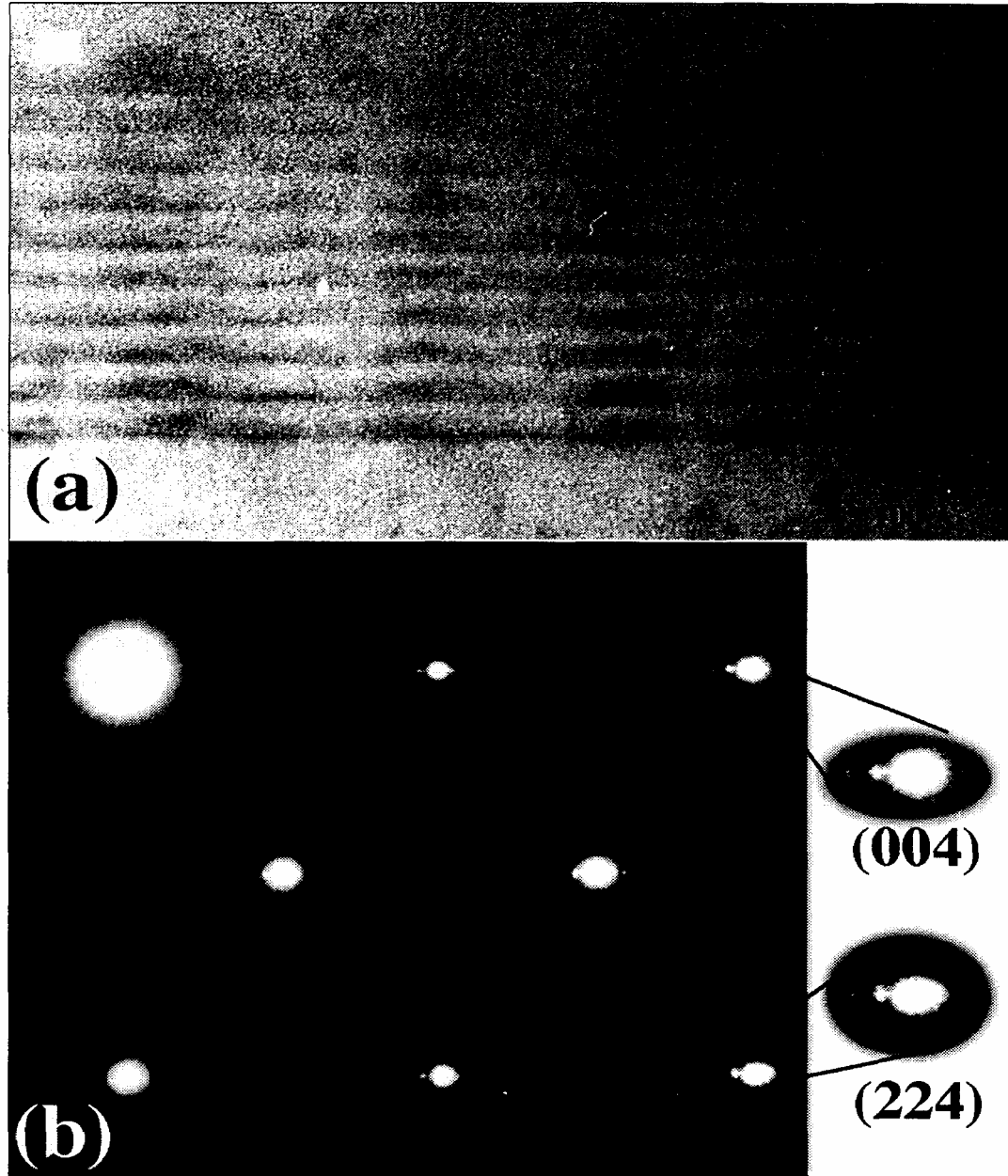


Figure 4.1: (a) TEM (110) cross section image of several columns of vertically aligned InAs islands (dark regions), (b) Selected area diffraction pattern of TEM sample in (a) showing superlattice diffraction spots in the (001) growth direction.

There are additional limitations associated with lithographically defined 3-D quantum dot arrays since lithography is an inherently 2-D process. An alternative to this approach is to layer the strain induced quantum dot layers, and it will be shown in this section that such layering produces vertically aligned dot columns. Previously, the vertical alignment of 2 layers of islands had been observed in the degenerative islanding process in InGaAs quantum wells in GaAs, and was believed to be associated with dislocation generation [111]. In this section, the vertical alignment of up to 10 islanding layers is demonstrated with cross-sectional transmission-electron microscopy (TEM) with no associated dislocation generation.

The epitaxial layers were deposited in using a Varian Gen II molecular-beam epitaxy (MBE) system with As_2 (cracked As_4) as the Arsenic source and a V/III beam equivalent pressure ratio of 9. The InAs island region and all subsequent deposition was conducted at $500^\circ C$, as measured by the substrate thermocouple, and corresponds to $457^\circ C$ using a more accurate optical technique [112]. Each InAs island layer is composed of the equivalent of 3 monolayers (MLs) of planar InAs deposited at a rate of $0.19 \mu m/hr$. The GaAs growth rate was also $0.19 \mu m/hr$. The thickness of the GaAs spacer layer between InAs islanding layers is defined as the thickness between adjacent wetting layers, and not the thickness between islands. For the 50 \AA GaAs spacer layer, the separation between

islands in adjacent islanding layers is approximately 10 \AA . TEM analysis was carried out in a Philips CM20 FEG microscope. A Digital Nanoscope II atomic-force microscope was used to image the surface structure and these measurements were conducted in ambient conditions.

In Figure 4.1, a high resolution TEM image of 10 layers of InAs dots shows several vertically aligned InAs dot columns. The sample is tilted slightly off the zone axis to reduce strain contrast, so that the dark regions in the layered structure are predominately from the increased scattering of the heavier In atoms. The top InAs layer produces much larger, more rounded and diffuse islands, which we believe are more heavily alloyed with

GaAs than the InAs islands in the lower layers. The presence of a new InAs wetting layer close to the peak of the lower islands inhibits mixing of GaAs with the InAs



Figure 4.2: TEM image showing one column of vertically aligned InAs islands. The island height is approximately 40 Å and the in-plane dimension is approximately 180Å.

islands. AFM measurements indicate the islands are approximately 180 Å wide in the in-plane direction, which is confirmed in Figure 4.1a. Although the small spacer thickness impedes vertical alloying with GaAs, the island shape remains consistent with the (113) sides observed by other workers. [113] Several TEM images made perpendicular to the zone axis to enhance the lattice contrast were investigated for dislocations in the layer island regions; none were observed. Dislocations at the upper interface between the InAs islands and the GaAs cap were investigated by tilting the sample up to 30° off the zone axis and again no dislocations were observed.

A selected-area diffraction pattern is shown in Figure 4.1b. Superlattice and InAs diffraction spots are present at all non-inplane reciprocal lattice points. Of particular interest are the bright and faint reflections to the left of the GaAs reflections for non-inplane reflections, for example the (004) reflection. Our calculations indicate the brighter secondary spots are due to the superlattice unit cell and are determined from the average composition and lattice constant of the superlattice. The faint reflections further to the left of the GaAs spot are due to InAs and a higher order superlattice reflection. In reciprocal space directions which are not the growth direction (001) or the in-plane direction (011), for example the (224) direction, the InAs reflections correspond to an in-plane InAs lattice constant that is pseudomorphically strained. Because the InAs islands form aligned columns, there are two separate diffracting regions that are structurally connected: the wetting layer regions without columns and the column regions. High resolution X-ray diffraction (HRXRD) in the [001] direction will be discussed later and confirms that the superlattice diffraction results are from the pseudomorphically strained wetting layer region. Because of the high island density, if the islands were relaxed through a dislocation mechanism, this relaxation should extend to the wetting layer region, and this is not observed.

In Figure 4.2, a high resolution TEM cross section highlights a column of InAs islands clearly indicating the individual InAs islands and their vertical alignment. The 1.7 ML InAs wetting layer[107] is not observed in Figure 4.2. This wetting layer is not only very thin, but also it diffuses vertically and is therefore very difficult to image with the TEM. The island height is approximately 40\AA , but is difficult to accurately determine since at the island peaks, only a small number of InAs atoms remain in cross section to contribute to the contrast, and the observed cross section may not intersect the island centers. The lower island interface is flat and abrupt indicating the GaAs fills in and smoothes the islanding interface. As in Figure 4.1, the island dimensions in the uppermost islanding layer are much larger and from the contrast change, appear to be alloyed with GaAs. To the right of the island column in Figure 4.2 is a 4 or 5 layer column that does not continue

through the upper layers. This decrease in island density after ~ 5 layers is also observed in our AFM results.

The vertical aligning of InAs islands is easily understood within the context of an energy balance between interface free energy terms and the lattice mismatch induced strain energy. The islands form to reduce the large heteroepitaxial free energy component and also allow the InAs to partially relax. Because the InAs is partially relaxed, subsequent GaAs deposition is favored in the non-islanding regions, and thus the valleys between islands should be initially filled. When the islands are covered by GaAs the GaAs on top of the islands is locally more stressed than the GaAs in adjacent regions between the islands. When a new InAs islanding layer is initiated, the locally stressed GaAs regions above the old InAs regions become favorable low energy attachment sites.

The local strain relaxation that occurs by islanding in one layer facilitates preferential island formation directly on top of islands in subsequent layers. The islanding process not only reduces the interface energy by limiting the contact of InAs with the GaAs underlayer, but allows the InAs free surface to partially relax. This partial relaxation is expected to be removed as the InAs island is covered by GaAs. However, if only a thin layer of GaAs is added to the islanding layer, the removal of the partial relaxation will not be complete and the strain field from the buried InAs island will extend to the surface leaving the GaAs locally strained and possibly distorted. In either case, the region above a buried InAs island will act as a preferential nucleation site for further islands. The TEM and AFM observations that there is only a marginally small change in the island size with additional island layering implying that the modification of the local strain state by the buried InAs island is not pronounced enough to measurably change the lattice mismatch.

4.2 Increase in Lateral Island Uniformity with Layer Stacking: Simulation

Using the formalism from Chapters 2 and 3 one can attempt to model the stress field on the islanding surface for stacked QD layers and utilize that trying to predict diffusion of In and Ga adatoms in this field. However, computational complexity associated with this calculation would be immense and still would not guarantee accurate quantitative prediction due to our limited knowledge of all the processes involved. Therefore, we introduce a simplistic 2D model with several empirical parameters. We expect this model to qualitatively approximate evolution of stacked island columns, deduce dependencies of column formation dynamics on the spacer layer thickness, initial island distribution, and adatom diffusion length.

To simulate stress generated by an InAs island covered with a GaAs spacer layer, we will use a model of a sphere with a constant pressure maintained inside and embedded in an infinite medium of a semiconductor crystal. While this approximation is rather crude, since InAs strain induced self-assembled islands are not spherical in shape and the host matrix is not an infinite medium, we believe this model would still be suitable for our qualitative evaluation. The surface strain may be calculated using continuum elasticity theory:

$$\varepsilon(x) = C \left(1 - 3 \frac{S^2}{x^2 + S^2} \right) (x^2 + S^2)^{-3/2} \quad (4.1)$$

where $\varepsilon(x)$ is a surface strain at a lateral position x , S is the GaAs spacer thickness, and C is a coefficient proportional to island size, lattice mismatch, and elastic constants.

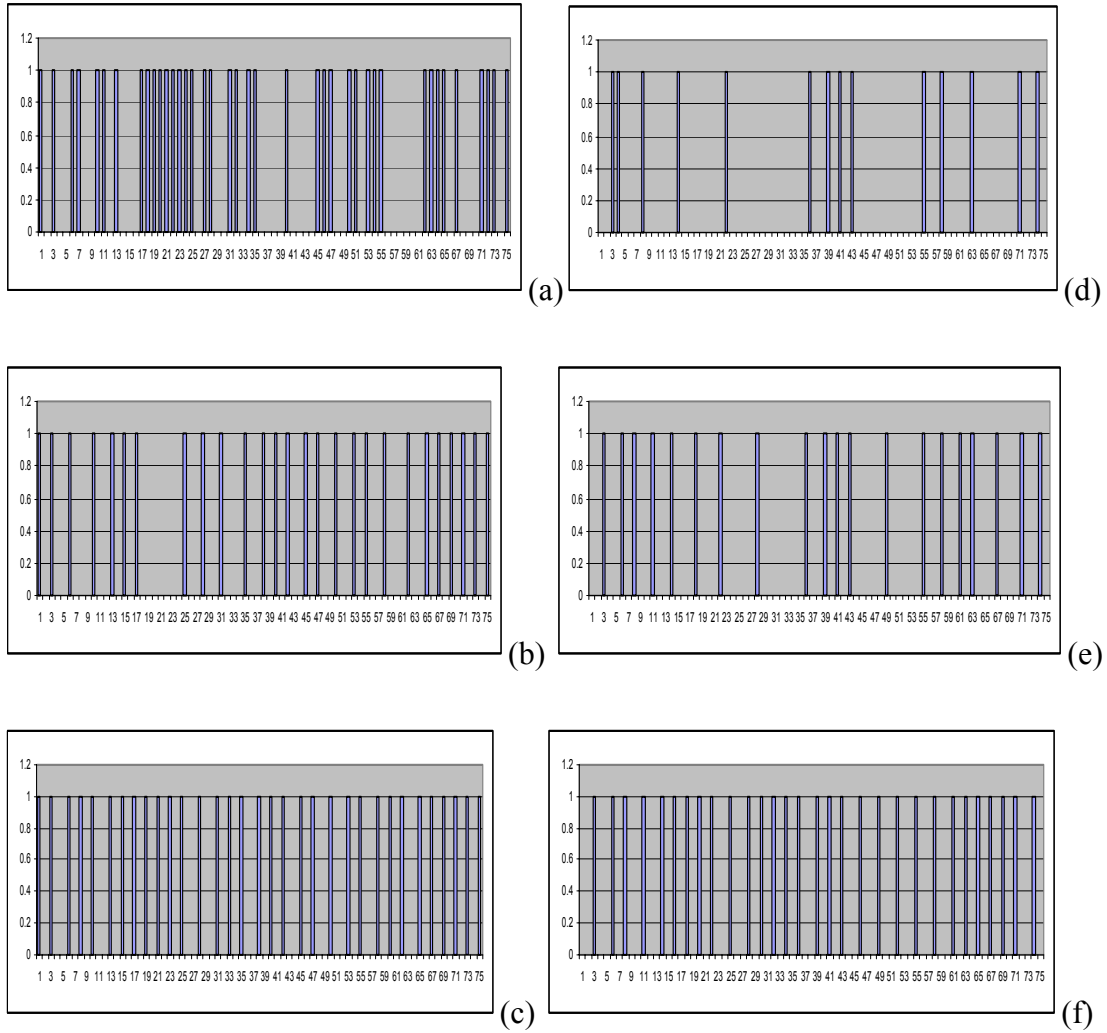


Figure 4.3: Calculated island positions for dense (left) and sparse(right) initial distributions in the first (a,d), second (b,e), and fifth (c,f) layers of a stacked structure.

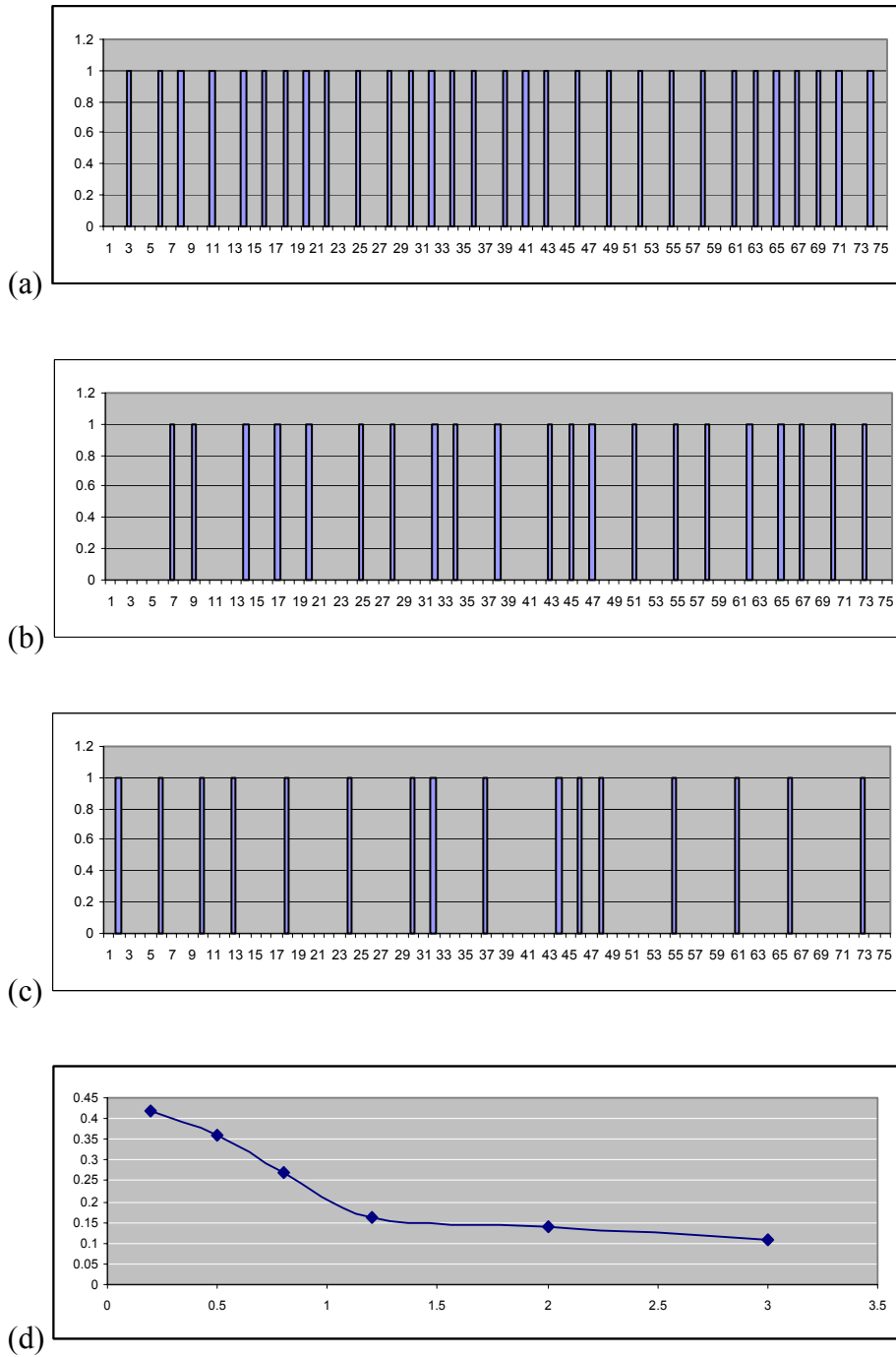


Figure 4.4: Island distribution in the fifth stacked layer with the spacer thickness of 0.5(a), 0.8(b), and 1.2(c) length units. Island density dependency on spacer thickness (d).

The initial island distribution is presumed random as the worst case scenario. Real island shapes are ignored. Island distribution in the subsequent layers is calculated using (4.1) with underlayer islands as stress field sources and adatom nucleation favored in the minima of the created strain potential. The autocorrelation function (4.2) described in detail in Section 4.4 was used to illustrate and quantify ordering. While island layer length was modeled as 512 units, and the whole layer was used to calculate autocorrelation, only limited sections will be shown on the figures to avoid overcrowding.

Figure 4.3 presents evolution of island positions with layering, starting from a dense (a) and sparse (d) random distributions with the same spacer layer thickness. As one can see in both cases after five island layers are stacked, the resulting distribution is considerably less random than the starting island positions. Furthermore, island density appears to be independent of the initial conditions.

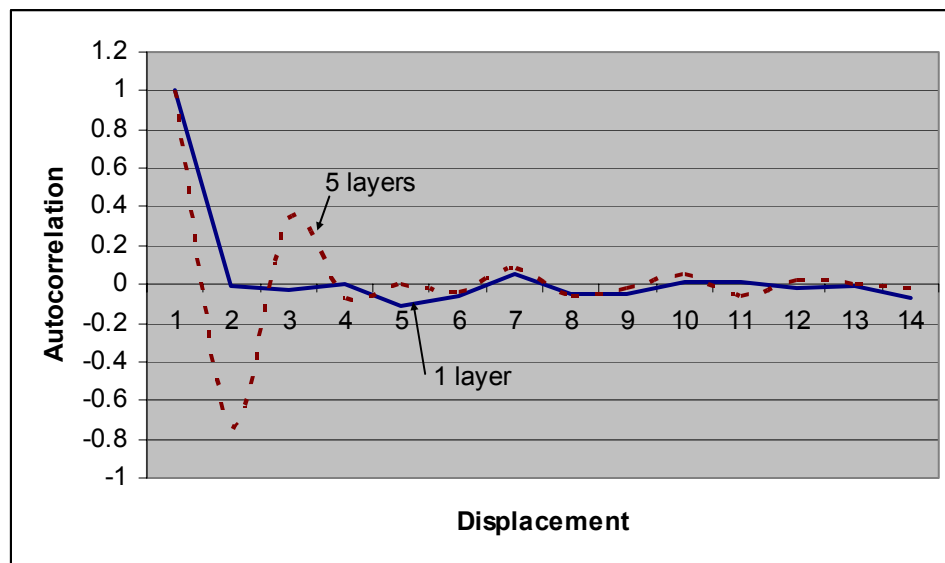


Figure 4.5: Autocorrelation function calculated for the initial island layer (solid curve) and for the fifth stacked layer (dashed curve).

Figure 4.4 illustrates that while self-organized island distribution in the top stacked layers seems to be independent of initial layer conditions, it is influenced significantly by the

GaAs spacer layer thickness. With thicker spacer layer island ordering appears to be less pronounced, which is logical since strain fields induced by the island underlayer are not as strong on the surface of the thicker spacer layer.

Finally, figure 4.5 shows the autocorrelation functions calculated for the initial and fifth island layers, from which one can clearly observe the onset of the island ordering reflected by the second peak in the 5 layer curve. Similar curves were collected on our experimental samples and will be presented in the Section 4.4.

To conclude this section, we have modeled the behavior of island ensembles with subsequent layer stacking using elasticity theory formalism (4.1). The qualitative results of the simulation are quite insightful and predict that island density in the top stacked layers should be independent of the initial layer distribution, while considerably influenced by the spacer layer thickness. The autocorrelation function is shown to be a useful instrument to detect and characterize ordering.

4.3 Experimental Observation of the Onset of Island Ordering

Samples under investigation were grown by molecular beam epitaxy using a Varian Gen II system in Stranski-Krastanow growth mode and consisted of one, five, ten, and twenty layers of coherently strained island layers of InAs with all but the last layer covered with GaAs. The InAs island and GaAs cap layer deposition were conducted at 500 °C with a growth rate of 0.1 $\mu\text{m/hr}$. As_2 from a valved cracker was used and V/III ratio of nine was maintained during the growth. Three monolayers of InAs were deposited to obtain coherently strained self-assembled islands and then a 50Å cap layer of GaAs was grown on top for multilayered structures. The top layer of islands remained uncovered.

Our results are based on atomic force microscope (AFM) scans taken in contact mode in the height regime on a Digital Instruments Multimode AFM. All scans were performed along the (110) crystallographic direction of the GaAs substrates. Figure 4.6 presents two such scans obtained on the samples grown under conditions described above. Figure

4.6(a) shows the top view of a surface with a single layer of coherently strained InAs islands on GaAs, while figure 4.6(b) shows the surface morphology of a sample containing twenty stacked layers of InAs islands, with all layers but the top covered with 5 nm of GaAs. As one can see from the direct visual comparison of the two images, the island density in the top layer of the 20-layered sample is less than that of the single layer of islands. As well, spatial island distribution appears to be more uniform with some evidence of island chain formation along the (100) directions. In other words, in addition to vertical strain induced island stacking, some kind of lateral island ordering occurs.

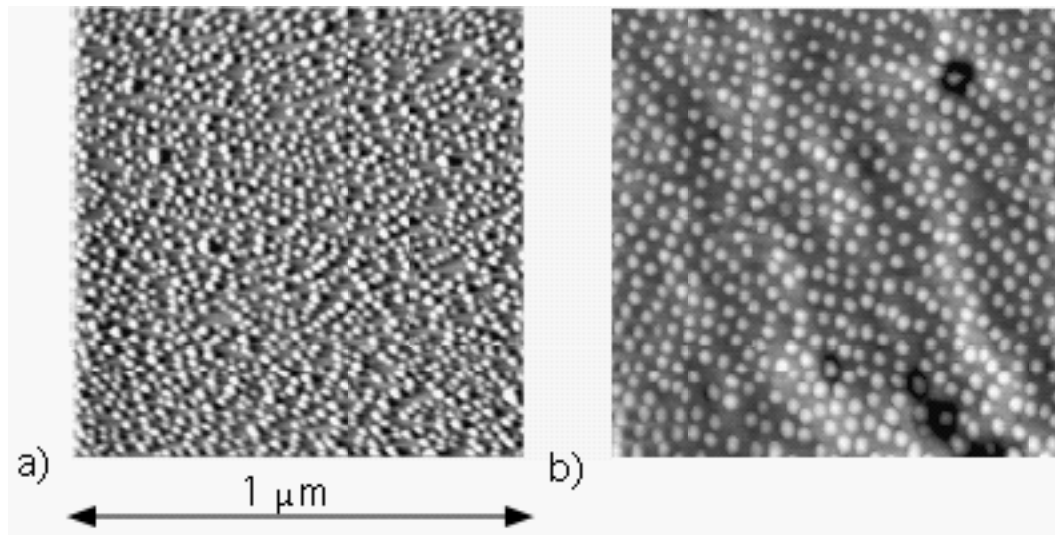


Figure 4.6: Visual comparison of the surface morphology of one (left) and twenty (right) layered samples of InAs self-assembled coherently strained islands on GaAs. Length scale applies to both plots.

It is interesting to see how the stacking of these InAs dot layers changes the size distribution of the dot ensemble. Three-dimensional AFM images of the InAs dot surface are shown in Figures 4.7 and 4.8 as to better convey island height information. In Figure 4.7 the surface topology after a single layer of InAs dots is observed with the AFM. The dots are approximately 40 Å high (in the growth direction) and 200 Å in the in-plane

direction. Figure 4.8 shows the surface topology after 20 layers of InAs dot layers have been deposited.

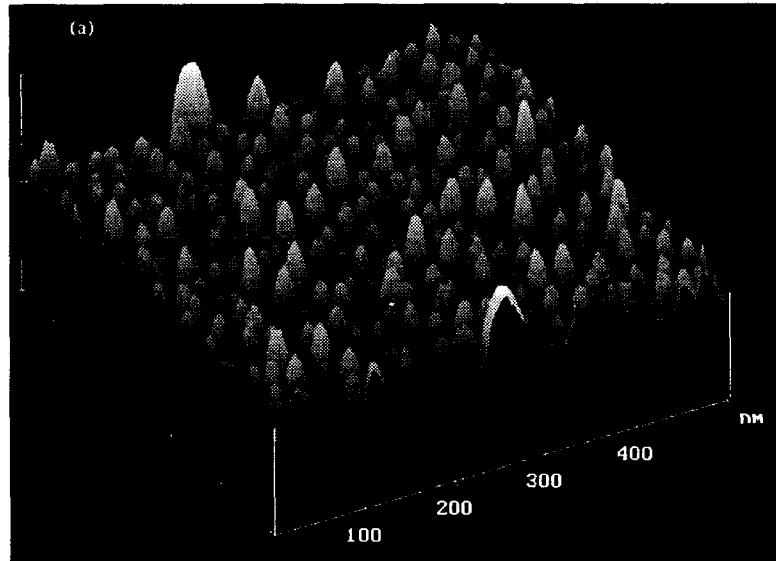


Figure 4.7: 3-D AFM image of the InAs dot surface after 1 dot layer has been deposited.

The dots height and in-plane diameter has increased. The dot density is decreased between the single layer and 20 layer samples from 8.4×10^{10} dots/cm² to 5.7×10^{10} dots/cm². In addition to the decreased island density, two other features are apparent in Figure 4.8 First, in the 20 layer sample the dots are aligned in (100) directions. This alignment is different from the alignment of dots along the (110) directions observed in single dot layer samples, which is due to steps on the growth surface. Second, there is new surface roughness present in the 20 layer sample.

The decrease in dot density with stacking of individual quantum dot layers has been predicted if the initial dot density is higher than some equilibrium value that minimizes the overlapping strain fields of adjacent dots [114]. If the dot density is larger than the strain fields of two adjacent dots overlap and only one dot will form above the dots and spacer layer. In the opposite case, in which the initial dot density is lower than some

equilibrium value, dots will form above lower dots as well as in regions where no dots are found below the spacer region. If an equilibrium state can result, the strain field should be periodic over the growth surface, assisting surface diffusion, and the nearest neighbor distance between nucleating dots will be constant, resulting in uniform nutrient fields for each dot, and thus a more uniform size distribution. Since we have adjusted our

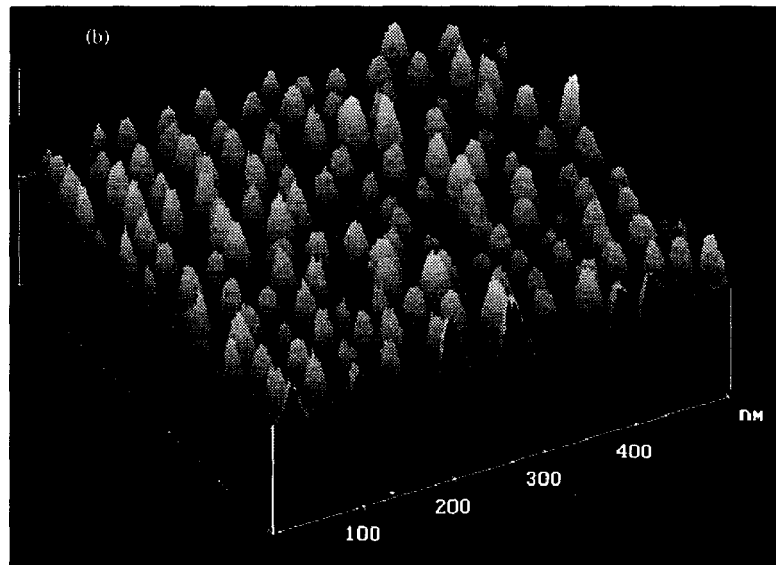


Figure 4.8: 3-D AFM image of the InAs dot surface after 20 dot layers have been deposited.

growth parameters to increase the dot density in single InAs dot layer samples for optoelectronics applications, it is not surprising, in the context of the above discussion, that the dot density should decrease with layering. It is believed that the density of dots in an isolated dot layer is determined by the uniformity of the wetting layer [108]. If the wetting layer was ideally uniform, then the transition from layer-by-layer growth to island growth would occur uniformly over the surface, leading to a dense array of dots with competing nutrient fields. It is believed this is a local minimum which reduces surface diffusion and even though the dots density is large in the single layer late stage ripening, the growth of larger dots at the expense of smaller ones, is inhibited. The

stacking of dot layers overcomes this problem. The more uniformly periodic strain fields which lead to the reduced InAs dot density should also lead to a more uniform dot size distribution.

4.4 Fourier Analysis of The Islanding Statistics

While it can be seen from the surface images that some island self-organization is happening, quantitative characterization of this process is important. In this connection, various image processing techniques become helpful. Figure 4.9 (a, b) shows 2-dimensional Fourier transforms of the AFM scans of the samples with one and twenty layers of InAs islands respectively. Here, the difference between the two samples is much more pronounced. The spectrum of the single-layered sample image is round in shape and does not have any particular features connected with directionality or with particular spatial frequencies. On the other hand, the Fourier spectrum of the AFM scan of the 20-layered sample surface contains rather strong low-frequency components originating from the increased long range (several hundred nanometers) surface roughness accumulated with InAs layer stacking. It also exhibits four clear peaks in the (100) directions, corresponding to a spatial frequency of about 40 nm. These peaks indicate the formation of a partially ordered 2-dimensional lattice of InAs islands in the top layer of the 20-layered structure. Starting from the relatively random island distribution in the single layer, it becomes more and more ordered as the number of stacked InAs island layers increases.

In order to clarify the nature of these peaks, we have performed an inverse Fourier transformation of the spectrum on figure 4.9(b), with low and high frequencies cut off. This results in the image presented on figure 4.9(c). One can see a distorted, but quite recognizable square lattice oriented along the (100) crystallographic directions, with a period of approximately 40 nm.

To further elaborate on the question of the evolution of the InAs island ordering occurring with layer stacking we have calculated the autocovariance of several AFM

images. The samples consisted of one, five, ten, and twenty layers of InAs coherently strained self-assembled islands in a GaAs matrix, with an uncovered top layer. The autocovariance of the function f of two variables is calculated according to the formula:

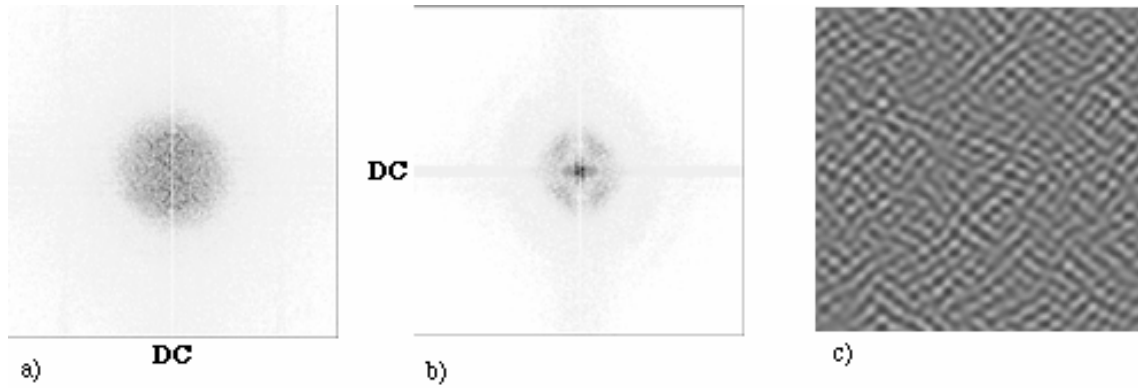


Figure 4.9: Fourier spectra of the AFM images for one (a) and twenty (b) layers of InAs islands and (c) inverse Fourier transform of the “features of interest” in the 20-layered sample’s spectrum.

$$\mathbf{R}_{ff}(\boldsymbol{\mu}, \boldsymbol{\nu}) = \lim_{T \rightarrow \infty} \frac{1}{2T} \int_{-T}^T \int_{-T}^T \mathbf{f}(\mathbf{x}, \mathbf{y}) \mathbf{f}(\mathbf{x} + \boldsymbol{\mu}, \mathbf{y} + \boldsymbol{\nu}) d\mathbf{x} d\mathbf{y} \quad (4.2)$$

Figure 4.10 shows section of the autocovariance in the (100) direction for samples with one (a), five (b), ten (c), and twenty (d) layers of InAs islands. The choice of the (100) direction is stipulated by the previous observations of Fourier spectra with peaks along the (100) directions, as well as by the fact that autocovariance functions of the AFM scans from 10 and 20-layered samples have distinct peaks in these directions. The physical meaning of the autocovariance suggests that the ratio of the amplitude of the second peak in the autocovariance function to the amplitude of the central peak is an appropriate parameter for characterization of short range ordering, while the peaks further from the central peak correspond to longer range order. This was verified by the autocovariance function as well as one-dimensional simulations performed using

Gaussian-shaped islands with randomized positions. As one can clearly see from Figure 4.10, the island distribution is rather random for a single layer, where the second-to-central-peak-ratio, $r = 0.023$. For the sample with five layers, wing peaks start to appear in the autocovariance section with $r = 0.140$, indicating the onset of short range order.

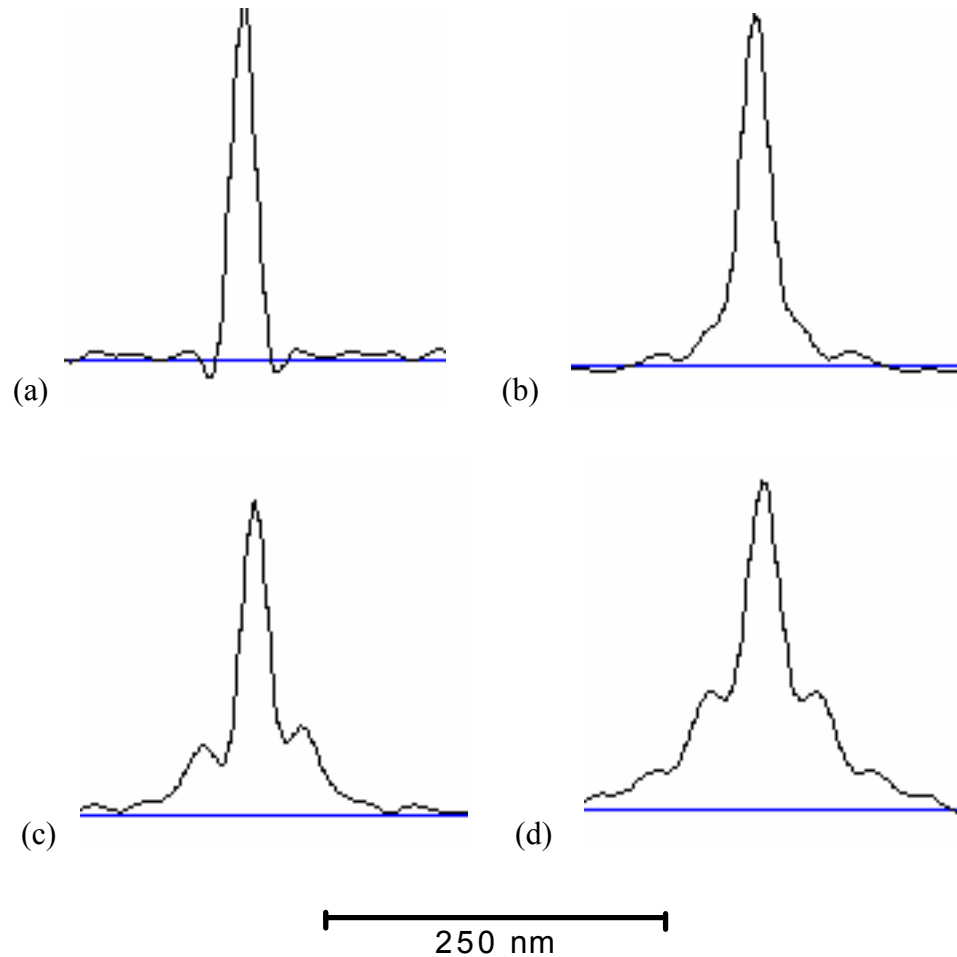


Figure 4.10: AFM image autocovariance (100) sections for one (a), five (b), ten (c) and twenty (d) stacked layers of InAs self-assembled islands. Length scale applies to all plots

For the 10-layered sample, wing peaks in the autocovariance sections are quite pronounced ($r = 0.282$) and weak higher order peaks show up. Finally, for the sample

with twenty layers of InAs islands, short range order is further increased ($r=0.366$), and the onset of the longer range ordering is apparent. The distance between the central and the wing peaks in the autocovariance sections is about 40 nm, and is constant for all four samples. These facts can be interpreted as evidence of lattice formation with a period of about 40 nm that does not depend on the number of layers stacked.

4.5 Conclusions

A vertically aligned quantum dot columnar structures have been investigated in this chapter. It was shown that the vertical alignment is due to the surface stress field which drives In and Ga adatoms in different directions. The structural aspects of the dot columns were first investigated with TEM. Here the dot columns were shown to be defect free and that the wetting layers remain intact throughout the layering.

We have modeled the behavior of island ensembles with subsequent layer stacking using elasticity theory formalism. The qualitative results of the simulation were insightful and predicted that self-organization occurs with island layer stacking; island density in the top stacked layers is independent of the initial layer distribution, but is considerably influenced by the spacer layer thickness. Autocorrelation function was shown to be a useful instrument to detect and characterize island ordering.

The structural ordering of the quantum dot columns was experimentally observed and characterized in this work. Single, 5, 10, and 20 dot layers are investigated each with 50Å of GaAs spacer layers. Atomic-force microscopy was used to investigate the size distribution as various numbers of quantum dot layers are deposited. There was an observed increase in the average height and in-plane diameter of the dots, resulting in a slightly more hemispherical dot after 20 dot layers are deposited. A decrease in the size variation of the dots with increasing number of quantum dot layers was also detected, as well as ordering of dots in (100) directions. Simulated predictions were in good qualitative agreement with experimentally observed distributions with increased layer number.

The reduction in the size variation in height and diameter is the result of several processes. First, the surface stress gradient creates a potential which separates In and Ga adatoms. This potential is present in the initial dot layer, but is not fully established until the initial dot layer is complete. Island pillboxes nucleate randomly on the initial GaAs surface. In the first layer, In adatoms can not effectively migrate from one dot to another because they must diffuse against the stress field. There is a local (not global) minimum at each and every dot, and because of the randomly nucleated initial pillboxes, the nutrient field for the dots is not uniform and thus the dot sizes vary. Once additional dot layers have been deposited, overlapping stress fields create a more uniform periodic stress field. Since the strain field in the dot layers becomes more periodically uniform with each dot layer, dots are nucleated with more uniform nearest neighbor distances and hence more uniform nutrient fields. The more uniform surrounding field leads to more uniform dots size with increasing layer number.

There are several advantages to the vertical column structure over the single dot layer structure. The dot volume density is increased by vertically stacking of the dot layers, regardless of whether the dots align in columns. This is particularly important in quantum dot structures designed for optical applications because the reduced active area is often only a small percentage of the in-plane area. The nearest neighbor distance, i.e., the degree of in-plane order, is also increased as more InAs layers are added. Finally, vertical electronic coupling resulting from a dot column formation, where electronic states are distributed through the vertical column, narrows the optical emission spectrum and provides a lower resistive carrier path due to tunneling of carriers between the dot.

Chapter 5: InAs Strain Induced Islands grown on Ge

In the previous chapters, mostly the growth of strain induced III-V compound semiconductor quantum dots has been discussed. While InAs islands on GaAs constitute a popular material system for research of quantum confinement effects and optoelectronic manifestation of these effects, there are other materials potentially useful in quantum dot fabrication. Group IV semiconductors Si and Ge are rather actively investigated [115,116,117] and some research effort is devoted to II-VI compound semiconductors [118]. Group IV semiconductor strain induced quantum dots are interesting both due to their compatibility with mainstream semiconductor industry and from the fundamental science standpoint since smaller lattice mismatch (4%) between Si and Ge results in the formation of islands that are more suitable for detailed characterization with high resolution atomic force microscopes and scanning tunneling microscopes. The obvious drawbacks are poor optoelectronic characteristics of group IV semiconductors and somewhat larger island dimensions requiring lower temperatures for quantum confinement conditions.

In an effort to possibly combine optoelectronic advantages of III-V compound semiconductors with higher device application potential of group IV elements, we have studied a hybrid material system: InAs islands on Ge. Our investigation was focused on the formation and evolution of InAs strain-induced islands grown by molecular beam epitaxy on Ge and because the lattice constant is nearly equals GaAs as a control of growth under identical conditions. Since the Ge and GaAs have nearly the same lattice

constants we could separate chemical effects and lattice mismatch strain effects controlling the islanding process. Experimental dependencies of the InAs island density and average diameter were obtained and compared for the two surfaces. Variations in size and evolution attributed to the differences in the In adatom surface diffusion. To the best of our knowledge, this was the first time that InAs strain induced islands on Ge were grown and characterized.

This chapter is divided into four sections. The first section touches upon characteristics of self-assembled strain induced islands formed from group IV semiconductors. The second section provides theoretical background for the study of the role of surface diffusion in the islanding process. In the third section, experimental results and comparison of InAs islands on Ge vs. InAs islands on GaAs are presented with focus on the surface diffusion driven differences in the wetting layer thickness, islanding statistics and phase evolution. Finally, the fourth section is devoted to conclusions based on observed results and comments as to role of surface diffusion in strain induced self-assembly.

5.1 Group IV Semiconductor Quantum Dots

In the previous chapters, we have only discussed III-V compound semiconductor material systems where strain-induced islands are formed, mainly InAs in GaAs matrix. Before proceeding to a hybrid system, InAs on Ge, we would like to give a short summary of group IV based self-assembled quantum dot research.

The group IV islands form because of stress from the 4% lattice mismatch between Ge and Si. Similar islands form whether they are grown by chemical vapor deposition [119] at moderate pressures or by molecular beam epitaxy in ultrahigh vacuum [120].

There are two different views of the growth and evolution of Ge islands on Si. One model suggests that the island size distributions are primarily caused by the kinetic process of Ostwald ripening [121]. The most convincing experimental evidence and theoretical

justification for this opinion are the real-time transmission electron microscope studies [122]. It was observed that as additional Ge is added to a Si surface partially covered with Ge islands, many of the smaller islands in the distribution actually shrink and eventually disappear, instead of all of the islands growing. An alternative model by Shchukin *et al.* [123] proposed that, for some systems, there can be a minimum in the free energy of island ensembles that acts to stabilize the distribution at a particular island size. The detailed scanning tunneling microscope measurements of the island size distributions [124] were consistent with Boltzmann distributions, in agreement with the Shchukin model broadened by finite-temperature effects. However, that report also illustrated some of the complexity of the Ge on Si system by showing that two previously identified island shapes: square-based pyramids and multifaceted domes had distinct and non-overlapping size distributions and that the distributions appeared to be in equilibrium with each other.

Ostwald ripening [121] is the coarsening of a particle size distribution driven by the Gibbs-Thomson effect [125]. Ostwald-ripening models [126, 127] incorporate a driving force that depends on the inverse of the radius of curvature of a particle. Atoms detach more readily from smaller particles, which have a higher vapor pressure, and condense more readily on larger particles. Thus, larger particles grow at the expense of smaller particles. The size distribution of the particles broadens with time, and the area density of particles decreases as the smallest particles dissolve. The basic particle radius equation of motion is usually written in the following form:

$$\frac{dr}{dt} = \frac{\beta(T)}{r^m} \left(\frac{1}{r_c} - \frac{1}{r} \right), \quad (5.1)$$

where r_c is the radius of a stable particle that neither grows nor dissolves, m depends on the rate limiting mass transport step. If the mass exchange occurs only through the contact boundary of a 3D island with the surface, then $m=1$ when transport is limited by the attachment and detachment of atoms at the boundary [128], and $m=2$ if transport is diffusion limited [129]. Islands with $r < r_c$ dissolve, and those with $r > r_c$ grow. The

Ostwald-ripening models are usually derived under the assumption that the detachment probability is inversely proportional to the island radius of curvature, an assumption apparently inapplicable to an island with a rectangular or polygonal base, as is the case for Ge on Si(001). Although Ostwald-ripening concepts have been used to explain the observed coarsening of an island distribution during deposition, doing so is valid only when the flux of incoming atoms being added to the adsorbed layer is small compared to the number of atoms diffusing in the adsorbed layer. The deposition rates utilized by many research groups are significantly greater, limiting the use of Ostwald ripening to explain growth processes.

An alternative model based on chemical equilibrium has been proposed [130] to understand the growth and coexistence of islands on a surface, to contrast to the Ostwald-ripening sizes, each with a particular shape, regarded as a distinct chemical species (for example, "pyramids" and "domes"). For the dilute case in which islands do not interact with each other, the ratio of the number of islands with the two shapes is a function of temperature but is independent of the total amount of Ge on the surface. At low coverages, most of the Ge is contained in the smaller pyramids as entropy attempts to maximize the number of islands on the surface. As the coverage increases, the relative amount of material taken up by domes increases more rapidly. However, the volume in the pyramids and the volume in the domes both increase monotonically with increasing coverage. When repulsive interactions are included in the equilibrium model by making the volume ratio a function of coverage, as well as temperature, the amount of material stored in pyramids can decrease with increasing coverage.

5.2 Role of Surface Diffusion in Islanding Dynamics

While it is generally acknowledged that strain is the primary factor for island formation in lattice mismatched semiconductor systems, there are other parameters influencing islanding, and surface diffusion is among those deemed important but difficult to study experimentally. In this section we will lay some theoretical foundations for study of the role of surface diffusion in island self-assembly.

Mean field theory of Stranski-Krastanov heteroepitaxy is most easily understood within the context of a general rate equation theory of epitaxial growth [131]. The central quantities here are the densities of adatoms and islands of various sizes. Kinetic equations are constructed for each on the basis of a phenomenological assessment of the atomistic processes that cause these quantities to change.

Consider first the case of submonolayer homoepitaxy. Growth is initiated by deposition of atoms onto a singular surface at a rate F . The diffusion of adatoms over the surface is characterised by a diffusion constant D parameterised here as $D=(2k_B T/h)a^2 \exp(-E_S/k_B T)$, where k_B is Boltzmann's constant, h is Planck's constant, T is the substrate temperature, a is the lattice constant, and E_S is the hopping barrier. Immobile dimers (the smallest 2D islands) form as a result of collisions between two adatoms. Generically, 2D islands grow by capturing other migrating adatoms and shrink due to the detachment of atoms from their perimeter. The rate at which adatoms attach to an island of size s is $D\sigma_s \langle n_1 \rangle$, where $\langle n_1 \rangle$ is the average adatom density and $a-s$ is the 'capture number' of islands of size s . The detachment rate of adatoms from an island of size s is w_s . Islands can also grow by capturing adatoms directly upon deposition if the adatoms land on the island or near its perimeter. The corresponding rate is Fk_s where k_s is the direct capture cross section. Combining these processes yields the rate equations for the adatom density

$$\frac{d\langle n_1 \rangle}{dt} = F \left(1 - 2k_1 \langle n_1 \rangle - \sum_{s \geq 2} k_s \langle n_s \rangle \right) - 2D\sigma_1 \langle n_1 \rangle^2 - D \sum_{s \geq 2} \sigma_s \langle n_s \rangle \langle n_1 \rangle + 2w_2 \langle n_2 \rangle + \sum_{s \geq 3} w_s \langle n_s \rangle \quad (5.2)$$

where the density of islands of size $s \geq 2$ is given by

$$\frac{d\langle n_s \rangle}{dt} = F(k_{s-1} \langle n_{s-1} \rangle - k_s \langle n_s \rangle) + D(\sigma_{s-1} \langle n_{s-1} \rangle - \sigma_s \langle n_s \rangle) \langle n_1 \rangle - w_s \langle n_s \rangle + w_{s+1} \langle n_{s+1} \rangle \quad (5.3)$$

Solving the full set of equations in (5.2) and (5.3) is a non-trivial numerical problem, particularly where large islands are involved. But if one is not concerned with the island size distribution, a useful alternative approach is to consider a reduced set of equations where we consider only the total density of islands, with averaged kinetic coefficients. The required quantities in this reduced scheme are the total island density

$$n = \sum_{s \geq 2} \langle n_s \rangle \quad (5.4)$$

and the average kinetic coefficients

$$\sigma = \frac{1}{n} \sum_{s \geq 2} \sigma_s \langle n_s \rangle, \quad w = \frac{1}{n} \sum_{s \geq 2} w_s \langle n_s \rangle, \quad k = \frac{1}{n} \sum_{s \geq 2} k_s \langle n_s \rangle \quad (5.5)$$

Rewriting (5.2) and summing over the island size in (5.3) one gets

$$\frac{dn_1}{dt} = F(1 - 2k_1 n_1 - kn) - D(2\sigma_1 n_1 + \sigma n) n_1 + wn \quad (5.6)$$

$$\frac{dn}{dt} = Fk_1 n_1 - D\sigma_1 n_1^2 \quad (5.7)$$

where rate of dimer dissociation is assumed negligible. Weighted summation of (5.3) results in an equation for the average 2D island size

$$\frac{d(ns)}{dt} = F(2k_1n_1 + kn) - D(2\sigma_1n_1 + \sigma n)n_1 - wn \quad (5.8)$$

The classical view of Stranski-Krastanow growth is that the first few monolayers of deposited material grow in a layer-by-layer fashion because they adhere strongly to the substrate. However, as the thickness of the wetting layer increases the effect of the lattice mismatch eventually becomes sufficient to favor islanding and a 3D growth mode. The discovery of coherent islands demonstrated this transition does not require the introduction of misfit dislocations. To incorporate the physics of coherent Stranski-Krastanow growth into the rate equation formalism two island populations are required: 2D islands of density n_s and 3D islands of density m_s . Each island type has its own set of capture numbers, direct capture cross-sections and detachment rates. We allow a 2D island of size s to spontaneously convert into a 3D island of size s at a rate $1/\tau_s$. More precisely, this occurs for all islands when the energy of the 3D island is less than the energy of the 2D island, i.e. those when $s > s^* \sim (\gamma/\mu\epsilon a)^3$, where γ is the mean island surface energy, μ is the shear modulus, and ϵ is the island strain. The reverse process, where a 3D island transforms to a 2D island is assumed to be negligible. By including the 2D and 3D island populations in our basic set of rate equations (5.2) and (5.3), we obtain as an approximation the expanded set of reduced rate equations for the average 2D and 3D island densities, n and m , during Stranski-Krastanow growth

$$\frac{dn_1}{dt} = F(1 - 2k_1n_1 - kn - k_{3D}m) - D(2\sigma_1n_1 + \sigma n + \sigma_{3D}m)n_1 + wn + w_Dm \quad (5.9)$$

$$\frac{dn}{dt} = Fk_1n_1 - D\sigma_1n_1^2 - n/\tau \quad (5.10)$$

$$\frac{dm}{dt} = n/\tau \quad (5.11)$$

In addition, for the average 2D and 3D island sizes we have

$$\frac{d(ns)}{dt} = F(2k_1n_1 + kn) - D(2\sigma_1n_1 + \sigma n)n_1 - wn - \frac{sn}{\tau} \quad (5.12)$$

$$\frac{d(ms_{3D})}{dt} = Fk_{3D}m - D\sigma_{3D}mn_1 - w_{3D}m + \frac{sn}{\tau} \quad (5.13)$$

and for the diffusion length

$$\lambda = (2\sigma_1n_1 + \sigma n + \sigma_{3D}m + k_1 F/D)^{-\frac{1}{2}} \quad (5.14)$$

The detachment rate is derived from the number of detachment sites being proportional to the island radius, thus

$$w_s = 2\pi \left(\frac{r_s D}{a^3} \right) \exp\left(\frac{-E_d}{k_B T} \right) \quad (5.15)$$

while 3D nucleation rate for islands small compared to the diffusion length is given by

$$\frac{1}{\tau_s} = \pi \left(\frac{r_s^2 D}{a^4} \right) \exp\left(\frac{-2E_d}{k_B T} \right) \quad (5.16)$$

We will now proceed to experimental results of InAs island growth on Ge in comparison to InAs islands on GaAs and utilize formalism developed in this section to explain our observations.

5.3 Comparison of InAs Islands on Ge and on GaAs

This section is devoted to the experimental study of the unconventional material system: strain-induced InAs islands on Ge and its comparison to the control, InAs island growth on GaAs. We believe this is the first time that nanoscale islanding in Stransky-Krastanow mode has been observed and characterized in this material system. The lattice mismatch

between InAs and Ge is 7% and differs from InAs and GaAs by only 0.08%, allowing us to compare islanding dynamics in two systems with similar strain conditions, but different underlayer material. In addition, understanding the InAs island evolution in this system may give more insight into other systems, particularly III-V islands on Si.

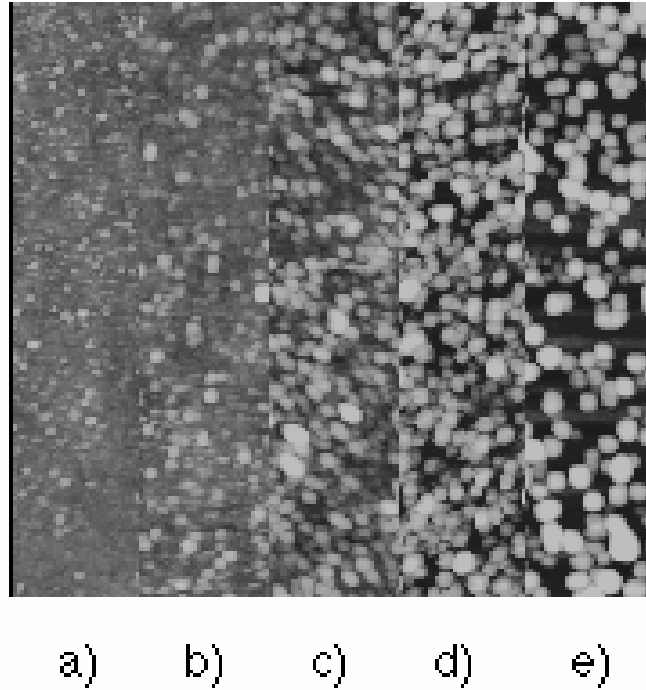


Figure 5.1: AFM images of InAs island on Ge with monolayer coverages: a) 1.5 ML, b) 2 ML, c) 2.5 ML, d) 3 ML, and e) 3.5 ML.

InAs islands were grown by molecular beam epitaxy with a substrate temperature of 420°C, an InAs growth rate of 0.15 $\mu\text{m/hr.}$, and a V/III flux ratio of 12 using cracked As_4 . In order to avoid Ge desorption our growth temperature is lower than conventionally used for InAs growth on GaAs. The growth temperature is set at the optimum temperature for InAs island growth on Ge, and InAs islands are grown on GaAs for comparison. The InAs was deposited on a 10 nm thick Ge layer grown on a 100 nm thick GaAs buffer and (100) GaAs substrate. Since the lattice constants of GaAs and Ge only differ by 0.08%, the 10 nm thick layer of Ge deposited on GaAs adequately represents bulk Ge properties.

For comparison, samples were made with InAs deposited directly on GaAs under the same conditions. The surface morphology was examined ex-situ with an atomic-force microscope (AFM), where tip convolution effects and native oxide formed have no effect on the island density data, but slightly exaggerate InAs island dimensions.

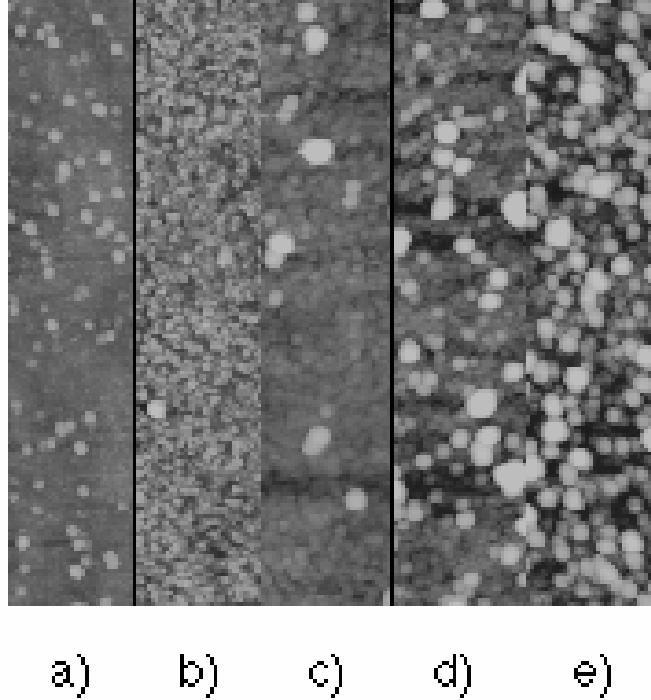


Figure 5.2: AFM scans of InAs island on GaAs with monolayer coverages: a) 1.5 ML, b) 2 ML, c) 2.5 ML, d) 3 ML, and e) 3.5 ML.

We have observed that the formation and evolution of InAs islands on Ge differs from islanding of InAs on GaAs. Taking into account that the lattice mismatch is the same, we attribute the differences in wetting layer thickness and islanding evolution between these two systems to differences in the surface diffusion and attachment dynamics of the In adatoms. Island density and average diameter statistics suggests that the surface diffusion plays an important role in island formation, and that the In adatom surface diffusion length is larger on Ge than on GaAs. It will be shown that these results are in good

qualitative agreement with the rate equation formalism of Section 5.2. The growth temperature is low enough so that In adatom desorption effects are not observed.

The relatively low and identical deposition rate w for both material systems ensures that in our growth regime, the island density is linearly proportional to w/D , where D is the diffusion constant. Thus, growth is below supersaturation and the strain-driven 2D-3D transition initiated by the island nucleation is primarily influenced by the surface diffusivity. This is confirmed further by our experimental results discussed below. Figure 5.1 shows a sequence of five AFM images of InAs islands on Ge, while in Figure 5.2 a similar sequence is shown for InAs islands on GaAs. In both figures the range of coverage is from 1.5 to 3.5 monolayers (ML) of InAs. At 1.5 ML of InAs coverage, the InAs islands on Ge are initially smaller (Fig. 5.1(a)), as compared to InAs islands on GaAs (Fig. 5.2(a)). InAs islands on Ge exhibit gradual density and diameter increase with relatively unimodal distribution in the range from 2 to 3 MLs of coverage (Fig. 5.1 (b)-(d)). However, for 2 ML of coverage of InAs on GaAs (Fig. 5.2(b)) the situation is dramatically different. The InAs islands form into a densely packed (with density above $2 \times 10^{11} \text{ cm}^{-2}$) ensemble of small (average diameter around 13 nm) relatively uniform size islands. This is indicative of lower surface diffusion length impeding In adatom movement to an existing 3D island. At 2.5 MLs of InAs on GaAs (Fig.2 (c)) a new phase of larger islands occurs within the existing closely packed ensemble of small and more uniformly shaped islands. With further InAs deposition up to 3 ML of InAs on GaAs (Fig.2 (d)) the density of these large islands increases, while the small islands remain relatively unchanged. And, finally, at 3.5 ML of coverage both phases of islands still coexist, though the number of smaller islands decreases, the density of the large islands becomes comparable with that of the small ones, and the total island density is reduced. This bimodal behavior is also well explained by the surface diffusion limited regime of growth, which does not allow smaller islands to dissolve feeding adatoms to the energetically preferential larger ones. InAs islands on Ge at 3.5 ML of coverage begin to coalesce, reducing their density and increases their average size considerably.

Statistical analysis of the AFM images shown in Figures 5.1 and 5.2 provided information about experimental dependencies of the island density and of the average island size on monolayer coverage for the two material systems at hand.

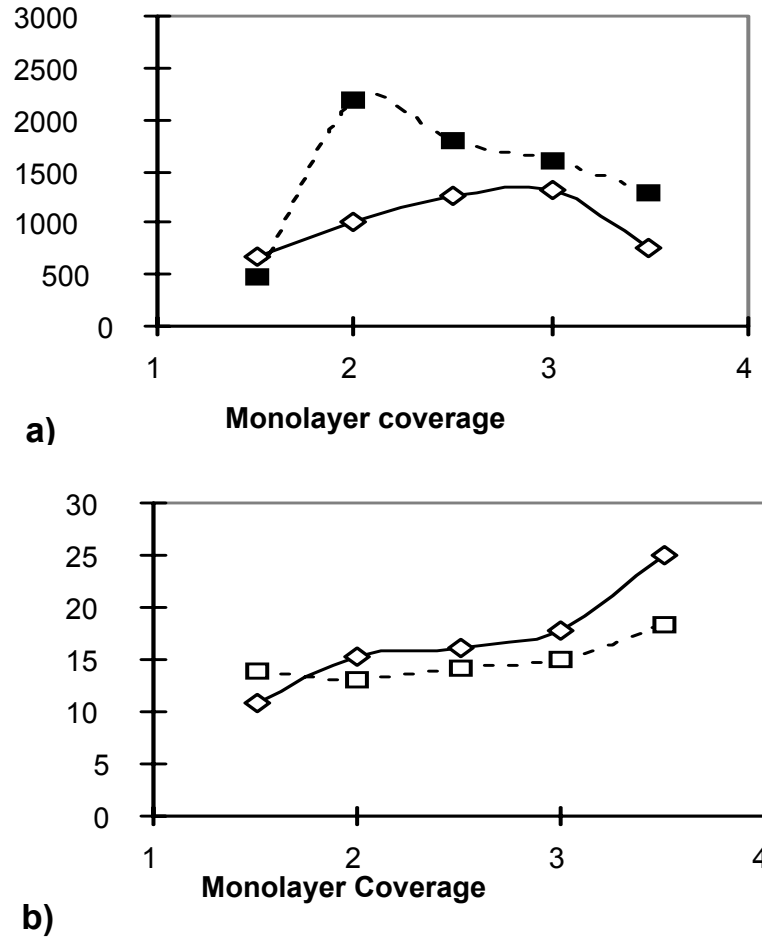


Figure 5.3: Monolayer coverage dependencies of the island density (a) and average diameter (b) for InAs islands on Ge (solid line) and on GaAs (dashed line).

In Figure 5.3 (a) we compare the evolution of the island density in the InAs/Ge system (solid line) and in the InAs/GaAs system (dashed line). The InAs wetting layer thickness deduced from these curves is 1.2 ML on Ge and 1.5 ML directly on GaAs. The island density increases rapidly with ML coverage in InAs on GaAs system reaching saturation density of $2.2 \times 10^{11} \text{ cm}^{-2}$ at 2 MLs of InAs deposited, while with InAs islands on Ge the density grows slower, saturating at higher amount of material deposited (2.5 ML) around $1.3 \times 10^{11} \text{ cm}^{-2}$. This behavior is well understood if we take into account that the larger surface diffusion length of an In adatom on Ge will facilitate the attachment of In adatoms to an existing InAs island, while In adatom motion on the GaAs surface is more restricted, leading to a thicker wetting layer and higher island density.

The average island diameter as a function of InAs deposition is compared for the Ge and GaAs surfaces in Figure 5.3 (b). The results generally show the trends expected from the surface diffusion influence described above. The InAs islands on Ge grow with monolayer coverage starting from relatively small islands of 10 nm in diameter at 1.5 ML, reaching average size of 25 nm at 3.5 ML. For the coverages from 2 to 3.5 monolayers, the InAs islands on GaAs are smaller with diameter ranging from 12 nm to 18 nm. We believe the smaller average islands size of the islands on the GaAs surface is a direct result of the smaller diffusion length of In adatoms on this surface. There is a difference in the form of the transition from the planar wetting layer to the islanding regime on the two surfaces that we are further investigating. This can be seen in the cross-over in the average islands size between 1.5 and 2 MLs, as well as the slight increase in average InAs island size on the GaAs surface, which has been confirmed through repeated experiments.

Following formalism developed in section 5.2 and taking into account values of adatom binding energy for In on Ge $E_B=0.33 \text{ eV}$ [140] and for In on GaAs $E_B=1 \text{ eV}$ [141] one can deduce that adatom diffusion length $\lambda \sim \exp(-E_B/k_B T)$ is indeed greater for InAs deposited on Ge than on GaAs, which perfectly correlates with our experimental observations of islanding statistics and evolution described above.

5.4 Conclusions

To summarize, we believe that this is the first observation and characterization of self-assembled InAs islands on Ge. The comparison of islanding dynamics in this system with that of InAs islands on GaAs substantiates the importance of other factors besides the epitaxial strain state, since the lattice constants of Ge and GaAs are nearly identical. We associate differences in island formation and evolution to variations in the surface diffusion length of In adatom on Ge and GaAs surface. These conclusions are in accordance with independent measurements of corresponding binding energies.

Chapter 6: Quantum Dot Device Applications

For more than 30 years, the microelectronics industry has enjoyed dramatic improvements in the speed and size of electronic devices. This trend has long obeyed Moore's law, which predicts that the number of devices integrated on a chip would double every 18 months. Adherence to this exponential growth curve has been a monumental task requiring rapid improvements in all aspects of integrated circuit fabrication, to permit manufacturers to both shrink the size of devices and increase chip size while maintaining acceptable yields. Since the early 1970s, the device of choice for high levels of integration has been the metal oxide semiconductor field effect transistor (MOSFET), and while the MOSFETs of today are a vast improvement over those of 1970, they are still used as current switches. However, at gate lengths below $0.1\mu\text{m}$ MOSFETs begin to encounter fundamental effects that make further scaling difficult. A possible way for the microelectronics industry to maintain growth in device density is to change from the MOSFET-based paradigm to one based on nanostructures. Here, instead of fighting the effects that come with feature size reduction, these effects are used to advantage.

Section 6.1 will focus on optoelectronic device applications of strain induced semiconductor quantum dots, while electronic devices based on single electron transfer in and out of the quantum dots will be discussed in the Section 6.2. Proper conclusions will be drawn in Section 6.3

6.1 Optoelectronic Quantum Dot Devices

It is naturally desirable to extend the device performance successes gained using quantum wells in optoelectronic devices, to structures with further dimensional reductions in the density of states (DOS), such as quantum wires and quantum dots. The implementation of such structures should result in increasingly efficient light-emitting diodes (LED), lower threshold lasers and novel nonlinear optical devices if the QD size is reduced to allow room temperature applications, the QD size uniformity is improved to take advantage of the sharp resonances in the QD DOS, and reliable and simple fabrication techniques are developed. A simple approach is self-organized islanding, induced through lattice mismatched crystal growth, which has been described in the previous chapters and has produced InAs islands on GaAs with in-plane diameters of less than 20 nm that exhibit 0-dimensional quantum confinement effects. These structures are small enough for room temperature applications; however, the variation in the dot size leads to large inhomogeneous broadening and a loss of the sharp luminescence from the 0-D energy states. Researchers hope this simple QD fabrication method will provide an alternative to the intensive post-growth processing and magnetic field techniques which are currently used to fabricate QD structures. The wetting layer acts as a narrow InAs quantum well (QW) and is connected to the random array of InAs quantum dots (QDs), so the system can be a mixture of 3-D and 1-D confinement. It is believed that a major advantage of the self-assembled QDs is the high dot densities that can be produced in these self-organized random arrays. These densities can approach 80% of the ideal close-packed array density, and will be important for optoelectronic device applications.

The vertical columns of quantum dots discussed in Chapter 4 can be used to increase the optically active volume of LEDs as well as to improve QD size uniformity. The vertically stacked InAs island layers use a sub 10 nm GaAs spacer region between adjacent InAs island layers. QDs from different layers are found to be vertically aligned in columns and are electronically coupled. Luminescence from wetting layer quantum well regions is

nearly eliminated in the multi-dot column samples. Thus, these columnar QD structures may be important under high injection conditions, such as lasing.

6.1.1 QUANTUM DOT LASER

Semiconductor lasers are key components in a number of widely used technological products, including compact disk players and laser printers, and they will play critical roles in optical communication schemes. The basis of laser operation depends on the creation of non-equilibrium populations of electrons and holes, and coupling of electrons and holes to an optical field, which will stimulate radiative emission. Calculations carried out in the early 1970s by C. Henry [132] predicted the advantages of using quantum wells as the active layer in such lasers: the carrier confinement and nature of the electronic density of states should result in more efficient devices operating at lower threshold currents than lasers with "bulk" active layers. In addition, the use of a quantum well, with discrete transition energy levels dependent on the quantum well dimensions (thickness), provides a means of "tuning" the resulting wavelength of the material. The critical feature size-in this case, the thickness of the quantum well-depends on the desired spacing between energy levels. For energy levels of greater than a few tens of millielectron volts (meV, to be compared with room temperature thermal energy of 25 meV), the critical dimension is approximately a hundred angstroms. Although the first quantum well laser, demonstrated in 1975, was many times less efficient than a conventional laser [133], the situation was reversed by 1981 through the use of new materials growth capabilities (molecular beam epitaxy), and optimization of the heterostructure laser design [134].

Even greater benefits have been predicted for lasers with quantum dot active layers. Arakawa and Sakaki [135] predicted in the early 1980s that quantum dot lasers should exhibit performance that is less temperature-dependent than existing semiconductor lasers, and that will in particular not degrade at elevated temperatures. Other benefits of quantum dot active layers include further reduction in threshold currents and an increase in differential gain-that is, more efficient laser operation [136]. Figures 6.1 and 6.2 illustrate some of the key concepts in the laser operation. Stimulated recombination of

electron-hole pairs takes place in the GaAs quantum well region, where the confinement of carriers and of the optical mode enhances the interaction between carriers and radiation (Fig. 6.1). In particular, note the change in the electronic density of states, as a function of the "dimensionality" of the active layer, shown in Figure 6.2. The population inversion (creation of electrons and holes) necessary for lasing occurs more efficiently as the active layer material is scaled down from bulk (3-dimensional) to quantum dots (0-dimensional). However, the advantages in operation depend not only on the absolute size of the nanostructures in the active region, but also on the uniformity of size. A broad distribution of sizes "smears" the density of states, producing behavior similar to that of bulk material.

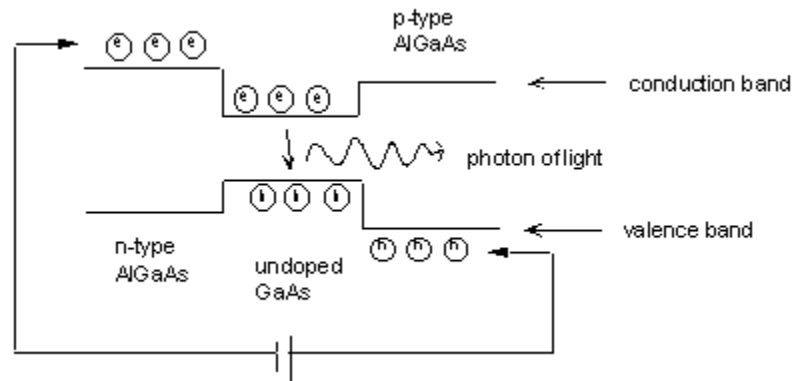


Figure 6.1: Schematic of a semiconductor laser.

Thus, the challenge in realizing quantum dot lasers with operation superior to that shown by quantum well lasers is that of forming high quality, uniform quantum dots in the active layer. Initially, the most widely followed approach to forming quantum dots was through electron beam lithography of suitably small featured patterns ($\sim 300 \text{ \AA}$) and subsequent dry-etch transfer of dots into the substrate material. The problem that plagued these quantum dot arrays was their exceedingly low optical efficiency: high surface-to-volume ratios of these nanostructures and associated high surface recombination rates,

together with damage introduced during the fabrication itself, precluded the successful formation of a quantum dot laser.

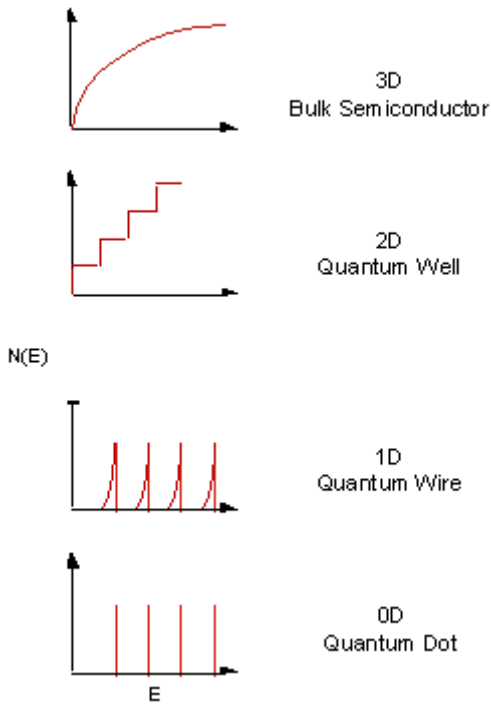


Figure 6.2: Density of electronic states as a function of structure size.

With the demonstration of the high optical efficiency from self-assembled formation of quantum dots discussed in previous chapters, and which form without need of external processing and having the natural overgrowth of cladding material (which addressed issues of surface recombination), there ensued a marked increase in quantum dot laser research. The first demonstration of a quantum dot laser with high threshold density was reported by Ledentsov and colleagues in 1994 [137]. Bimberg et al. [138] achieved improved operation by increasing the density of the quantum dot structures, stacking successive, strain-aligned rows of quantum dots and therefore achieving vertical as well as lateral coupling of the quantum dots. In addition to utilizing their quantum size effects

in edge-emitting lasers, self-assembled quantum dots have also been incorporated within vertical cavity surface-emitting lasers [142].

As with the demonstration of the advantages of the quantum well laser that preceded it, the full promise of the quantum dot laser must await advances in the understanding of the materials growth and optimization of the laser structure. Although the self-assembled dots have provided an enormous stimulus to work in this field, there remain a number of critical issues involving their growth and formation: greater uniformity of size, controllable achievement of higher quantum dot density, and closer dot-to-dot interaction range will further improve laser performance. Better understanding of carrier confinement dynamics and capture times, and better evaluation of loss mechanisms, will further improve device characteristics.

Since their first realization in 1994 quantum dot lasers have shown tremendous performance improvements and technological progress establishing these devices as powerful coherent sources in the mid infrared spectral region. The possibility to design a wide range of emission wavelengths in one material system renders quantum dot lasers particularly suitable for applications in the mid infrared region, the spectral region where gases and vapors have their characteristic absorption features associated with molecular vibrations. Trace gas analysis of chemicals such as CO, CH₄, NH₃, N₂O, SO₂ and HNO₃ as well as many organic compounds is only one application which is important in pollution detection, industrial process monitoring, chemical forensics, chemical and biological warfare and non-invasive medical diagnostics. Other applications based on the transmission windows of the atmosphere include collision avoidance radars in automobiles and ultra-fast optical wireless communication.

6.1.2 QUANTUM DOT INFRARED PHOTODETECTOR

Quantum dot infrared detector (QDIP) is another example of optoelectronic devices benefiting from nano-scale semiconductor structures. In QDIPs, carriers are usually photoexcited out of the dots into the host material and they are collected by biased front

and back contact layers, like in quantum well infrared detectors (QWIP). The most important benefit of quantum dot structures is their high absorption for normal incident light compared to transparency for QWIPs. In addition, QDIPs have an enlarged spectral range of operation, compared to QW structures.

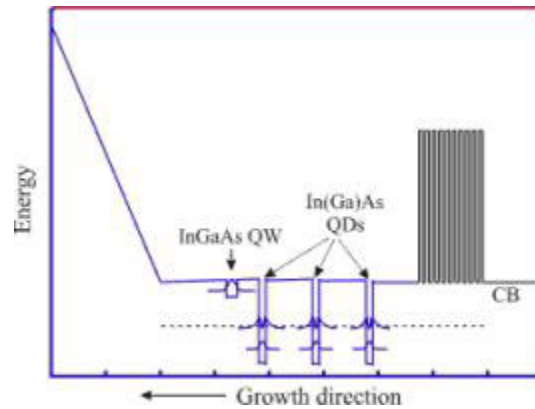


Figure 6.3: Quantum dot infrared photodetector schematics.

Furthermore, a novel type of QDIP (Figure 6.3) was recently demonstrated a new functionality relying on the 3-D localization of carriers within quantum dots. The lateral conductivity changes strongly if carriers are excited into conducting states within the host material, the wetting layer of self-assembled dot layers or especially within high mobility quantum well layers. The latter operation principle is the most advanced. Excited electrons are spatially transferred into a quantum well and keep bound there for a long time. This prolonged lifetime of electrons in the conducting QW enhances the internal gain and the photoresponse of the detector structure drastically. A photoresponse in excess of 11 A/W was observed at lateral interdigital finger contacts on a GaAs/InAs quantum dot detector structure with an InGaAs QW channel.

A similar functionality is reached in Si/Ge quantum dot structures in which hole states are localized within Ge dots at low temperature. Normal incident mid-infrared light excites the holes and the lateral photoconductivity increases. The incorporation of SiGe quantum wells with high hole mobility enhances the photoresponse by nearly two orders of

magnitude. The dark current changes just slightly and is remarkably low at low temperature $T=20\text{K}$, indicating efficient trapping of carriers by the dots.

6.2 Electronic Quantum Dot Based Devices

While optoelectronic devices utilizing semiconductor quantum dots were demonstrated to produce superior results to their conventional analogs and may not be too far from wide industrial use, quantum dot applications for electronic circuitry still belong more to the scientific research realm. Yet as the critical dimensions in the mainstream semiconductor industry continue to shrink according to Moore's law, it is inevitable that quantum dot based transistors and more complex logic elements will grow tremendously when CMOS gate size approaches quantum mechanical limits.

To this end we would like to first discuss single electron transistor (SET) as a basic element of quantum dot based electronics and then to proceed with an outline of quantum dot cellular automata (QCA) to show that new paradigm can be utilized for quantum dot based logic devices.

6.2.1 SINGLE ELECTRON TRANSISTOR

The typical schematic of a single electron transistor is shown of Figure 6.4.

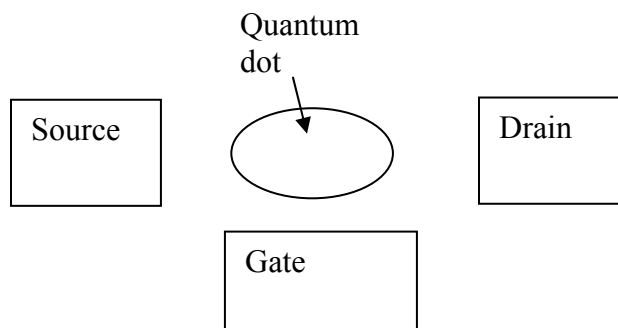


Figure 6.4: Schematic of a single electron transistor

Carriers can tunnel in and out of the quantum dot while transport characteristics are governed by wave-functions of the electrons in this 3-D confined structure and can be modulated by the applied gate voltage. To allow controllable operation of the SET, the quantum dot charging energy $E_c = q^2/2C$ should be larger than thermal agitation energy $k_B T$, where C is the quantum dot capacitance. Therefore, requirements for reliable room temperature operation of single electron devices impose severe limitations on the quantum dot dimensions.

In the SET shown on Figure 6.4, the quantum dot is coupled via two tunnel junctions to a transport voltage source $V = V_S - V_D$ so that a current can flow. The dot is, furthermore, coupled capacitively to a gate voltage V_G . The charging energy of the system depends on the number of electrons n on the dot and the voltages. For the transistor $C = C_S + C_D + C_G$ is the total capacitance of the island, i.e. the sum of the two junction capacitances and the gate capacitance, and all three voltage sources define the gate charge $Q_G = C_G V_G + C_S V_S + C_D V_D$. In a tunneling process, increasing the dot charge from n to $n + 1$, the charging energy changes by

$$E_c(n+1, Q_G) - E_c(n, Q_G) = \left(n + \frac{1}{2} - \frac{Q_G}{e} \right) \frac{e^2}{C} \quad (6.1)$$

These energy differences are equally spaced and can be tuned by the gate voltage. For definiteness, we assume that the energy of the electrons in the source is higher than that in the drain. Then, at low temperature, tunneling from the source to the dot (transition from n to $n+1$) is possible if the energy in the source eV_S is high enough to compensate for the increase in charging energy of the island

$$eV_S > E_c(n+1, Q_G) - E_c(n, Q_G) \quad (6.2)$$

Similarly, tunneling from the dot (transition from $n+1$ to n) to the drain is possible at low temperature only if

$$E_c(n+1, Q_G) - E_c(n, Q_G) > eV_D \quad (6.3)$$

Both conditions have to be satisfied simultaneously in order for a current to flow through the SET. At low transport voltages, depending on the gate voltage, V_G , the transistor may be either in a Coulomb blockade regime or have a finite current. By varying the gate voltage, one can observe Coulomb oscillations, i.e. the periodic dependence of the conductance on Q_G .

Other devices [139] using controlled transfer of single electrons can be constructed based on the SET concept and can e.g. be utilized as current standards. In the next section, we will extend the discussion to applications employing multiple quantum dots to produce logic circuit elements.

6.2.2 CELLULAR AUTOMATA

Quantum-dot Cellular Automata (QCA) is an approach to computing with quantum dots, which is based on encoding binary information in the charge configuration of quantum-dot cells [143]. The interaction between cells is Coulombic, and provides the necessary computing power. No current flows between cells and no power or information is delivered to individual internal cells. Local interconnections between cells are provided by the physics of cell-cell interaction.

A QCA cell (Figure 6.5) consists of 4 quantum dots positioned at the vertices of a square and contains 2 extra electrons. The configuration of these electrons is used to encode binary information. The 2 electrons sitting on diagonal sites of the square from left to right and right to left are used to represent the binary "1" and "0" states respectively. For an isolated cell these 2 states will have the same energy. However for an array of cells, the state of each cell is determined by its interaction with neighboring cells through the Coulomb interaction.

The cell contains two mobile electrons, which are allowed to tunnel between neighboring sites of the cell. The compensating positive charge is fixed and immobile. Tunneling out of the cell is assumed to be completely suppressed by the potential barriers between cells. It is also possible to add a fifth dot at the center of the square; the addition of this dot

improves the behavior of the cell slightly but for simplicity we will focus mainly on the four-dot cell.

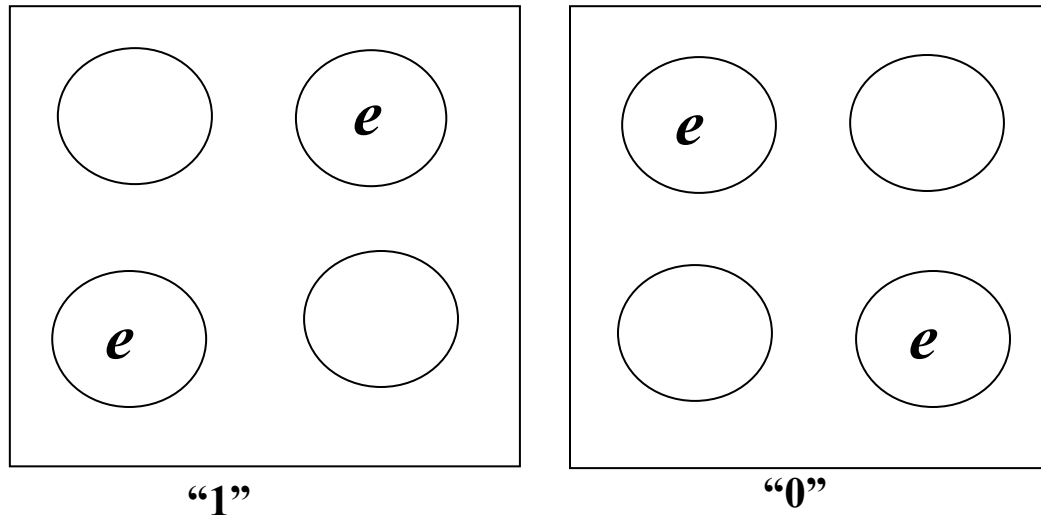


Figure 6.5: Four quantum dot elemental cell in “0” and “1” states.

If the barriers between cells are sufficiently high, the electrons will be well localized on individual dots. The Coulomb repulsion between the electrons will tend to make them occupy antipodal sites in the square as shown in Fig. 6.5. For an isolated cell there are two energetically equivalent arrangements of the extra electrons which we denote as a cell polarization $P = +1$ and $P = -1$. The term "cell polarization" refers only to this arrangement of charge and does not imply a dipole moment for the cell. The cell polarization is used to encode binary information - $P = +1$ represents a binary 1 and $P = -1$ represents a binary 0.

The two polarization states of the cell will not be energetically equivalent if other cells are nearby. Consider two cells close to one another as shown in the inset of Fig. 6.6. The figure inset illustrates the case when cell 2 has a polarization of $+1$. It is clear that in that case the ground-state configuration of cell 1 is also a $+1$ polarization. Similarly if cell 2 is in the $P = -1$ state, the ground state of cell 1 will match it.

Arrays of QCA cells configured correctly can perform complex computational tasks[144]. A linear array of cells can be used to form a binary wire. An inverter may be designed by positioning the cells diagonally. Considering the influence of several

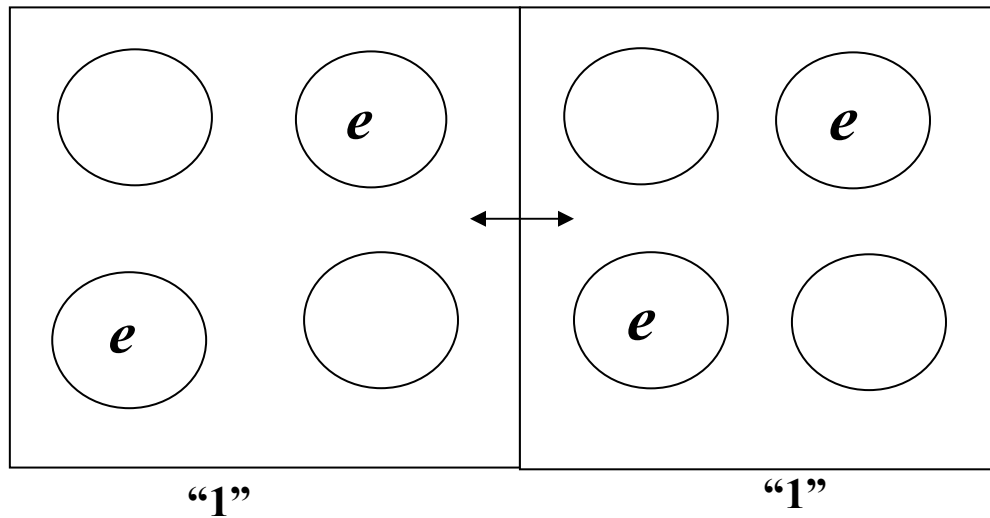


Figure 6.6: Interaction between two nearby QCA cells.

neighboring cells on a "central" cell state leads to the idea of majority voting logic. This behavior can be used to implement a majority gate and a programmable AND/OR gate. Inverters, majority gates and programmable logical gates provide the basis for computing in this scheme. It is possible to cross two QCA binary wires in the plane, with no interference. Building up more complicated operations from the basic gates, a full adder may be implemented using QCA cells. The interactions between cells are sufficiently local that hierarchical design is possible.

Examples of QCA binary wire (a) and of an inverter (b) are shown on the Figure 6.7. The left-most cell is fixed with a polarization representing the input. The ground state configuration of the remaining free cells is then one with each cell polarized in the same way as the input cell. We can consider this "transmission" of the input signal from one end to the other. Cells which are positioned diagonally from each other tend to anti-align.

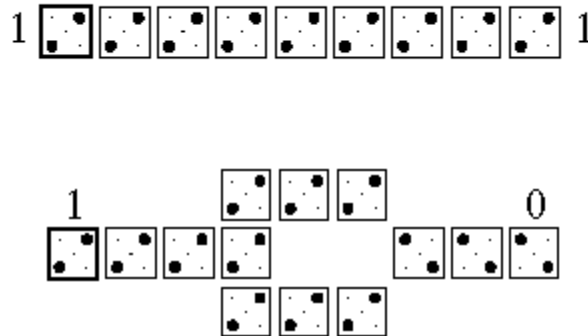


Figure 6.7: Simple logical elements implemented with QCA cells: (a) binary wire and (b) inverter [144].

This feature is employed to construct an inverter as shown on Fig 6.7(b). The anti-alignment can also be seen by examination to be a simple consequence of the mutual repulsion between electrons and the geometry of the cells. Although two diagonal cells function as an inverter, this more symmetric design ensures exact symmetry between the inversion of a 1 and a 0. More complex logical elements can also be implemented in a similar fashion.

Setting an input requires coercively establishing the state of the first cell in the wire. This can be accomplished very simply by charging nearby conductors to repel electrons from one dot and attract them to another. Reading an output state is more difficult. It requires the ability to sense the charge state of a dot without having the measurement process alter the charge state. Since the local charge produces a local electrostatic potential, this is really a question of constructing a small electrometer. Electrometers made from ballistic point-contacts and from quantum dots themselves have already been demonstrated. These electrometers can non-invasively measure the charge state of a single dot. Input and output are only performed at the edges of the array; no information or energy needs to flow to interior cells.

6.3 Conclusions

In this chapter existing and potential optoelectronic and electronic device applications of semiconductor quantum dots, and, in particular, strain induced self-assembled nano-scale islands are discussed. QD lasers have active regions in which the gain material is confined in all three spatial dimensions. Semiconductor quantum dot lasers manifest properties superior to those of conventional diode-laser heterostructures and quantum-well structures. The appeal of QD lasers is that they have characteristics approaching the atomic ideal, meaning that they can offer a lower threshold current for lasing, enhanced spectral purity, and a greater independence from the effects of temperature.

An important benefit of infrared photodetectors based on quantum dot structures is spatial separation of the localized ground state and continuum conducting states of the electron increasing significantly the photoelectron capture time and photoconductive gain. Large values of gain result in high responsivity, which in turn improves detectivity and raises the device operating temperature.

Single electron transistors are considered to be candidates as elements for future low power, high density integrated circuits because of their potential for ultra-low power operation involving only a few electrons. In order to be useful in practical applications, however, SETs must be operable at room temperature. Capacitance and thermal fluctuation limitations require that the quantum dot size of the SET be on the order of 10 nm or less, a feature size so far unreachable with conventional microfabrication techniques, but quite realistic through strain induced island self assembly.

Finally, a quantum-dot cellular automata paradigm was described relying on physically mediated cell-cell interaction providing coupling between the states of nearby cells. Inputs to array are set by physically coercing edge cells to particular states. Outputs are read by non-invasively sensing the state of edge cells. Computing is accomplished by the mapping between the physical ground state of the array and the logical solution state of the computational problem.

Chapter 7: Conclusions

This dissertation has been devoted to the study of InAs quantum dots formed by a strain-induced islanding process on different substrate materials with emphasis on the potential device applications of such structures. In the Chapter 2 fabrication and characterization techniques along with fundamentals of crystal growth and strain-induced islanding were discussed. Special attention was paid to molecular beam epitaxy, allowing crystal growth with atomically abrupt interfaces necessary for creating uniform and controllable confining potentials. Description of crystal formation with focus on strain induced self-assembly of nanoscale islands at an interface of two lattice mismatched semiconductor materials compared kinetics and thermodynamics of homogeneous epitaxial growth and introduced the main parameters influencing the process. This was followed up with a description of strained heterogeneous epitaxial growth leading to the formation of nanoscale islands, which occurs when material of close but slightly different lattice constant is deposited on a host substrate. Finally, overview of the characterization methods used throughout this dissertation was provided encompassing high resolution direct observation techniques of atomic force microscopy and transmission electron microscopy as well as more application oriented optical spectroscopy and electrical measurements.

Structural and optical properties of these strain induced semiconductor quantum dots were discussed in Chapter 3, which begins defining the narrow growth window in which islands can be fabricated in a defect free, controllable form that is necessary for quantum dot applications. Coherent, dislocation free dots can be grown only within a deposition window of two monolayers or approximately 6 Å of deposited material, and the exact transition point is a function of the growth temperature. The second section of this

chapter studies the effects of growth parameters on dot density, which is important for both optoelectronic device applications (high density) and electronic device applications (intermediate density). Although both growth rate and monolayer cover effect the dot density, the most significant effect on dot density is the V/III flux ratio. After key factors influencing islanding were identified we proceeded to a theoretical description of quantum confinement which establishes the connection between the physical structure of the dots and their optically active electronic states. Photoluminescence is used to observe the effects of changing crystal growth parameters on these states. Clear correlation of luminescence spectra with the change in physical structure of the InAs dot regions is detected.

A vertically aligned quantum dot columnar structures have been investigated in Chapter 4. The vertical alignment originates from the surface stress field which drives In and Ga adatoms in different directions. The dot columns were shown to be defect free from cross-section transmission electron microscopy measurements. A simplistic model of the behavior of island ensembles with subsequent layer stacking using elasticity theory formalism was introduced. The qualitative results of the simulation were insightful and predicted that self-organization occurs with island layer stacking, and that island density in the top stacked layers is independent of the initial layer distribution, while considerably influenced by the spacer layer thickness. Autocorrelation function was shown to be a useful instrument to detect and characterize island ordering. The structural ordering of the quantum dot columns was experimentally observed and characterized. Single, 5, 10, and 20 dot layers were investigated, each with 50Å of GaAs spacer layers. Atomic-force microscopy was used to investigate the size distribution dependency on the number of quantum dot layers deposited. We observed an increase in the average height and in-plane diameter of the dots, resulting in slightly more hemispherical dots after 20 dot layers were deposited. A decrease in the size variation of the dots with increasing number of quantum dot layers was also detected, as well as ordering of dots in (100) directions, which are soft crystallographic directions for GaAs. Results were in good qualitative agreement with simulation predictions. The dot volume density and size

uniformity increase with vertical stacking of the dot layers is particularly important in quantum dot structures designed for optoelectronic applications.

Chapter 5 is dedicated to investigation of the new material system InAs strain induced islands on Ge, which is interesting both from the standpoint of InAs quantum dot integration into mainstream group IV oriented semiconductor industry and due to unique scientific opportunity to study role of surface diffusion in the islanding process. A set of InAs on Ge samples were grown with molecular beam epitaxy along with a control set of InAs islands on GaAs under identical conditions. Since lattice mismatch between InAs and Ge is nearly identical to that between InAs and GaAs, observed differences in islanding statistics are attributed to the surface diffusion contribution into processes governing island self-assembly which normally is considered secondary to strain induced effects. Observed islanding dynamics and phase evolution were in agreement with developed rate equation theory and adatom binding energy values reported by other researchers.

Finally, in Chapter 6, existing and potential optoelectronic and electronic device applications of semiconductor quantum dots, and, in particular, strain induced self-assembled nano-scale islands were discussed. Semiconductor quantum dot lasers manifest properties superior to those of conventional diode-laser heterostructures and quantum-well structures. The appeal of QD lasers is that they have characteristics approaching the atomic ideal, meaning that they can offer a lower threshold current for lasing, enhanced spectral purity, and a greater independence from the effects of temperature. Infrared photodetectors with increased photoelectron capture time and photoconductive gain can be fabricated with semiconductor quantum dot structures. Semiconductor quantum dot based single electron transistors are considered to be candidates as elements for future low power, high density integrated circuits because of their potential for ultra-low power operation involving only a few electrons. Quantum dots fabricated with strain induced self-assembly techniques approach capacitance and thermal fluctuation limitations required for SET operation at room temperature. Quantum-dot cellular automata paradigm relying on physically mediated cell-cell

interaction providing coupling between the states of nearby cells can be introduced to replace the currently utilized FET-based paradigm facing fundamental challenges with gate size below $0.1\mu\text{m}$. Quantum computing is accomplished by the mapping between the physical ground state of the cell array and the logical solution state of the computational problem.

Bibliography

- [1] J. A. Venables et al. Growth and Properties of Ultrathin Epitaxial Layers, edited by D.A. King and D.P. Woodruff, New York: Elsevier, 1997.
- [2] Zhenyu Zhang, Max G. Lagally. Morphological Organization in Epitaxial Growth and Removal, River Edge, NJ: World Scientific, 1998.
- [3] J.S. Foord, G.J. Davies, and W.T. Tsang. Chemical Beam Epitaxy and Related Techniques, New York: Wiley, 1997.
- [4] Kenichi Iga, Susumu Kinoshita. Process Technology for Semiconductor Lasers : Crystal Growth and Microprocesses, New York: Springer, 1996.
- [5] Karl Eberl, Pierre M. Petroff, and Piet Demeester. Low Dimensional Structures Prepared by Epitaxial Growth or Regrowth on Patterned Substrates, Boston: Kluwer Academic Publishers, 1995.
- [6] J. R. Barnes, A. C. F. Hoole, M. P. Murrell, M. E. Welland and A. N. Broers, Appl. Phys. Lett. 67:1538, 1995.
- [7] W. Lu, A. J. Rimerberg, K. D. Maranowski and A. C. Gossard. Appl. Phys. Lett., 77:2746, 2000.
- [8] D.G. Austing, H. Tamura, Y. Tokura, K. Muraki, S. Amaha, K. Ono, S. Tarucha. Physica E 10:112 , 2001.

- [9] E. S. Snow and P. M. Campbell. Science 270:1639, 1995.
- [10] K. Matsumoto. Physica-B 227:92, 1996.
- [11] K. Matsumoto, M. Ishii, K. Segawa, Y. Oka, B. J. Vartanian and J. S. Harris. Applied Physics Letters 68:34, 1996.
- [12] J. Shirakashi, K. Matsumoto, N. Miura, and M. Konagai. Jap. J. Appl. Phys., Part 2 (Letters) 36:1257, 1997.
- [13] C. Wang, M. Shim and P. Guyot-Sionnest, Science 291:2390, 2001.
- [14] D.R. Stewart, D. Sprinzak, C.M. Marcus, C.I. Duruöz, and J.S. Harris, Jr. Science 278:1784, 1997.
- [15] S.R. Patel, D.R. Stewart, C.M. Marcus, M. Gokcedag, Y. Alhassid, A.D. Stone, C.I. Duruöz, and J.S. Harris, Jr. Physical Review Letters 81:5900, 1998.
- [16] I. N. Stranski and L. Krastanow. Sitz. Ber. Akad. Wiss., Math.-naturwiss. Kl. Abt. IIb 146:797, 1938.
- [17] M. Volmer and A. Weber. Z. Physik. Chem. 119:277, 1926.
- [18] M.A. Herman, H. Sitter. Molecular beam epitaxy: fundamentals and current status, New York: Springer, 1996.
- [19] E. H. Kennard. Kinetic Theory of Gases. McGraw Hill, 1938.
- [20] G. A. Somorjai and J. E. Lester. Progr. Solid State Chem., 4:1, 1967.
- [21] L. Dunoyer. C. R. Acad. Sci. Paris, 152:549, 1911.
- [22] O. Stern. Z. Phys., 2:49, 1920.

- [23] N. F. Ramey. Molecular Beams. Oxford Univ. Press (Clarendon), London and New York, 1963.
- [24] R. E. Stickney. Advan. At. Mol. Phys., 3:143, 1967.
- [25] G. P. Thomson and A. Reid. Nature, 119:80, 1927.
- [26] L. Bruck. Ann. Phys. Leipzig, 26:233, 1936.
- [27] G. I. Finch and A. G. Quarrell. Proc. Roy. Soc. A, 141:398, 1933.
- [28] G. I. Finch and A. G. Quarrell. Proc. Phy. Soc., 46:148, 1934.
- [29] J. H. van de Merwe. Discuss. Faraday Soc., 5:201, 1949.
- [30] A. J. Elleman and H. Wilman. Proc. Phys. Soc., 61:163, 1948.
- [31] R. J. Miller and C. H. Bachman. J. Appl. Phys., 29:1277, 1958.
- [32] R. B. Schoolar and J. N. Zemel. J. Appl. Phys., 35:1848, 1964.
- [33] K. G. Gunter. Z. Naturforsch., 13a:1081, 1958.
- [34] R. Zuleeg and E. J. Senkovits. Extended Abstracts, 123rd Meeting of the Electrochem. Society, Pittsburgh, Pennsylvania, 95:2224, 1963.
- [35] J. E. Davey and T. Pankey. J. Appl. Phys., 35:2203, 1964.
- [36] J. E. Davey and T. Pankey. J. Appl. Phys., 39:1941, 1968.
- [37] B. A. Joyce and R. R. Bradley. Phil. Mag., 14:289, 1966.
- [38] J. R. Arthur. J. Appl. Phys., 39:4032, 1968.
- [39] J. R. Arthur. Proc. Int. Mater. Symp. Struct. Chem. Solid Surfaces, Berkeley.

- [40] L. Esaki and R. Tsu. IBM J. Res. Develop., 14:61, 1970.
- [41] J. R. Arthur and J. J. Lepore. J. Vac. Sci. Technol., 8:494, 1969.
- [42] A. Y. Cho. J. Vac. Sci. Technol., 8:531, 1971.
- [43] A. Y. Cho. J.J. Appl. Phys., 41:782, 1970.
- [44] L. Esaki, L. L. Chang, W. E. Howard, and V. L. Rideout. Proc.11th Int. Conf. Phys. Semicond., Warsaw, 56-58:431, 1972.
- [45] L. L. Chang, L. Esaki, W. E. Howard, and R. Ludeke. J. Vac. Sci. Technol., 10:11, 1973.
- [46] L. Esaki and L. L. Chang. Phys. Rev. Lett., 33:495, 1974.
- [47] R. Dingle, W. Wiegmann, and C. H. Henry. Phys. Rev. Lett., 33:827, 1974.
- [48] L. L. Chang, L. Esaki, W. E. Howard, R. Ludeke, and G. Schul. J. Vac. Sci. and Technol., 10:655, 1973.
- [49] P. M. Petroff, C. Weisbuch, R. Dingle, A. C. Gossard, and W. Wiegmann. Appl. Phys. Lett., 55:1888, 1981.
- [50] E. C. Larkins and Jr. J. S. Harris. Molecular Beam Epitaxy - Applications to Key Materials, page 114. Noyes Publications, Park Ridge, N. J., 1995. edited by Robin F. C. Farrow.
- [51] A. Y. Cho and J. R. Arthur. Prog. Solid State Chem., 10:157, 1975.
- [52] J. C. M. Hwang, J. V. DiLorenzo, P. E. Luscher, and W. Knodie. Appl. Phys. Lett., 42:66, 1983.

- [53] J. P. A. van der Wagt. Reflection High-Energy Electron Diffraction During Molecular-Beam Epitaxy. PhD thesis, Stanford University, 1994.
- [54] J. M. van Hove, C. S. Lent, P.R. Pukite, and P. I. Cohen. J. Vac. Sci. Technol., B1:741, 1983.
- [55] A. Y. Cho. Thin Solid Films, 100:291, 1983.
- [56] C. E. C. Wood, T. M. Kerr, T. D. McClean, D. I. Westwood, J. D. Medland, S. Blight, and R. Davies. J. Appl. Phys., 60:1300, 1986.
- [57] J. H. Neave, B. A. Joyce, P. J. Dobson, and N. Norton. Appl. Phys., A31:1, 1983.
- [58] K. R. Evans, C. E. Stutz, E. N. Taylor, and J. E. Ehret. Appl. Surf. Sci., 56-58(1-4). Pt. B.
- [59] C. H. Hale, I. T. Muirhead, S. P. Fisher, and J. S. Orr. J. Vac. Sci. Technol., A8:285, 1990.
- [60] E. S. Hellman and Jr. J. S. Harris. J. Cryst. Growth, 81:38, 1987.
- [61] K. L Bacher. Improvements Toward High-Efficiency Vertical-Cavity Surface-Emitting Lasers. PhD thesis, Stanford University, 1995.
- [62] Robin F. C. Farrow, editor. Molecular Beam Epitaxy. Noyes Publications, Park Ridge, NJ, 1995.
- [63] Marian A. Herman. Molecular beam epitaxy. Springer Verlag, 1989.
- [64] K. Ploog. Molecular beam epitaxy of III-V compounds. Springer Verlag, 1984.
- [65] J. Tsao. Materials Fundamentals of Molecular Beam Epitaxy. Boston Academic Press, Boston, MA, 1993.

- [66] C. D. Thurmond. J. Phys. Chem. Solids, 26:785, 1965.
- [67] J. R. Arthur. J. Phys. Chem. Solids, 28:2257, 1967.
- [68] Richard E. Honig and Dean A. Kramey RCA Review, page 285, June 1969.
- [69] L. Daweritz and R. Hey. Surface Science, 236:15, 1990.
- [70] C. Herring. Physics of Powder Metallurgy. McGraw-Hill, New York, 1951.
- [71] L. D. Landau. Collected Papers, page 540. Pergamon Press, Oxford, 1965.
- [72] C. Herring. Phys. Rev., 82:87, 1951.
- [73] W. A. Tiller. The Science of Crystallization: Microscopic Interfacial Phenomena. Cambridge University Press, Cambridge, England, 1991.
- [74] J.W. Matthews and A.E. Blakeslee. J. Cryst. Growth, 27:118, 1974.
- [75] O. Brandfand et. al. J. Cryst. Growth, 127:513, 1993.
- [76] W. W. Mullins. J. Appl. Phys., 28:333, 1957.
- [77] R. J. Asaro and W. A. Tiller. Metallurgical Transactions, 3:1789, 1972.
- [78] D. J. Srolovitz. Adv. Metall., 37:621, 1989.
- [79] Cheng-Hsin Chiu and Huajian Gao. Mat. Res. Soc. Symp. Proc., 356:33, 1995.
- [80] A.L Weisenhorn, P.K. Hansma, T.R. Albrecht, and C.F. Quate. Appl. Phys. Lett. 54:2651, 1989.
- [81] F. Thon. Electron Microscopy in Materials Science, Academic Press: New York, p.570, 1971.

- [82] G. Binnig, C.F. Quate, and Ch. Gerber. Phys. Rev. Lett. 56:930, 1986.
- [83] T.R. Albrecht, S. Akamine, T.E. Carver, and C.F. Quate. J. Vac. Sci. Technol. A 8:3386, 1990.
- [84] G. Binnig, H. Rohrer, F. Salvan, C. Gerber, A. Baro. Surface-Science, 157:373, 1985.
- [85] G. Meyer and N.M Amer. Appl. Phys. Lett. 53:1045, 1988.
- [86] S. Alexander, L. Hellemans, O. Marti, J. Schneir, V. Elings, P.K. Hansma, M. Longmiro, and J.J. Gurley. Appl. Phys. 65:164, 1989.
- [87] L. D. Landau and E. M. Lifshitz. Quantum Mechanics. Pergamon: Oxford, 2nd edition, 1987.
- [88] T. Inoshita, H. Sakaki. Physical Review B. Condensed-Matter , 56:4355, 1997.
- [89] C.-Y. Hung, J.S. Harris, Jr., A.F. Marshall, R.A. Kiehl. Applied Physics Letters, 73:330, 1998.
- [90] G. S. Solomon, J. A. Trezza, and J. S. Harris Jr. Appl. Phys. Lett., 66:991, 1995.
- [91] Y. Nabetani, T. Ishikawa, S. Noda, and A. Sasaki. J. Appl. Phys., 76:347, 1994.
- [92] B. J. Spencer, P. W. Voorhees, and S. H. Davis. Phys. Rev. Lett., 67:3696, 1991.
- [93] H. Van Houten and C. W. J. Benakker. Phys. Rev. Lett., 53:1893, 1989.
- [94] C. Weisbuch and B. Vinter. Quantum Semiconductor Structures. Academic Press, 1991.
- [95] K. J. Vahala. IEEE J. Quantum Electron., QE-24.-523, 1988.

- [96] Francesco Tassone. Based on discussions with F. Tassone.
- [97] L. Banyai and S. W. Koch. Semiconducting Quotum Dots. World Scientific Publishing Co., 1993.
- [98] Y. Miyamoto M. Asada and Y. Sematsur. IEEE J. Quantum Electron., QE-24:523, 1986.
- [99] G. W. Bryant. Phys. Rev., B37:8763, 1988.
- [100] T. Takagahara. Phys. Rev., B36:9293, 1987.
- [101] D. Vanderbilt and L. K. Wickham. Mat. Res. Symp. Proc., 202:555, 1991.
- [102] D.V. Brunev, I.G. Neizvestny, N.L. Shwartz, Z.Sh. Yanovitskaya. Computer-Physics-Communications, 147:255, 2002.
- [103] D. Leonard, M. Krishnamurthy, C. M. Reaves, S. P. Denbaars, and P. M. Petroff. Appl. Phys. Lett., 63:3203, 1993.
- [104] M. Tabuchi, S. Noda, and A. Sasaki. Science and technology of mesoscopic structures. Springer-Verlag:Tokyo, Japan, 1992.
- [105] Qianghua Xie, P. Chen, A. Kalburge, T. R. Ramachandran, A. Nayfonov, A. Konkar, and A. Madhukar. J. Cryst. Growth, 150:357, 1995.
- [106] G. S. Solomon, J. A. Trezza, A. F. Marshall, and J. S. Harris Jr. Phys. Rev. Lett., 76:952, 1996.
- [107] D. Leonard, S. Fafard, K. Pond, Y. H. Zhang, J. L. Merz, and P. M. Petroff. J. Vac. Sci. Tech. B, 12:2516, 1994.
- [108] G. S. Solomon, J. A. Trezza, and J. S. Harris Jr. Appl. Phys. Lett., 66:3161, 1995.

- [109] M. Sopanen and H. Lipsanen. Phys. Rev., B51:13868, 1995.
- [110] D. J. Eaglesham and M. Cerullo. Phys. Rev. Lett., 64:1943, 1990.
- [111] J. Y. Yao, T. G. Andersson, and G. L. Dunlop. J. Appl. Phys., 69:2224, 1991.
- [112] W. S. Lee, G. W. Yoffe, D. G. Schlom, and J. S. Harris Jr. J. Cryst. Growth, 111:131, 1991.
- [113] J. M. Gerard, J. B. Genin, J. Lefebvre, J. M. Moison, N. Lebouche, and F. Barthe. J. Cryst. Growth, 150:351, 1995.
- [114] J. Tersoff, C. Teichert, and M. G. Lagally. Phys. Rev. Lett., 76:1675, 1996.
- [115] N. Motta. Journal of Physics:Condensed Matter. 14:8353, 2002.
- [116] A.V. Kolobov, K. Morita, K.M. Itoh, E.E. Haller. Applied Physics Letters. 81:3855, 2002.
- [117] J. Drucker. IEEE Journal of Quantum Electronics. 38:975, 2002.
- [118] E. Lifshitz, A. Glozman, L.D. Litvin, H. Porteanu. Journal of Physical Chemistry B. 104:10449, 2000.
- [119] M. De-Seta, G. Capellini, F. Evangelisti, C. Spinella. Journal of Applied Physics. 92:614, 2002.
- [120] Zh. Yangting, M. Floyd, K.P. Driver, J. Drucker, P.A. Crozier, D.J. Smith. Applied Physics Letters. 80:3623, 2002.
- [121] A.J. Markworth. Metallography, 3:197, 1970.
- [122] F.M. Ross, J. Tersoff, R.M. Tromp. Microscopy and Microanalysis. 4: 254, 1998.

- [123] M. Meixner, E. Scholl, V.A. Shchukin, D. Bimberg. Physical Review Letters. 87:236101, 2001.
- [124] T.I. Kamins, G. Medeiros-Ribeiro, D.A.A. Ohlberg, R.S. Williams. Applied Physics A Materials Science Processing, A67: 727, 1998.
- [125] M. Qian. Metallurgical and Materials Transactions A Physical Metallurgy and Materials Science. 33A:1283, 2002.
- [126] M. Conti, B. Meerson, A. Peleg, P.V. Sasorov. Physical Review E Statistical,- Nonlinear, and Soft Matter Physics, 65:046117, 2002.
- [127] R.N. Stevens, C.K.L. Davies. Journal of Materials Science, 37:765, 2002.
- [128] P.Wynblatt and N.A.Gjostein. Progress in Solid State Chemistry, Pergamon: Oxford, 9:21, 1975.
- [129] B.K.Chakraverty. J.Phys. Chem. Solids 28:2401, 1967.
- [130] R.S. Williams, G. Medeiros-Ribeiro, T.I. Kamins, and D.A.A. Ohlberg. J. Phys. Chem. 102, 1998.
- [131] J.A. Venables. Philosophical Magazine, 27:697, 1973.
- [132] R. Dingle, W. Wiegmann, C.H. Henry. Physical Review Letters, 33:827, 1974.
- [133] J.P. van der Ziel, R. Dingle, R.C. Miller. W. Wiegmann, and W.A. Nordland, Jr. Appl. Phys. Lett. 26:463, 1975.
- [134] W.T. Tsang. Appl. Phys. Lett. 40:217, 1982.
- [135] Y. Arakawa, H. Sakaki. Appl. Phys. Lett. 40:939, 1980.

- [136] M. Asada, Y. Mayamoto, and Y. Suematsu. IEEE Journ. Quantum Electronics QE-22:1915, 1986.
- [137] Ledentsov, N.N., M. Grundmann, N. Kirstaedter, J. Christen, R. Heitz, J. Börher, F. Heinrichsdorff, D. Bimberg, S.S. Ruvimov, P. Werner, U. Richter, U. Gösele, J. Heydenreich, V.M. Ustinov, A.Yu. Egorov, M.V. Maximov, P.S. Kop'ev, and Zh.I. Alferov. Proc. ICPS-22, Vancouver 3:1855. Singapore: World Scientific, 1994.
- [138] D. Bimberg, N. Ledentsov, M. Grundmann, N. Kirstaedter, O. Schmidt, M. Mao, V. Ustinov, A. Egorov, P. Kop'ev, Zh. Alferov, S. Ruvimov, U. Gösele, and J. Heydenreich. Jap. Journal. Appl. Phys. 35:1311, 1996.
- [139] H. Ahmed. Microelectronic Engineering, 61-62:3, 2002.
- [140] D.H. Rich, T. Miller, T.-C. Chiang. Physical Review B Condensed-Matter. 41:3004, 1990.
- [141] H.T. Dobbs, D.D. Vvedensky, A. Zangwill. Applied Surface Science. 123-124:646, 1998.
- [142] D. Bimberg, N.N. Ledentsov, J.A. Lott. MRS-Bulletin. 27:531, 2002.
- [143] G. Toth, C.S. Lent. Physical Review A 63:052315, 2001.
- [144] A. Csurgay, W. Porod. International Journal of Circuit Theory and Applications, 29:3, 2001.

